Performance Analysis of Quantum-Enabled Radar Systems through Modelling and Experimentation

By

Jithin Kannanthara

A thesis submitted to the University of Birmingham
for the degree of DOCTOR OF PHILOSOPHY

Alkaline Group
School of Physics and Astronomy
College of Engineering and Physical Sciences
University of Birmingham

February 2023

ABSTRACT

This thesis presents the first realisation of a quantum-enabled radar in simulation. The thesis is focused on the fundamental limitations of conventional oscillator phase noise in the performance of radar systems and the development of a quantum-enabled radar (with ultra-low phase noise quantum oscillators) in the simulation. A radar model was developed and validated with the results from a commercially available L-band staring radar at the University of Birmingham to study the effects of oscillator phase noise and the performance capabilities of quantum-enabled radar systems. The whole radar model represents the behaviour of all the fundamental hardware building blocks with reasonable simplifications. The phase noise spectrum of the microwave generator unit locked to its cavity-stabilised internal laser, referred to as one manifestation of the quantum oscillator, is shown to have values at least 20 dB lower for every offset frequency in comparison to the L-band staring radar at the transmit frequency.

The conventional oscillator phase noise of the L-band staring radar is shown to manifest as clutter-induced phase noise floor in the range-Doppler plots, with the phase noise floor at least 25 dB above the thermal noise floor, limiting the SNR available for target detection. In range-Doppler plots, the thermal noise floor is the uniform noise floor present in all the range bins, whereas the phase noise floor is the extra noise floor present in range bins with higher clutter power. In comparison to the conventional radar phase noise floor, the quantum-enabled radar simulations show around 20 dB reduction in the phase noise floor in range bins with high levels of clutter in the simulation environment. The detection plots

show the successful detection of low RCS targets with quantum-enabled radar that fail to get detected in the classical radar for the same simulation environment. The quantum-enabled radar with ultra-low phase noise quantum oscillators makes it a promising system capable of detecting slow-moving very-low RCS targets even in extreme clutter.

DEDICATION

To my parents, Surathna and Pushpangathan,

and my wife, Brilya

ACKNOWLEDGMENTS

First of all, I would like to thank my primary supervisor, Yeshpal Singh, for providing me with the opportunity to pursue a PhD in the Alkaline group. I also thank him for his constant support and motivation throughout the duration of my PhD and for all the discussions, both at the professional and personal levels. I thank my secondary supervisor, Chris Baker, for all the guidance and immense help I have received. I also thank my tertiary supervisor, Mohammed Jahangir, for the help towards the PhD. I am also grateful to Kai Bongs and the UK National Quantum Technology Hub in Sensors and Timing.

I would also like to thank BAE systems and the EPSRC industrial-case award for providing me with the scholarship to pursue the PhD. I thank Henry White, Colin Bell, Phil Clark, and Bill Stafford from BAE systems for their constant help, supervision and discussions. I especially want to thank Colin Bell, without whom I would not have been able to complete my radar model and the PhD. Thank you for helping me through all the stages.

All the members of the Alkaline team, present and past, for all the memories and discussions over the past four years of the PhD. Special mention to the radar sub-group within the Alkaline team - with you guys, we achieved what we have achieved today. I would also like to thank members of the MISL group, our counterpart from the school of engineering.

To all my friends, the list is way too long. You all have been my support system all over the years. To all my lovable friends, living in different time zones, and pursuing their life, thank you so much for being with me throughout my ups and downs, for constantly

caring for each other, and for pushing each other to achieve greater goals.

My sincere thanks to my parents for my life and for making me who I am today. Thank you for providing me with a wonderful life amid all the hardships and for all the happiness. To my beloved wife, even though it's been only two years since we met, thank you for the unconditional love, care, support and trust. You are the best ones I could ever dream of. Thank you to everyone in both our families, for all the prayers and the love, especially her parents, and my sister.

There are a lot of people to thank, and many names might get missed. By reading this, please be assured that all of you are being thanked.

Contents

List of Figures

List of Tables

Chapter One

INTRODUCTION

This thesis presents the advanced modelling and performance capabilities of quantum-enabled radar systems. The first chapter of the thesis starts with a brief background of the work presented in the thesis. The chapter also includes a detailed literature survey that discusses the history of radars, radar applications and the current state of the art in radar systems, emphasising radar modelling and phase noise in radar systems. The literature survey leads to the motivation of the thesis. The chapter also includes a section on the original contributions of the PhD work and a section on publications during PhD work. The outline of the thesis is detailed in the final section of the chapter.

1.1 Background

The doctoral work presented in the thesis encompasses efforts towards the realisation of a quantum-enabled radar in simulations. A quantum-enabled radar consists of a quantum oscillator that replaces a conventional radar oscillator. The thesis includes the development of a whole radar model with the capability to encapsulate real radar scenarios in a simulation platform, validation of the simulated model by comparing the results from real radar field

trials, the experimental measurements for the phase noise and Allan deviation of the oscillators, culminating in an advanced model to assess the performance of a quantum-enabled radar. The thesis makes use of the advanced model to study the fundamental limitations of different components in radar, focusing on the limitations of oscillator phase noise in radar systems and the development of a quantum-enabled radar with ultra-low phase noise quantum oscillators in simulation.

Figure 1.1: Photo of the L-band staring radar at the University of Birmingham.

The whole radar model discussed in the thesis comprises all the fundamental hardware building blocks in the transmit chain, the receive chain, and the data processing chain. The radar model developed in the MATLAB/Simulink platform is built in a bottom-up approach and consists of modelling, simulation and validation of each building block to generate a complete radar model. The radar model currently presented in the thesis is based on an L-band multiple receive beam staring radar [1] at the University of Birmingham, pictured in figure 1.1, with reasonable simplifications. The simplifications include a single receive channel instead of an array of 64 receive channels and direct digital synthesis of the transmit signal

instead of frequency up-conversion from a reference signal. The radar model is validated by comparing the simulated results with the experimentally measured results from the L-band staring radar. Each radar building block is developed with the capability to optimise every parameter in the model to suit the user specifications and the power budget.

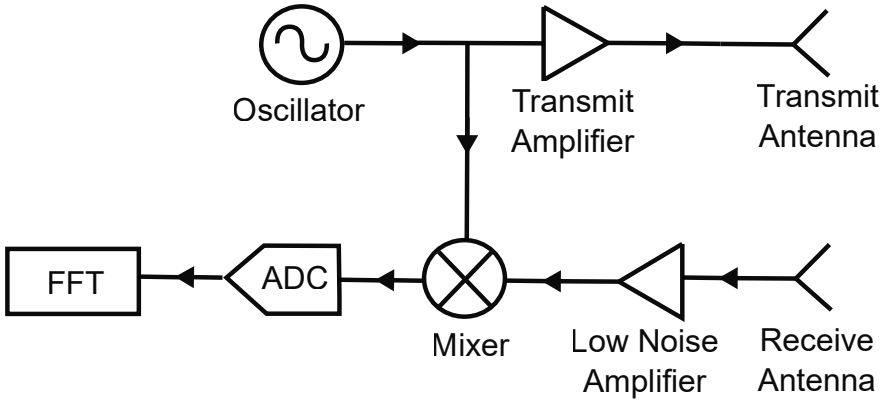

Figure 1.2: Generic block diagram of a basic radar system. The radar signal generated by the radar oscillator gets amplified before transmission to the environment. The received signal from the environment undergoes low noise amplification and frequency down-conversion, followed by analogue to digital conversion. The digitised signal corresponds to a two-dimensional (2D) matrix consisting of range and number of pulses. A 2D fast Fourier transform (FFT) operation is performed on the signal matrix to generate a range-Doppler plot.

A generic block diagram of a basic radar system with a radar oscillator and other building blocks are given in figure 1.2. The radar oscillator generates the radar signal, which gets amplified and finally broadcast to the environment by a transmit antenna. The signals reflected by the targets and clutter in the environment get detected by a receive antenna. The received signal undergo amplification and down-conversion, followed by digitisation using an analogue to digital converter (ADC). The signal at the output of the ADC corresponds to a 2D data matrix consisting of the range and the number of received pulses as the two dimensions of the data matrix. A 2D FFT is performed on the 2D matrix of the digitised received signals to generate a range-Doppler plot. The range-Doppler plot provides the range and Doppler frequency information of targets and clutter in the environment. A target Doppler spectrum provides the Doppler information of a radar target over time. Target

Doppler spectrum is generated from a consecutive array of range-Doppler plots for the range bin where the target is present.

In the thesis, real staring radar trials are replicated in the simulation platform, and the results from the staring radar trials and the simulations are compared to validate the radar model. The radar model is formulated from the actual measurements of the performance of the L-band staring radar. The results from the simulated radar model showed a high parity level with the results from experimental measurements carried out with the actual staring radar. The high fidelity of the radar model provided a powerful tool to test real and hypothetical radar scenarios and configurations in the simulation platform. The validated, high-fidelity radar model is used to explore the fundamental limitations of different building blocks in the radar system, emphasising the oscillator phase noise in radar target detection.

Phase noise is one of the fundamental limitations in the performance of radars. The phase noise in radar systems is primarily due to an imperfect oscillator with frequency fluctuations. The oscillator phase noise results in the phase noise floor coming out of the thermal noise floor in range-Doppler plots and Doppler spectrum, especially in high-clutter environments, masking slowly moving weak targets. The effect of phase noise can be seen in figure 1.3. Figure 1.3 represents the radar target spectrum from one of the drone trials performed at the University of Birmingham. The target spectrum consists of Doppler frequency on the vertical axis and time frames on the horizontal axis. Figure 1.3 shows that the drone can be detected and tracked at all times except between 95 s and 115 s, where the phase noise floor can be seen coming out of the thermal noise floor, resulting in an SNR reduction of at least 15 dB, affecting the target detection.

As part of the thesis work, measurements for the characterisation of the oscillators are performed, with phase noise and Allan deviation being the two figures of merit. The measurement campaign used extensive methods to characterise both classical radar and quantum

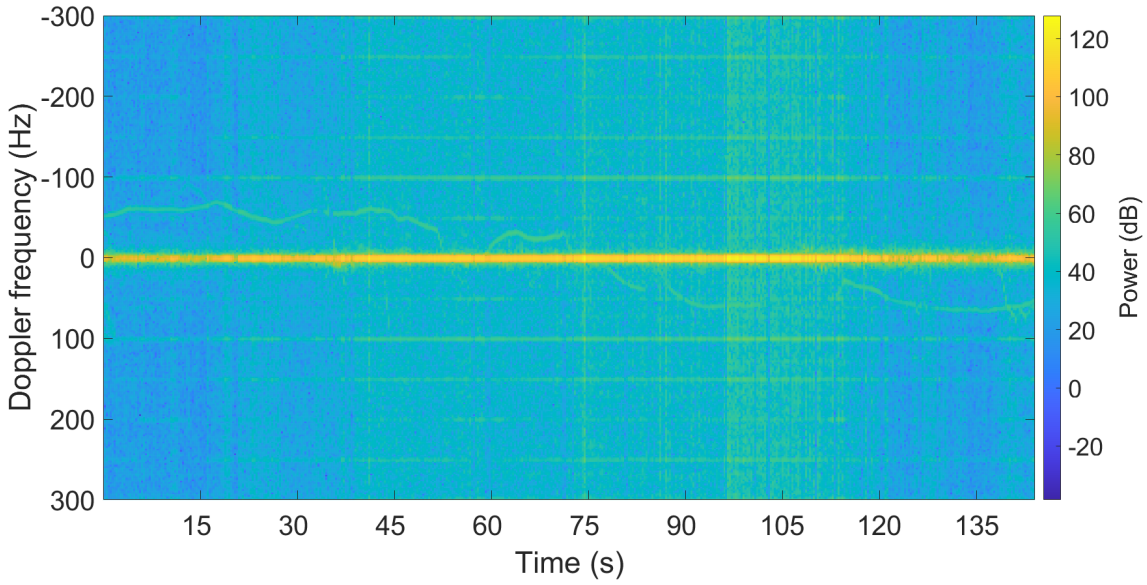

Figure 1.3: An example of a radar target spectrum from a drone trial. The drone can be easily seen in time frames with a lower phase noise floor. The phase noise floor is seen emerging out of the thermal noise floor, especially between 95 s and 115 s, resulting in a considerable reduction in the target SNR affecting detection.

oscillators. The phase noise measurement of classical radar oscillators is incorporated into the comprehensive radar model to generate simulations to study the limitation of oscillator phase noise in target detection. The phase noise measurements from the campaign are also used to generate simulations of quantum-enabled radar and to compare the simulated results from quantum-enabled radar and classical radar.

The thesis focuses on the limitations of oscillator phase noise in radar systems and the development of quantum-enabled radar in simulations. The comprehensive radar model, built from the actual measurements of the performance of the L-band staring radar, is used to explore the effects of oscillator phase noise and to develop an advanced model of the quantum-enabled radar. Experimental measurements of the phase noise of classical and quantum oscillators support the simulations. The reader will now be directed to the literature survey relevant to the research work presented in the thesis.

1.2 Literature Survey

The literature survey is divided into four subsections. The first subsection consists of the historical perspective of radars, followed by the radar applications in the second. The recent progress in radar modelling is discussed in the third subsection. The fourth subsection consists of literature on phase noise, and the effects of phase noise in radar systems are detailed.

1.2.1 Historical perspective

The history of radar goes back to as early as the 1880s when Heinrich Rudolf Hertz experimentally verified the theoretical work of James Clerk Maxwell. In the early 1870s, Maxwell formulated the general equations of the electromagnetic field [2]. Maxwell's work led to the inference that radio and light waves are electromagnetic waves and that, similar to light waves, radio waves can undergo reflection and refraction. Between 1886 and 1889, Hertz discovered electromagnetic waves [3] and verified the theoretical predictions by Maxwell.

Guglielmo Marconi achieved the first long-range transmission of electromagnetic waves in 1897 [4]. In 1900, Nichola Tesla observed the reflection of radio waves from large objects [5]. The first radar test happened in 1904 when Christian Hülsmeyer invented a transmitter-receiver system for traffic monitoring on the water in poor visibility [6]. In 1917, Nikola Tesla established the principles regarding the frequency and power level of primitive radars and predicted that a target's distance and speed could be measured [7]. The first practical radar system was built in 1935 by Sir Robert Watson-Watt [8]. Watson-Watt demonstrated the bouncing of radio waves from an aircraft and measured the target information from the travel time of the radio waves. In 1940, the United States Navy coined the term radar as an acronym for radio detection and ranging. In 1940, the scientific community also witnessed

the development of cavity magnetrons [9]. The introduction of cavity magnetrons as high-power microwave oscillators in 1940 saw a massive leap in the history of radars and radar oscillators. Over the decades, radars played a crucial role in the development of humankind, serving a wide range of applications.

1.2.2 Radar applications

Radar technology is currently used in many applications, including military, meteorology and weather, law enforcement, healthcare, mapping and astronomy. The military and defence radars are used in navigation and traffic management for both air [10], and sea [11], and in general defence [12, 13]. The radars are also used in the detection and surveillance of hostile targets [14], including drones [15, 16]. The weather radars [17, 18] are generally used to track and detect different weather phenomena, including rain [19], storm [20], snow and wind [21]. The law enforcement radars mainly include radar speed guns [22]. In healthcare, the radars are used for tumour tracking [23], speech monitoring [24], and vital signs monitoring [25]. In mapping and astronomy, radars are used for different applications, including planetary astronomy [26], and topographic mapping [27]. The more complex the radar system and the target environment become, the more difficult it is to test the radars physically. High-fidelity radar models are a possible solution to test complex radar systems in simulation platforms.

1.2.3 Progress in radar modelling

At present, the complexity associated with radar technology is increasing in a manner that testing an advanced radar system across all hardware combinations is impossible in the actual world. One solution to testing a radar across different hardware combinations is

developing radar models to accommodate and replicate the different configurations. Through radar modelling, a subset of real-world hardware and environmental conditions can be tested, and the results from the real tests can be used to validate extensive radar models.

Over the past few decades, there have been several attempts in the literature to model the different aspects of radars. Models to represent bi-static radar sea clutter and the performance of radar in coherent and non-coherent sea clutter were discussed in [28–31]. A computer model was developed to simulate the performance of three-dimensional laser radars using the C programming language and validated with real radar results [32]. An effective radar imaging simulator was developed to generate a precise simulation of objects in the field of view of synthetic aperture radar [33]. The range-Doppler plots for the back-scattered sea clutter and ship echoes for high-frequency surface wave radar were developed and validated with radar trials [34]. A relatively simple method for precise simulation of the three-dimensional geometry of objects in the environment in synthetic aperture radar was proposed in [33].

In recent years, there has been very little literature on radar hardware and radar system modelling. An incoherent scatter radar simulation system using a modular design concept was developed [35]. An introductory pulsed Doppler radar system simulation using MATLAB and Simulink with the implementation of a few components was developed [36]. A signal level simulator consisting of algorithms for the simulation of raw radar return signals was discussed in [37]. Detailed MATLAB codes for finite difference time domain (FDTD) modelling of ground penetrating radar were discussed in [38]. A frequency-modulated continuous wave (FMCW) radar system simulation was developed to explore the impact of phase noise on target signal detection [39].

Even though there are instances of radar modelling in literature, to the author's best knowledge, all the models are focused on specific aspects of radars. The focus could be

either modelling the radar environment or limited hardware building blocks. The literature primarily needs a whole radar model with all system-level hardware components in the transmit chain, the receive chain, and the data processing chain, along with modelling of the radar environment. A comprehensive radar model consisting of all fundamental hardware building blocks, validated by comparing the simulated data with data from actual staring radar measurements, can be a powerful tool to model different radar scenarios.

1.2.4 Phase noise in radars

Noise in electronic systems has been studied since the early 20^{th} century. The thermal noise was initially reported in 1918 by Shottky [40], who observed that the noise has a flat spectrum [41]. The experiments were soon followed by Johnson, who observed that the noise did follow a flat spectrum at low frequencies and showed the presence of the Flicker effect [42, 43]. The thermal noise was further studied by Johnson and Nyquist between 1927 and 1928 [44–46]. Phase noise is the random and unwanted fluctuations in the phase of an oscillator in the frequency domain resulting in the broadening of the oscillator spectrum [47, 48]. The phase noise in oscillators and radar systems was first discussed between 1964 and 1966 as part of an Institute of Electrical and Electronics Engineers (IEEE) standards project and an IEEE-NASA symposium intended to unify definitions of frequency stability in both time and frequency domain [49–51].

Over the past few decades, the phase noise in oscillators has been studied in detail [52–55]. Radar oscillators constitute a significant source of phase noise in radar systems [56]. The effects of phase noise on the performance of radar and radar sub-systems were analysed in [57]. In FMCW radars, phase noise affects the spatial resolution and maximum range [58]. The phase noise also results in spectral broadening of the target responses in FMCW radar systems [59]. In Doppler radars, the phase noise exceeds the receiver thermal noise floor

and is a fundamental limit to the system's signal-to-noise ratio (SNR). The increased phase noise floor can limit the target detection capability of radar by masking slowly moving low radar cross-section (RCS) targets, especially in the presence of strong clutter [60]. Radar oscillators with lower phase noise can potentially overcome the limitations and thereby detect slowly moving targets with weak echos [60–62], even in the presence of extreme urban clutter. Radars with low phase noise oscillators also have applications in the classification of radar targets, including drones and birds [63, 64].

Despite being the fundamental limit on the performance of radars under high clutter, as demonstrated in this subsection, to the best of the author's knowledge, rarely few literature explore the effects of oscillator phase noise in radar systems and the potential of using oscillators with low phase noise levels.

1.3 Motivation

As evidenced in the literature survey and as demonstrated in chapter 5, the phase noise of radar oscillators is a significant factor in radar target detection. The oscillator phase noise results in the phase noise floor emerging out of the thermal noise floor, masking slowly moving low-RCS targets in strong clutter.

The clutter-induced phase noise floor can be reduced by using low phase noise oscillators, and the radar community is constantly searching for radar oscillators with low phase noise. Quantum oscillators, including optical atomic clocks, are the most stable frequency sources available today [65, 66]. The best laboratory-based quantum oscillators exhibit fractional frequency instabilities and uncertainties in the range of 10^{-18} and below [67, 68]. The optical signals at the output of quantum oscillators can be down-converted to radio frequency (RF) using a frequency comb without compromising stability, accuracy, and phase

noise [69]. The quantum oscillator, down-converted to RF, exhibits ultra-low phase noise levels, as demonstrated in chapter 4. Such a quantum oscillator can be the solution to a radar oscillator with very-low phase noise.

Even though there are instances in literature where classical oscillators with low phase noise levels are studied [70], literature that explores the possibility of replacing conventional radar oscillators with quantum oscillators is minimal [71]. We have proposed the use of quantum oscillators as a potential oscillator candidate in radars [60, 72]. Also, no literature covers the development of a quantum-enabled radar (either in simulation or reality) with low phase noise quantum oscillators with the potential to detect slowly moving low RCS targets even in strong clutter environments.

An efficient approach to studying the effects of phase noise in radar systems and exploring the possibility of employing quantum oscillators as radar oscillators are using radar modelling, similar to the comprehensive radar model that will be discussed in chapter 3. Radar modelling is also helpful for investigating the fundamental limitations of different radar building blocks. As shown in the literature survey, despite the fact that there are several examples of radar modelling, the literature primarily lacks a comprehensive radar model that includes all of the critical hardware radar building blocks.

The research work discussed in the thesis covers the effects of oscillator phase noise in target detection. The thesis uses the radar model, validated using the experimental results from the L-band staring radar, to develop quantum-enabled radar in simulation and to compare the performance of classical and quantum-enabled radars. The thesis also covers the first realisation of a quantum-enabled radar in simulation, with the phase noise floor almost identical to the thermal noise floor for the specific clutter environment used in the simulation. The quantum-enabled radar described in the thesis is capable of detecting smaller targets in the presence of strong urban clutter.

1.4 Original contributions

The following are the original contributions of this work:

1. A radar model that represents the response of fundamental hardware building block in the transmit chain, the receive chain, and the data processing chain, formulated and validated with experimentally measured results from a commercially available L-band staring radar (Chapter - 3, pages - 43 to 101).
2. A comprehensive measurement of phase noise, showing a quantum oscillator with phase noise values at least 20 dB lower for every offset frequency in comparison to the L-band staring radar at the transmit frequency (Chapter - 4, page - 135, figure - 4.18).
3. A high fidelity replication of range-Doppler plot from experimentally measured results of the L-band staring radar in simulation, with an emphasis on phase noise, showing phase noise floor at least 25 dB above the thermal noise floor for range bins with the highest clutter (Chapter - 5, pages - 146 and 147, figures - 5.3 and 5.4).
4. The first realisation of a quantum-enabled radar with low phase noise quantum oscillator in simulation, with phase noise floor very close to thermal noise floor in range bins with high levels of clutter in the simulation environment (Chapter - 5, pages - 151 and 153, figures - 5.6 and 5.7).
5. Detection plots showing a low-RCS target that fails to get detected in high clutter range bins with the L-band staring radar in simulation getting detected in all the range bins with the quantum-enabled radar in simulation (Chapter - 5, pages - 150 and 154, figures - 5.5 and 5.8).

These original contributions have led to journal and conference publications and are listed in the section 1.5.

1.5 Publications

The following papers have been published during this PhD work:

1. Mohammed Jahangir, Jonathan M. Jones, Jithin Kannanthara, Chris J Baker, Kai Bongs, Michail Antoniou, Yeshpal Singh, "Development of Quantum Enabled Staring Radar with Low Phase Noise", *2021 18th European Radar Conference (EuRAD)*, London, 2021, pp. 225-228

2. Jonathan M. Jones, Darren Griffiths, Jithin Kannanthara, Mohammed Jahangir, Michail Antoniou, Christopher Baker, Kai Bongs, Yeshpal Singh, "Quantum Enabled Radar Sensing", *2022 IEEE International Topical Meeting on Microwave Photonics (MWP)*, Virtual conference, 2022, pp. 1-4

3. Darren Griffiths, Mohammed Jahangir, Jithin Kannanthara, Chris J Baker, Michail Antoniou, Yeshpal Singh, "Direct Signal Synchronization for Staring Passive Bi-Static Radar", *2022 IET International Radar Conference*, Edinburgh, 2022 (Accepted)

4. Maximilian Bradler, Maurice Lessing, Benjamin Sprenger, Marc Fischer, Michele Giunta, Ronald Holzwarth, Jonathan M. Jones, Darren Griffiths, Jithin Kannanthara, Mike Antoniou, Chris Baker, Mohammed Jahangir, Yeshpal Singh, Kai Bongs, "Photonic Microwave Generator as Quantum-enabled Local Oscillator for Radars", *2022 European Frequency and Time Forum and IEEE International Frequency Control Symposium (EFTF-IFCS)*, Paris, 2022 (Accepted)

5. Jithin Kannanthara, Darren Griffiths, Mohammed Jahangir, Jonathan M. Jones, Chris J. Baker, Michail Antoniou, Colin J. Bell, Henry White, Kai Bongs, Yeshpal Singh, "Whole System Radar Modelling: Simulation and Validation", In: *IET - Radar, Sonar & navigation*, 2023 (Accepted)

6. Darren Griffiths, Mohammed Jahangir, Gwynfor Donlan, Jithin Kannanthara, Michail Antoniou, Chris Baker, Yeshpal Singh, "Oscillator Synchronization Measurements Campaign for Network Radar Systems", *2023 IEEE International Frequency Control Symposium and the European Frequency and Time Forum (IEEE IFCS-EFTF)*, Toyoma, 2023 (Submitted)

1.6 Thesis outline

This thesis details the simulations, and experimental work carried out towards the advanced modelling of a quantum-enabled radar at the University of Birmingham. The thesis starts with a brief introduction to different aspects of the radar in chapter 2. The radar fundamentals and the background knowledge required for the thesis are discussed in chapter 2. A detailed discussion of radar modelling is presented in chapter 3. The chapter on radar modelling includes the construction of each radar hardware building block in the MATLAB/Simulink simulation platform and the theory associated with different radar building blocks. The mathematical model of the signal and the SNR at the output of each building block is also provided. The chapter 3 also consists of the validation of the simulated radar model with the results from actual staring radar measurements.

Chapter 4 consists of the characterisation of the oscillators. The phase noise and the Allan deviation are used as the two figures of merits for oscillator characterisation. Methods to measure the figure of merits, measurement results and the comparison of the performance of different oscillators (both classical and quantum) are discussed in chapter 4. In chapter 5, the reader is introduced to the modelling of quantum-enabled radar. The validated radar model from chapter 3 and the phase noise results from the measurement campaign in chapter 4 are used to develop the quantum-enabled radar in simulations. Chapter 5 also includes

a detailed discussion of the limitations of oscillator phase noise in target detection and a comparative study of the advantages of quantum-enabled radar over classical radar with respect to phase noise. Chapter 6, the final chapter, summarises the work in all the previous chapters and concludes the thesis. The potential of the research carried out in the thesis, and future work is also discussed in the final chapter.

Chapter Two

FUNDAMENTALS OF RADAR

Building on the introduction provided in chapter 1, this chapter describes the radar basics that will be developed and refined in chapter 3 on radar modelling. This chapter presents the reader with the relevant background information and theory behind radar systems. The chapter starts with a discussion on the basic radar configuration, followed by a discussion on the fundamental parameters and equations relevant to radars. The chapter also discusses the different kinds of noises in radar systems.

2.1 Basic radar configuration

This section briefly introduces radar architecture, including the different components of radar and the characterisation of the radar signal in the time and frequency domain. Radar works on the principle of transmission, reflection, and detection of electromagnetic waves. The configuration of a radar system depends on the application for which the radar is used. Generally, a radar consists of three subsystems: a transmit chain, a receive chain, and an environment, as illustrated in figure 2.1. In basic terms, the transmit chain consists of a transmitter, and a transmit antenna and the receive chain consists of a receiver and a

receive antenna. The environment contains targets, along with the clutter, including natural and artificial physical landscapes, weather, and electromagnetic signals.

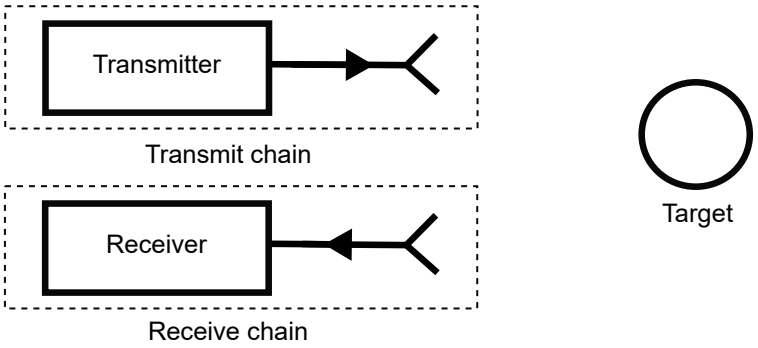

Figure 2.1: The basic configuration of a radar consists of transmit chain, receive chain and environment. The transmit chain consists of a transmitter and a transmit antenna. The receive chain consists of a receiver and a receive antenna. The environment contains targets, along with other artificial and natural terrain features and electromagnetic signals.

2.1.1 Transmit chain

The transmit chain in the radar system serves the purpose of generating and transmitting the radar transmit signal. The transmit chain requirements depend on the transmit signal. The characterisation of the transmit signal in the frequency and time domain, the basic architecture of the transmit chain in a radar system, and the different types of radar systems based on the transmit signal and transmit chain architecture are discussed below.

2.1.1.1 Transmit signal: Frequency domain

The electromagnetic transmit signal in the radar systems spans a wide range of RF from a few MHz up to a few 100s of GHz [73, 74]. There are exceptions, including light detection and ranging (LIDAR) systems with frequencies in the optical domain [75]. IEEE has divided the range of RF into different frequency bands [76]. The IEEE standard RF letter-band nomenclature for the frequency bands and the corresponding frequency values

are summarised in the table 2.1.

Frequency band	Frequency range
HF	3 - 30 MHz
VHF	30 - 300 MHz
UHF	300 - 1000 MHz
L	1 - 2 GHz
S	2 - 4 GHz
C	4 - 8 GHz
X	8 - 12 GHz
K_u	12 - 18 GHz
K	18 - 27 GHz
K_a	27 - 40 GHz
V	40 - 75 GHz
W	75 - 110 GHz
mm	110 - 330 GHz

Table 2.1: IEEE standard RF letter-band nomenclature for the frequency bands and corresponding frequency range [76]

2.1.1.2 Transmit signal: Time domain

The time domain characteristics of the radar transmit signal are as important as the frequency domain characteristics of the transmit signal. A radar system can be divided into continuous waveform (CW) radar and pulsed waveform radar based on the type of transmitted signal. A typical CW and pulsed signal is given in figure 2.2. In CW radars, the signal is transmitted continuously, as shown in figure 2.2a. In a pulsed waveform radar, the signal is transmitted in short bursts of pulses followed by a brief period of no signal transmission, as shown in figure 2.2b. The significant parameters in the time domain are pulse width, pulse repetition interval (PRI), pulse repetition frequency (PRF), and duty cycle. The pulse width is the time duration for a single pulse and is denoted by τ. The PRI is the time difference between the start of two adjacent pulses. The PRF is the inverse of the PRI and denotes the number of pulses in a second. The duty cycle of the transmitted pulse is the ratio between the pulse width and the PRI.

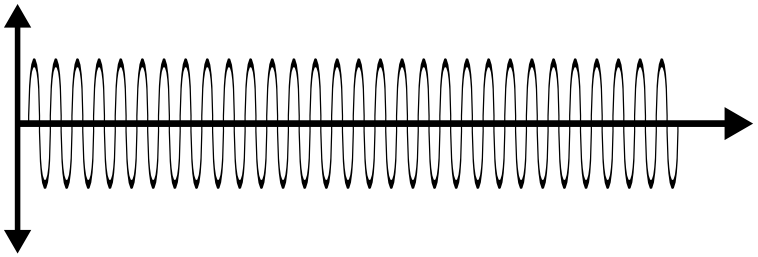

(a) Typical signal at the output of a CW waveform radar

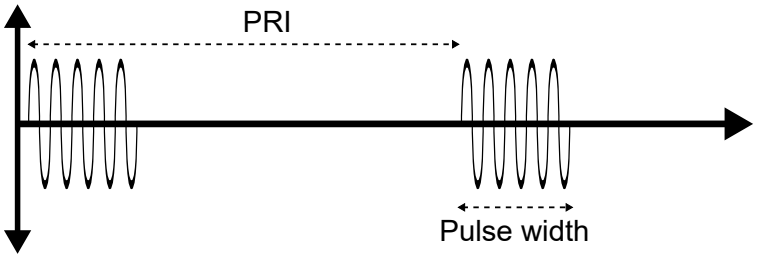

(b) Typical signal at the output of a pulsed waveform radar. The PRI is the time difference between the start of two adjacent pulses, and pulse width is the length of a single pulse.

Figure 2.2: Typical signals at the output of a CW and pulsed waveform radar.

Due to their constant operation, CW radar systems are typically less complex than pulsed radars in terms of hardware and signal handling. However, the massive difference in transmitted and received signal power complicates the CW radar design and makes target detection challenging. The lack of simultaneous operation of the transmit and receive antenna in a pulsed radar system makes it simpler to detect a target return at the expense of more sophisticated hardware and signals. A pulsed radar can either be coherent or non-coherent. In radars, coherence describes the phase relationship between the transmitted pulses. Coherent pulsed radars have a deterministic phase relationship from pulse to pulse. Meanwhile, a non-coherent pulsed radar does not follow a constant phase relationship between the pulses. Since coherent radars compare the phase of the received pulse with the phase of the transmitted pulse, even small phase shifts arising from the movement of the targets can be detected [77].

2.1.1.3 Transmit signal: Modulation

Signal modulation is defined as the modulation of the properties of the transmit signal with the help of a modulating signal. In general, some modulation to the transmit signal is needed to estimate a target's range. The signal modulation is applicable for both the pulsed and the CW radar. It can be amplitude modulation, frequency modulation, phase modulation, or a combination of the modulation types. For a pulsed radar system, the modulation can either be constant throughout all the pulses or can be applied within individual pulses. The most common modulation in CW radars is the frequency modulation resulting in FMCW radars.

2.1.1.4 Transmit chain architecture

In a typical radar system, the transmit chain consists of a transmitter to generate the transmit signal and an antenna to radiate the transmit signal. The transmitter can be generally divided into two categories: power oscillator transmitter and power amplifier transmitter. The high-power transmit RF signal is directly generated in the power oscillator transmitter. In the power amplifier transmitter, the RF signal is initially synthesised at low power and is amplified using a power amplifier (PA) to the required transmit power. The power oscillator transmitters generally consist of a magnetron or a similar self-oscillating device to generate the high-power RF signal, as shown in figure 2.3a.

The power amplifier transmitters typically consist of stable frequency references known as local oscillators (LO) to provide the LO signal. In power amplifier transmitters, the modulated baseband signal is mixed and frequency up-converted using the LO signal to generate the required transmit RF signal. Within the power amplifier transmitter architecture, the low-power RF signal is generated using a single stage of frequency up-conversion or multiple

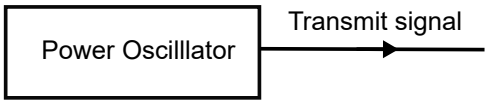

(a) Layout of a power oscillator transmitter consisting of a power oscillator to directly generate the high-power RF transmit signal.

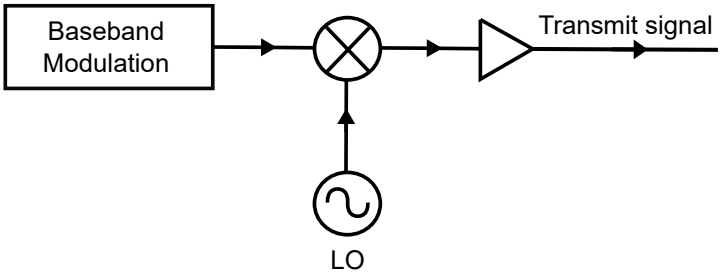

(b) Layout of a homodyne power amplifier transmitter. The baseband signal undergoes a single stage of frequency up-conversion followed by amplification to generate the high-power RF transmit signal.

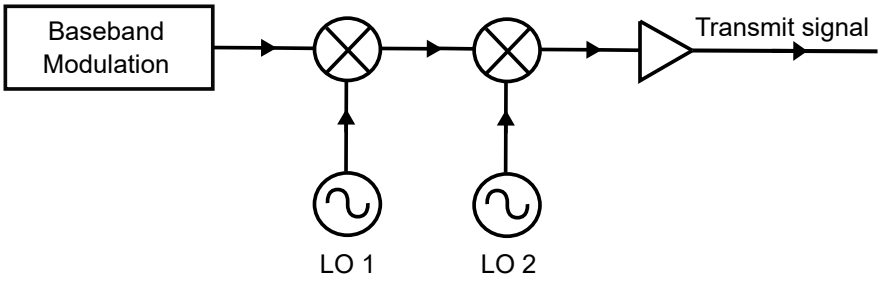

(c) Layout of a heterodyne power amplifier transmitter. The baseband signal undergoes multiple stages of frequency up-conversion followed by amplification to generate the high-power RF transmit signal.

Figure 2.3: The general radar transmitter architecture includes the power oscillator transmitter and power amplifier transmitter.

stages of frequency up-conversion. In homodyne power amplifier transmitters, as shown in figure 2.3b, the baseband signal undergoes a single stage of frequency up-conversion. In heterodyne power amplifier transmitters, as shown in figure 2.3c, the signal undergoes multiple stages of frequency upconversion. Modern radar systems generally produce their initial signal at an intermediate frequency (IF) and are mixed with the LO signal to generate the

RF signal.

When it comes to stability, the power amplifier transmitter outperforms the power oscillator transmitter. The power oscillator transmitters are self-oscillating devices that tend to be non-coherent from pulse to pulse, resulting in lower stability. The power amplifier transmitter generally consists of low-power phase coherent components locked to an external reference clock, resulting in higher stability than the power oscillators. The transmitter architectures are not limited to the general architectures mentioned and can vary in design and complexity depending on the radar design and transmit signal specifications.

The antenna in the transmit chain radiates the generated RF signal to the environment. There are different kinds of system architectures based on radar antennas. The transmit antenna can either be a single antenna that serves the purpose of both the transmission and the reception of the RF signal, a separate stand-alone antenna for only the transmission of the RF signal, or an array of antennas. In a single transmit/receive antenna radar system, as shown in figure 2.4a, a circulator is used to isolate the transmit and receive chains. During transmission, the circulator connects the transmitter to the antenna, and during reception, the circulator connects the receiver to the antenna. Since the transmit signal power is several orders of magnitude higher than the receive signal power, the isolation between the transmit chain and receive chain is crucial for the efficient detection of the received signal. CW radar systems generally avoid the single transmit/receive antenna radar system. When separate transmit and receive antennas are used, as shown in figure 2.4b, there will be inherent isolation between the transmit chain and the receive chain.

The transmit antenna can also consist of an array of antenna elements in many of the recent applications. The transmit and the receive antenna can share the antenna array or can use a separate antenna array. Based on the location of the transmit and receive antennas, the radar systems can be divided into mono-static, bi-static, and multi-static radars. Radar

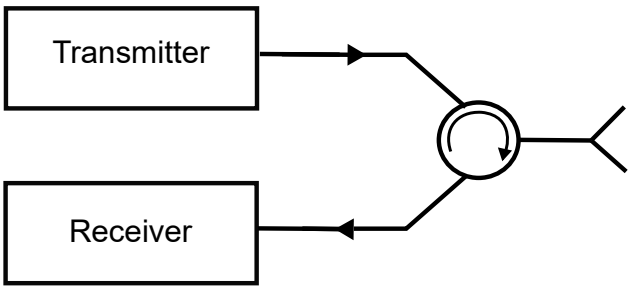

(a) Radar architecture with a single antenna for both the transmission and reception of the RF signal. A circulator is used to isolate the transmit chain and the receive chain.

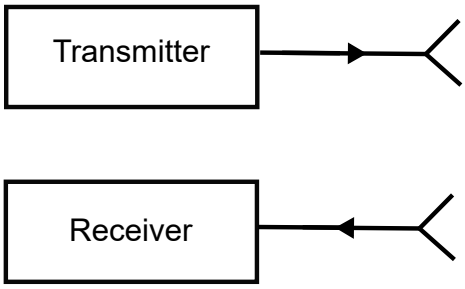

(b) Radar architecture with a separate antenna for transmitting and receiving the RF signal.

Figure 2.4: Radar system architecture based on antennas

systems with both the transmit and receive antennas co-located are known as mono-static radar. The transmit and the receive antennas are physically separated by distance in bi-static radars. The multi-static radar system consists of multiple spatially separated mono-static or bi-static radars with a shared radar coverage area.

2.1.2 Environment

The transmit signal generated by the transmitter is radiated to the environment by the transmit antenna. The environment contains objects that can be defined as targets; it also contains the physical landscape and weather, which are more described as types of clutter. The environment also contains the medium of propagation. The propagation

medium is usually the atmosphere, and electromagnetic transmit signal interacts with the targets, clutter, and atmosphere. Electromagnetic waves interact in different ways, including absorption, scattering, reflection, refraction, and diffraction. Absorption is the phenomenon where an object absorbs the energy of the incident electromagnetic waves and converts it into another form of energy, typically heat [78]. Scattering is the phenomenon where the incident electromagnetic waves are absorbed by the objects and re-radiated in multiple directions [79]. Reflection happens when an object reflects a portion of the incident electromagnetic wave [80]. Refraction occurs when an electromagnetic wave passes from one medium to another. Refraction causes electromagnetic radiation to bent due to the difference in the refractive index of the medium, causing a difference in the speed of the electromagnetic wave [81]. Diffraction is the phenomenon where a beam of electromagnetic wave spreads out, passing through a narrow aperture or across an edge [82].

The transmit signal radiated by the radar transmit antenna propagates towards the targets and clutter through the atmosphere, where the signal gets attenuated due to atmospheric absorption. On hitting the target, some of the transmit signal energy gets reflected towards the radar receive antenna. The signal reflected by the targets and clutter gets further attenuated while propagating through the atmosphere towards the radar receive antenna. The RCS of a target, a measure of the target's ability to reflect the transmit signal, defines the amount of transmit signal reflected towards the radar. The RCS of a target is different from the physical cross-section of the target. The RCS depends on several parameters, including the target's size, shape, material, and orientation [83]. The RCS is also dependent on the frequency of the transmitted signal [84].

2.1.3 Receive chain

In a radar system, the reflected signal from the targets and clutter are received and processed by the receive chain. The receive chain consists of the receive antenna to collect the reflected signal from the target and a receiver to process the received signal. Generally, the radar receiver amplifies, filters, and down-converts the received signal [85] to an IF or baseband signal before performing data processing of the signal.

2.1.3.1 Receive chain architecture

The radar receiver typically consists of three subsections: RF front-end, IF block, and data processing block, as shown in figure 2.5. The major components in the RF front

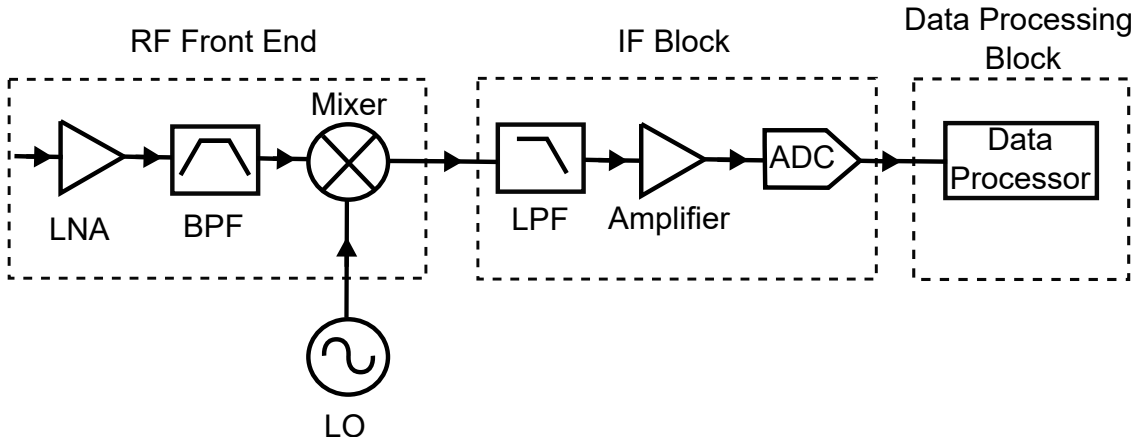

Figure 2.5: The basic architecture of a radar receive chain consists of an RF front end, an IF block and a data processing block. The RF front end amplifies, filters and down-converts the received RF signal. The IF block performs the function of filtering, amplifying, and digitising the IF signal. The digitised signal goes through different processing stages in the data processing chain.

end are the low noise amplifier (LNA), band-pass filter (BPF), and down-converter. The LNA performs the function of amplification of both the signal and the noise. There are different kinds of noise in a radar system, which are discussed in detail in section 2.3. A perfect noiseless LNA will have an SNR the same at both its input and its output. In reality,

an LNA adds extra noise and decreases the SNR at the output of the LNA. The lower the additional noise it adds, the better the performance of an LNA. The BPF after the LNA is used to remove the out-of-band receiver noise and the out-of-band signal, thereby increasing the SNR. The BPF restricts both the signal and the noise to a specific RF bandwidth. The downconverter is used to frequency down-convert the filtered RF signal to the IF band. The frequency downconversion is generally performed by mixing the RF signal with a LO signal. In a coherent radar system, the LO used to down-convert the received RF signal is phase coherent with the LO present in the transmit chain.

After down-conversion, the signal is transferred to the IF block, where the signal undergoes further stages of filtering, amplification, and digitisation. In modern radars, the ADC samples the IF signal and the conversion to the baseband is performed digitally in the data processing block. The low-pass filter (LPF) in the IF block function as an anti-aliasing filter and removes all the frequencies lower than half the sampling rate of the ADC. The anti-aliasing filter is used to follow the Nyquist criteria, discussed in detail in section 3.4.

The data processing block performs the function of down conversion of the digital IF signal to the baseband. The data processing block also calculates the target information, including range, velocity, and angle relative to the radar. The processing methods employed in the data processing block depend on the radar application. In addition to the general radar receiver components, the RF front-end can also include a limiter to protect the radar receiver from high-power received signals.

2.2 Basic radar parameters

With the basic configuration of the radar defined in section 2.1, the basic equations and definitions relevant to radars are described in this section. The section briefly discusses

the radar range equation, maximum unambiguous range, minimal measuring range, and range and Doppler resolution.

2.2.1 Radar range equation

The performance of a radar is dependent on the amount of reflected signal that reaches the receive antenna. The properties of the transmit signal, the target, and the environment determine the signal power at the receive antenna. The radar range equation provides the received signal power after the receive antenna and is [86],

$$P_R = \frac{P_T G_T G_R \lambda^2 \sigma L}{(4\pi)^3 R^4}, \tag{2.1}$$

where P_T is the transmitted signal power, G_T is the transmit antenna gain, G_R is the receive antenna gain, λ is the wavelength of the transmitted signal, σ is the RCS of the target, L is the atmospheric loss factor, and R is the target range. The atmospheric loss factor is the measure of the signal attenuation during the propagation of the transmit signal through the atmosphere.

2.2.1.1 Maximum detectable range

The radar range equation can be used to determine the maximum detectable range for a radar system. The maximum detectable range is the target range for which the power of the received signal is at its minimum detectable value. The maximum detectable range ($R_{\max}$) is given by,

$$R_{max} = \left(\frac{P_T G_T G_R \lambda^2 \sigma L}{(4\pi)^3 S_{min}} \right)^{1/4}, \tag{2.2}$$

where S_{min} is the minimum detectable received signal power.

2.2.1.2 Dynamic range

The radar receiver must be able to handle strong signals from short-range targets and surface reflections as well as pick up weak signals close to the noise floor. The dynamic range (DR) at the detection point is defined as the ratio of the maximum detectable signal power (S_{max}) to the minimum detectable signal power (S_{min}) and is given by,

$$DR = \frac{S_{max}}{S_{min}}, \tag{2.3}$$

where S_{max} is governed by the components in the receive chain and the maximum receivable signal power. The S_{min} must be above the receiver noise level and is governed by the radar detection threshold.

2.2.1.3 Received SNR

Another common parameter in the radar is received SNR, which is the ratio between the received signal power and noise power. In the received SNR calculation, the received signal power is calculated from the radar range equation, the equation 2.1. The main source of noise in the receiver is thermal noise generated within the radar receiver. The thermal noise power is given by,

$$N = k_B T B, \tag{2.4}$$

where N is the thermal noise power, k_B is the Boltzmann's constant, T is the temperature, and B is the noise bandwidth. The received SNR (SNR_R) is given by,

$$SNR_R = \frac{P_T G_T G_R \lambda^2 \sigma L}{(4\pi)^3 R^4 k_B T B}. \tag{2.5}$$

The receiver SNR is one of the parameters generally used to describe the performance of a radar system.

2.2.2 Maximum unambiguous range

For a pulsed radar, the target range is calculated from the time taken for a single transmit pulse to reach the receiver after reflection from the target. As a result, if the time it takes for a transmit pulse to return to the receive antenna exceeds the time between successive pulses, there is insufficient information to distinguish which of the transmit pulses is the source of the reflected signal, and the target range becomes ambiguous. The maximum unambiguous range provides the upper limit to the range of a radar that can be measured with certainty. The maximum unambiguous range is given by,

$$R_M = \frac{c(PRI - \tau)}{2}, \tag{2.6}$$

where c is the speed of light, and τ is the pulse width. Targets beyond the maximum unambiguous range appear as ghost targets with incorrect range information. The pulse width in the equation 2.6 indicates the requirement of the complete reflected signal to be received for target detection.

2.2.3 Minimal measuring range

In a pulsed radar, since the transmit and receive antennas are not operated simultaneously, the reception of the reflected signal is not possible during transmission. The minimal measuring range is the minimum distance below which a target cannot be detected. The

minimal measuring range (R_{min}) is related to the pulse width and is given by,

$$R_{min} = \frac{c\tau}{2}. \tag{2.7}$$

2.2.4 Doppler

In general, the Doppler effect is the change in the observed frequency of a wave due to the relative motion of the observer and source [87]. In radars, for a target moving towards or away from the radar, the frequency of the reflected signal from the target shifts compared to the frequency of the transmit signal. The frequency shift of the RF signal due to the relative motion of the radar target is known as the Doppler frequency shift. The Doppler frequency shift is used to measure the velocity of a moving target. For a stationary radar observing a moving target, the Doppler frequency shift (f_D) is,

$$f_D = \frac{2v\cos\delta}{\lambda}, \tag{2.8}$$

where δ is the Doppler angle, $v\cos\delta$ is the target's velocity in the radar's direction, and λ is the wavelength of the transmit signal. Doppler angle is the angle between the line of sight from the radar to the target and the direction of the target's motion.

2.2.5 Resolution

The resolution defines how well a radar can differentiate a target in range and velocity. The resolution in the range is known as range resolution, and the resolution in Doppler is known as Doppler resolution. The resolution is one of the key parameters in the technical datasheet of a radar.

2.2.5.1 Range resolution

The ability of a radar system to differentiate between two or more objects in various ranges is known as the range resolution. Two identical targets at the same distance from the radar cannot be resolved in range. The degree of range resolution depends on the transmitted pulse width. For a radar system, with all other factors at maximum efficiency, two targets separated by a distance equivalent to one-half of pulse width can be resolved. The theoretical range resolution (ΔR) for a pulsed radar system is given by,

$$\Delta R = \frac{c\tau}{2}. \tag{2.9}$$

For a pulsed radar system with frequency modulation, the bandwidth (BW) of the frequency modulation is equivalent to the inverse of the pulse width and is given by,

$$BW = \frac{1}{\tau}. \tag{2.10}$$

Using equation 2.9 and 2.10, the theoretical range resolution for a frequency-modulated pulsed radar system becomes:

$$\Delta R = \frac{c}{2BW}. \tag{2.11}$$

Hence, the range resolution of a radar system can be improved by using a shorter pulse and introducing frequency modulation. The shorter pulse implies less energy on the target resulting in reduced detection, which is compensated by frequency modulation.

2.2.5.2 Doppler resolution

The ability of a radar system to differentiate between two or more targets located in the same range and moving with different Doppler velocities is known as Doppler resolution.

The Doppler frequency resolution is equivalent to the inverse of the integration time, the duration for which the radar is looking at the target. The Doppler frequency resolution is given by,

$$\Delta f_d = \frac{1}{T_c}, \tag{2.12}$$

where Δf_d and T_c is the Doppler frequency resolution and integration time respectively. Using equation 2.8, the Doppler velocity separation required for two targets to be resolved is,

$$\Delta v = \frac{\lambda}{2T_c \cos(\delta)}, \tag{2.13}$$

where Δv is the Doppler velocity resolution. The Doppler velocity resolution can be improved by increasing the duration for which the radar is looking at a target.

2.3 Noise in radars

Noise is inevitable in any electronic circuit. The desired scenario in designing an electronic circuit is to reduce the noise to the minimum possible value. There are different kinds of noise in any radar system, and they can be broadly classified into internally generated noise and external noise. This section discusses the crucial noises present in radar systems.

2.3.1 Internally generated noise

The internally generated noise in the radar systems is the noise generated within the radar and includes thermal noise, flicker noise, shot noise, and phase noise. In this subsection, a detailed description of each of the internally generated noises in radar systems is provided. Another important internal noise is the quantisation noise from ADC which is discussed in detail in section 3.4.5.1.

2.3.1.1 Thermal noise

Thermal noise is present in any electronic device. The thermal noise is proportional to the temperature and is inevitable in any electronic device above the temperature of 0 K. In radars, the thermal noise is created by the thermal agitation of electrons in the various components that make up the radar receiver [88]. The thermal noise is also proportional to the receiver noise bandwidth. The thermal noise power is given by the equation 2.4. The thermal noise can never be eliminated; it can be reduced by reducing the temperature or receiver noise bandwidth. Thermal noise has a uniform distribution over the frequency spectrum with a Gaussian distribution of levels and hence is also known as white Gaussian noise [89].

2.3.1.2 Flicker noise

The flicker noise is present in all semiconductor-based electronic devices. The charge carriers that are randomly trapped and released between the interfaces of two materials are attributed to be the source of the flicker noise [90]. Unlike thermal noise, flicker noise is dependent on the frequency, and the spectrum of the flicker noise is,

$$S(f) \propto \frac{1}{f}. \tag{2.14}$$

The flicker noise occurs at low frequencies and decreases with frequency, exhibiting the $1/f$ characteristic. Hence, the flicker noise is also known as $1/f$ noise or pink noise. At higher frequencies, the flicker noise is overshadowed by the thermal noise. In oscillators, flicker noise stays close to the carrier frequency and plays a significant role in the contribution of phase noise.

2.3.1.3 Shot noise

The source of the shot noise is similar to the flicker noise. The shot noise is attributed to the random fluctuation of the noise current generated when a current flows across the interface of two materials in a semiconductor. Similar to thermal noise, shot noise is also a white noise with Gaussian distribution.

2.3.2 External noise

In radars, external noises are noises with a source external to the radar and solely depend on the signals received by the antenna. Similar to internally generated noise, a radar designer also needs to take good care of the external noise sources. There are noises as well as interference that affect the performance of a radar system. The primary sources of external interference are:

- Interference from radars operating in the same frequency band, causing the appearance of ghost targets. Ghost targets are caused by the presence of multiple indirect reflections from other radar sources in the vicinity, which results in more than one target signature for a single target.
- Jammers in the form of electronic countermeasures that intentionally sends out radio frequency signals to interfere with the operation of radar by saturating its receiver with noise or false signals

2.3.2.1 Sky noise

Sky noise is one of the crucial noises external to the radar. There are different sources that contribute to sky noise. When a receive antenna is directed at a thermal body, the

thermal body acts as a noise source with a corresponding noise temperature. The thermal bodies that contribute to the sky noise include the sun, the moon, and the earth. The rain, oxygen, and water vapour in the atmosphere attenuates the RF signal through absorption. Since absorption is a thermal process, these components in the atmosphere also contribute to the sky noise. The rest of the galaxy also contributes to the sky noise.

2.3.3 Phase noise

Phase noise is one of the very crucial internal noises in radar systems. Phase noise is the perturbation of phase in the frequency domain [91]. Phase noise plays a major role in the detection of radar targets. In this sub-section, a detailed theory of phase noise and the characteristics of phase noise are described.

2.3.3.1 What is phase noise

The mathematical model for the output of an ideal sinusoidal oscillator is given as,

$$s(t) = A_0 \sin(2\pi f t), \tag{2.15}$$

where A_0, f is the amplitude and the frequency of the oscillator output, respectively. However, the equation 2.15 is not valid in the real world. In the real world, the output of an oscillator can be better represented as,

$$s(t) = A_0(1 + \epsilon(t)) \sin(2\pi f t + \phi(t)), \tag{2.16}$$

where $\epsilon(t)$ and $\phi(t)$ represent the amplitude modulation and the phase modulation of the sinusoidal oscillator output. The amplitude modulation is the disturbance in the amplitude

of the signal and is also known as amplitude noise. Phase modulation is the disturbance in the frequency of the signal. The phase modulation due to random phenomena is called phase noise. Since a change in phase is always followed by a change in frequency, it is also possible to consider phase noise as frequency noise.

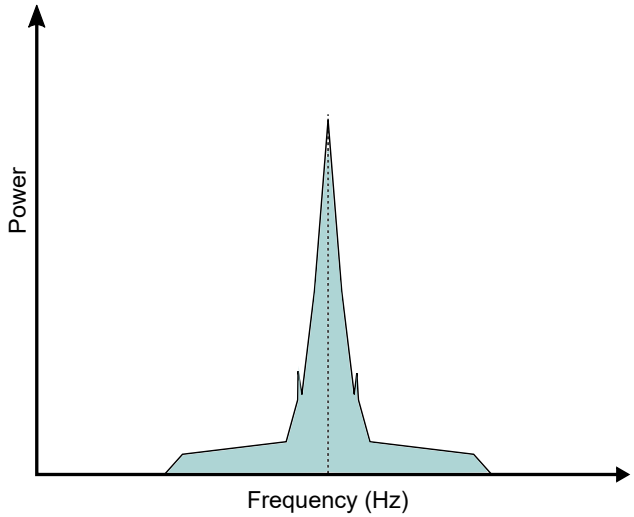

Figure 2.6: Simple illustration of the general spectrum of a real oscillator. The spectrum contains noise skirts on both sides of the carrier frequency and noise. The spectrum also consists of spurs due to anomalous frequency components.

The general spectrum of a real oscillator is shown in figure 2.6. Figure 2.6 shows the presence of noise skirts on both sides of the carrier frequency. In addition to the noise skirts, peaks caused by anomalous frequency components known as spurs are also present. The noise skirts are composed of both the phase noise and the amplitude noise. However, the phase noise and the amplitude noise behave to the changes differently. For example, a perfect limiter can remove all the amplitude noise, but the phase noise at the output of the limiter will be the same as the phase noise at the input of the limiter. In most of the circuits, there is an intrinsic limiting effect that takes care of the amplitude noise. Additionally, an oscillator itself will have a limiting effect and eliminate the amplitude noise, causing the phase noise to predominate in the oscillator's output. Hence the modified expression for the

output of a real oscillator with phase noise will be,

$$s(t) = A_0 \sin(2\pi f t + \phi(t)). \tag{2.17}$$

Since the phase noise is dominated at the output of a real oscillator, the noise skirts around the carrier in the figure 2.6 is often attributed to the phase noise.

Phase noise is generally defined in two ways. In the first definition, also the old definition, the phase noise is defined from the RF spectrum of the oscillator output signal. The phase noise appears as noise sidebands in the direct measurement of the RF spectrum of an oscillator. For an oscillator output signal, $s(t)$, the RF spectrum is defined as,

$$S_{RF}(f) = |\mathcal{F}[s(t)]|^2 = \mathcal{F}[R_s(\tau)] \tag{2.18}$$

where S_{RF} is the RF spectrum of the output signal, $\mathcal{F}$ denotes the Fourier Transform and $R_s(\tau)$ denotes the autocorrelation function of $s(t)$. The RF spectrum of an oscillator is illustrated in figure 2.7. Figure 2.7 shows the central peak of the oscillator RF spectrum with the noise sidebands.

In the old definition and the most common definition used by the manufacturers and the users of frequency standards, the phase noise is defined as the ratio of the noise power in one sideband of the signal RF spectrum at a certain offset frequency (for a 1 Hz bandwidth) to the total signal power (carrier plus sidebands) [92]. The single sideband phase noise, $\mathcal{L}(f)$, is given by,

$$\mathcal{L}(f) = \frac{\text{Noise power in one sideband per Hz at an offset frequency}}{\text{Total signal power}}. \tag{2.19}$$

The $\mathcal{L}(f)$ is usually expressed in decibels (dB) as $10\log(\mathcal{L}(f))$, and the units of phase noise are dB below the carrier frequency in a 1 Hz bandwidth and is generally written as dBc/Hz.

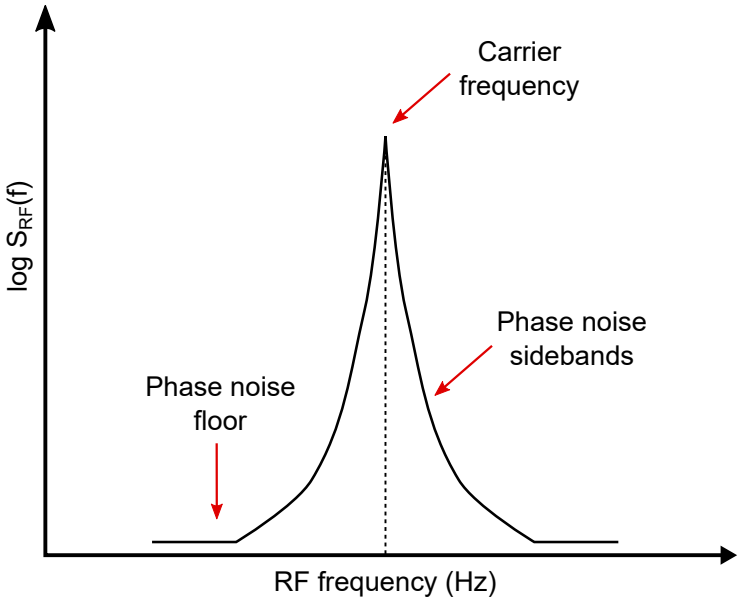

Figure 2.7: The RF spectrum of an oscillator with the central peak and the noise sidebands. The phase noise is defined as the ratio of the noise power in one sideband of the RF spectrum at a certain offset frequency (for a 1 Hz bandwidth) to the total signal power. The noise power approaches carrier signal power as the frequency approaches zero.

However, the limitation of using the RF spectrum to define the phase noise is that both the phase noise and the amplitude noise appear as sidebands in the RF spectrum. Hence, it is impossible to determine whether the sidebands correspond to amplitude noise or phase noise. To overcome the ambiguity, in the second and the latest definition, the phase noise is defined using the spectral density of phase fluctuations.

An RF power spectrum normalised to unity is known as power spectral density. The RF spectrum of an oscillator can be separated into two independent spectral densities: spectral density of phase fluctuations and spectral density of amplitude fluctuations. In most cases, the power spectral density of amplitude fluctuations is negligibly small, and the total modulations in the phase fluctuations are small, making the RF spectrum and the spectral density of phase fluctuations take approximately the same shape. The spectral density of

phase fluctuations, also called the phase noise spectrum, is denoted by $S_\phi(f)$, where f is the Fourier frequency. In the latest definition, phase noise is defined by IEEE as one-half of the spectral density of phase fluctuations [92],

$$\mathcal{L}(f) = \frac{s_\phi(f)}{2}. \tag{2.20}$$

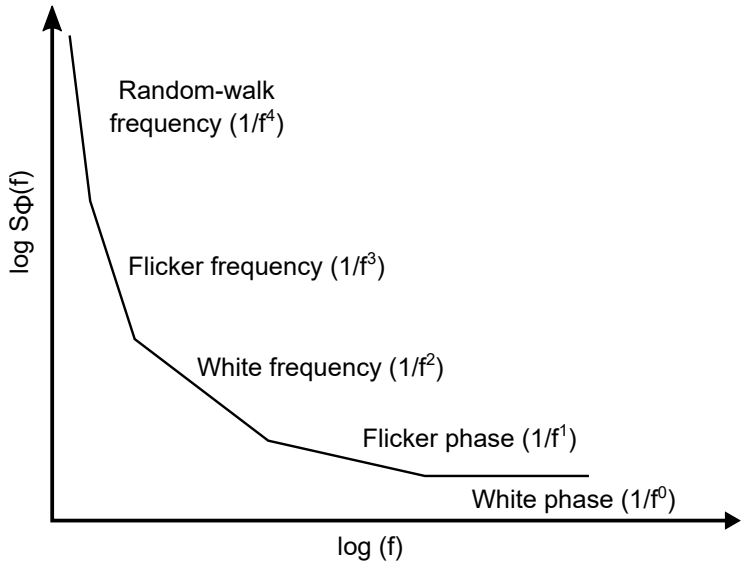

Figure 2.8: The general phase noise spectrum of an oscillator with different phase noise components [49]. Each of the phase noise components is associated with a specific noise colour. The noise power approaches infinity as the frequency approaches zero.

The units of $S_\phi(f)$ are rad^2/Hz. The phase noise spectrum is one-sided since the Fourier frequency ranges from 0 to ∞. Figure 2.8 shows the general phase noise spectrum of an oscillator. One of the noticeable differences between the phase noise spectrum and the RF spectrum is noise power as the frequency approaches zero. For the RF spectrum, the noise power approaches the carrier signal power as the frequency approaches zero. On the other hand, in the phase noise spectrum, the noise power approaches infinity as the frequency approaches zero.

2.3.3.2 Typical phase noise of an oscillator

The phase noise spectrum of an oscillator typically consists of several terms:

$$\mathcal{L}(f) \approx \frac{h_4}{f^4} + \frac{h_3}{f^3} + \frac{h_2}{f^2} + \frac{h_1}{f^1} + h_0 \tag{2.21}$$

Each power-law component in the equation 2.21 corresponds to different types of phase noise, as illustrated in figure 2.8. Conventionally a colour is also associated with different phase noise components. The table 2.2 summarises the phase noise type and the colour associated with each power-law component in the equation 2.21.

Term	Type of phase noise	Colour
$1/f^4$	Random walk frequency modulated phase noise	Brown/Red
$1/f^3$	Flicker frequency modulated frequency noise	Pink
$1/f^2$	White frequency modulated phase noise	White
$1/f^1$	Flicker phase noise	Blue
$1/f^0$	White phase noise	Purple/Violet

Table 2.2: The phase noise type and colour associated with different power law components of the phase noise [56, 93]

The most important of all the power law components is the $1/f$ term, and the research discussed in the thesis mainly focuses on the $1/f$, the Flicker phase noise. Most oscillators consist of the $1/f$ term at some significant frequency offsets. Many of the "ideal" oscillator phase noise spectrums use the $1/f^2$ term. The $1/f^4$ is often present in the phase noise spectrum for precision frequency standards at very low offset frequencies [94]. While plotting the dB values in the phase noise spectrum, the terms in the equation 2.21 correspond to slopes of -40 dB/decade, -30 dB/decade, -20 dB/decade, -10 dB/decade and constant. The fundamental limitations of phase noise in the performance of a radar system are discussed in detail in chapter 5. The different methods to measure the phase noise of classical and quantum oscillators are given in detail in section 4.4.

2.3.4 Jitter

While phase noise is the perturbation of a phase in the frequency domain, the perturbation of the phase in the time domain is known as the jitter. The jitter negatively impacts the performance of electronic devices, including radars. The jitter is crucial in ADC and digital-to-analogue converters (DAC) where sampling occurs.

2.3.4.1 Types of jitter

Jitter can be broadly classified into two types: random jitter and deterministic jitter. Random jitter is generally attributed to electronic thermal noise. The random jitter is unpredictable and has a normal distribution curve, hence is also known as Gaussian jitter. Random jitter is present in every electronic device with temperatures above 0 K. Deterministic jitter, on the other hand, is not random and does not follow a normal distribution. The deterministic jitter is often periodic and narrow band and hence is repetitious and can be predicted.

Jitter can also be classified as correlated jitter and uncorrelated jitter. The correlated clock jitter is caused by a noise source and is correlated to the noise source. The correlated jitter can be periodic or aperiodic. The uncorrelated jitter is not correlated to any identifiable noise source. The uncorrelated jitter is generally caused by intrinsic random thermal noise.

Chapter Three

RADAR MODELLING

Having presented the fundamentals of the radar in chapter 2, this chapter will now provide a detailed description of the development of a whole radar model and its comparison with the reference staring radar. The chapter begins with a discussion on the front end of the radar model simulated in the MATLAB/Simulink platform. The reader is then directed to the working principle of each radar building block in the transmit chain, receive chain, and data processing chain, along with the realisation of each building block within the simulation. Finally, the radar model is validated by comparing the simulated results with radar theory and the experimentally measured results from actual staring radar trials. The radar model discussed in this chapter will be used as a tool to explore the limitations of phase noise in radar systems and to develop simulations towards the realisation of the quantum-enabled radar in chapter 5.

3.1 Radar simulation front end

There are many radar architectures in the current world, and radar architecture depends on the application of the radar. Some common radar architectures include frequency-

modulated continuous wave radar, pulse Doppler radar, and pulse compression radar. A good radar model is a model that can simulate the building blocks in the transmit chain, receive chain and data processing chain, along with the target and clutter model of the environment. The radar model developed and discussed in this chapter is based on the L-band staring pulsed Doppler radar at the University of Birmingham with a reasonable number of simplifications and is focused on modelling the behaviour of the hardware building blocks.

There are several platforms where radar can be modelled, including MATLAB and LabVIEW. The radar model discussed in this chapter was developed from scratch in a bottom-up approach in MATLAB and the graphical interface of MATLAB, known as Simulink. Most of the building blocks in the radar were modelled in Simulink to develop a user-friendly radar model with the power to optimise every parameter based on the requirements. The front end of the simulated whole radar model is given in figure 3.1. The radar model can be divided into four major sections as follows:

- Transmit chain
- Environment
- Receive chain
- Data processing chain

The components within the transmit chain, the environment, and the receive chain were modelled as separate system-level building blocks in Simulink. Each radar building block consists of further sub-blocks to properly represent the functioning of the radar components in the model. The Simulink blocks representing the radar components were connected to perform simulations on the full radar model. Test probes were placed to assess the signal at the input and output of every building block in the simulation, both in the time and frequency domain. The data at the output of the last block of the receive chain was taken to the MATLAB workspace. The data processing chain was realised in MATLAB

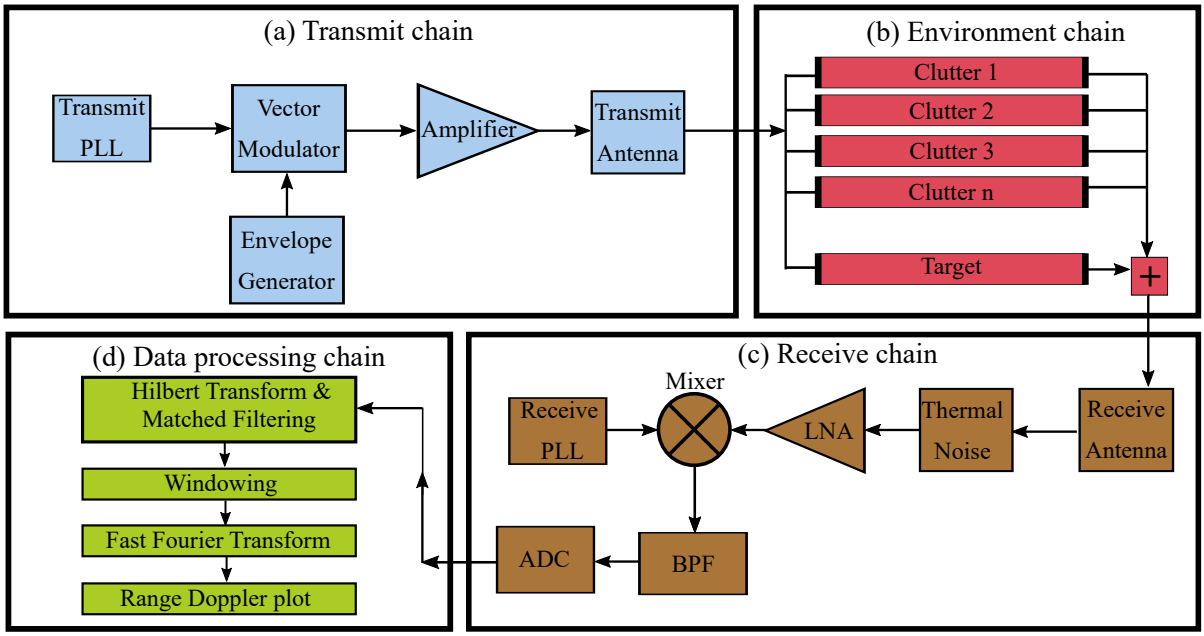

Figure 3.1: Schematic of the front end model of the whole radar model in the simulation. The front end consists of four main sections. The transmit chain transmits the amplified pulsed sinusoidal signal to the environment through the transmit antenna. The clutter and targets in the environment reflect the signal to the radar receive antenna. In the receive chain, the received signal undergoes stages of amplification and down-conversion to generate an IF signal. The IF signal gets converted to a baseband signal in the data processing chain. The baseband signal undergoes further data processing stages to enhance the target's signal-to-noise ratio.

using separate MATLAB codes.

The transmit chain of the front end of the radar model consisted of a transmit phase lock loop (PLL) for the generation of the transmit RF signal and an envelope generator to provide the amplitude envelope. The continuous RF signal produced at the output of the transmit PLL was converted to a pulsed, amplitude-modulated RF signal with the help of the vector modulator. The RF signal was then amplified using the amplifier and transmitted to the environment using the transmit antenna.

The environment consisted of targets and clutter models to reflect the transmitted RF signal towards the receive antenna. In the receive chain, the reflected signal from the

environment was collected by the receive antenna. The thermal noise block after the receive antenna added Gaussian thermal noise to the simulation. The LNA amplified the received signal at the output of the thermal noise block. The combination of the receive PLL block and the mixer block down-converted the received RF signal to a first intermediate frequency (IF1) signal. The IF1 signal was filtered using BPF to remove all the unwanted frequencies. The ADC placed at the output of the BPF down-converted the IF1 signal to a second intermediate frequency (IF2). Since the signal was already in the digital domain, the ADC was only used for frequency down-conversion.

A number of data processing methods were performed to the signal at the output of the ADC in the data processing chain. The data processing chain consisted of Hilbert transform and matched filtering, windowing, FFT, and range-Doppler plot generation. The matched filtering was used to improve the SNR in the presence of additive noise. In the radar domain, matched filtering is often referred to as pulse compression. The FFT was used to generate the range-Doppler plot from the time domain signal and to perform the pulse integration to improve the SNR. The spectral leakage due to the Fourier transform was reduced through windowing.

3.2 Transmit chain

The transmit chain of the simulated whole radar model consisted of components to perform signal generation, modulation, amplification and transmission. One of the significant aspects of the radar transmit chain is the generation of the RF transmit frequency. As discussed in the section 2.1.1.4, the transmit frequency is either directly generated or synthesised using the process of frequency up-conversion. The very early method for direct synthesis of the RF signal used magnetrons [95]. Recently, direct digital synthesis (DDS)

[96, 97] has been used to generate signals directly at the required RF frequency. The typical method to synthesise the RF signal using the frequency up-conversion consists of mixers. Another method for frequency up-conversion is using PLLs [98]. The RF signal was generated using a transmit PLL in the whole radar model. The Simulink simulation discussed in the chapter also consists of a general stand-alone PLL model to verify the PLL's working principle. In the whole radar model, due to modelling limitations in integrating the stand-alone model of the PLL, a simplified version of transmit PLL to generate the signal directly at the RF frequency was modelled.

Most of the radar signals undergo some form of waveform modulation. The waveform modulation can be of different types, including amplitude modulation, frequency modulation, and phase modulation, as discussed in section 2.1.1.3. The whole radar model consisted of an amplitude modulation to generate a pulsed radar signal. The amplitude envelope for the amplitude modulation in the whole radar model was generated by an envelope generator block, as shown in figure 3.1. The amplitude modulation is generally added to the RF signal with the help of mixers. The mixers are also used in radars for frequency up-conversion and frequency down-conversion. In the radar model, the vector modulator performs the function of the mixer. The vector modulator integrated the amplitude modulation into the RF signal. In most radars, the RF signal generated needs to be amplified to a high power before transmission to the environment. The power required for transmission and amplification depends on the radar application. The whole radar model simulated a simple amplifier design with a constant amplifier gain. The transmit antenna design can follow different architectures depending on the application. The transmit antenna was modelled as a single transmit antenna with a constant antenna gain in the whole radar model.

3.2.1 Transmit PLL

The transmit PLL generates the sinusoidal RF signal in the transmit chain of the radar model implemented in the simulation. This subsection discusses the fundamentals of PLL, the operation of a PLL in the simulation, and the transmit PLL design in the simulation.

3.2.1.1 Fundamentals of PLL

A PLL is an electronic circuit that uses a voltage or voltage-driven oscillator that continuously modifies its frequency to match an input signal. PLLs produce, stabilise, modulate, demodulate, filter, or recover a signal in' noisy' communication channels. The PLL plays an important aspect in most modern-day electronic devices, especially RF devices. In radars, the PLL is used to generate a stable RF signal at the radar transmit frequency using a highly stable reference oscillator.

The block diagram of a typical PLL is given in figure 3.2. The major components in a PLL include a reference oscillator, a voltage-controlled oscillator (VCO), a phase detector, a filter, and in some cases, a divider. The PLL works on the principle of tuning the phase and the frequency of the VCO with the help of the reference oscillator. A control input within the VCO adjusts the VCO frequency, and the phase detector compares the phase of the VCO to the reference oscillator. When the phase of the VCO is synchronised with the reference oscillator, the condition is known as phase-locked, and hence the name phase lock loop. The VCO can also be locked to a reference oscillator at a different reference frequency with the help of a divider placed in front of the phase detector, as shown in figure 3.2. The divider can also be placed after the reference oscillator when a fractional relation is required between the reference oscillator and the VCO frequencies.

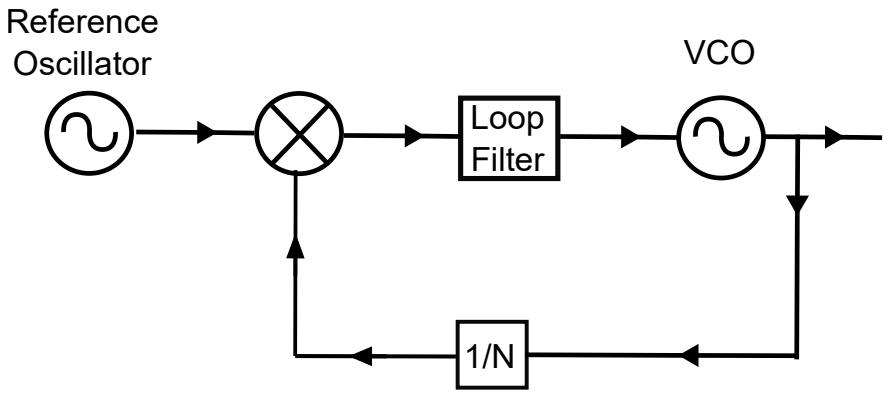

Figure 3.2: Schematic of a typical PLL consisting of a reference oscillator, phase detector, filter, VCO, and divider. The phase detector compares the output of the reference oscillator with the output of the VCO. The output of the phase detector is used to optimise the phase of the VCO until the VCO is locked with the reference oscillator. The divider is used to divide the VCO output frequency, and the filter is used to filter out the noise.

There are different kinds of phase detectors. The mixer phase detectors work on the principle of mixing the two input signals. The mixer performs the multiplication of two inputs, and one of the outputs of a mixer phase detector will be the sine of the phase difference between the two inputs. The mixer phase detector only detects the difference in the phase of the two inputs and is only valid for the same frequencies or frequencies very close to each other.

The phase frequency detector (PFD) is the most popular phase detector. The PFD can work even in cases where the frequency of the two input signals to the phase detectors is different. The PFD works on the principle of zero transitions of the input signals to track the difference in the phase and frequency. The outputs of the PFD consist of a UP signal and a DOWN signal. The UP and DOWN signal indicates the direction of the frequency change required to lock the PLL. Since a voltage signal controls the VCO, the UP and DOWN signals at the output of the PFD need to be converted into voltage signals. One of the standard conversion methods of the UP and DOWN signal is using the charge pumps [99]. The current sources in the charge pump can be controlled by the UP and DOWN outputs from the PFD. The charge pump current is sunk to the output when the UP signal is active,

and the charge pump current is drawn from the output when the DOWN signal is active. The capacitor at the output of the charge pump transfers the variation in current to the variation in voltage. The variation in voltage is fed to the control input of the VCO.

The filter in the PLL is primarily used to control the dynamics of the loop and hence is also known as a loop filter. The filter is also used to low-pass filter the noise and unwanted products at the output of the phase detector. The filter is placed before the VCO, and the output of the filter is fed to the control input of the VCO.

3.2.1.2 Operation of a PLL in simulation

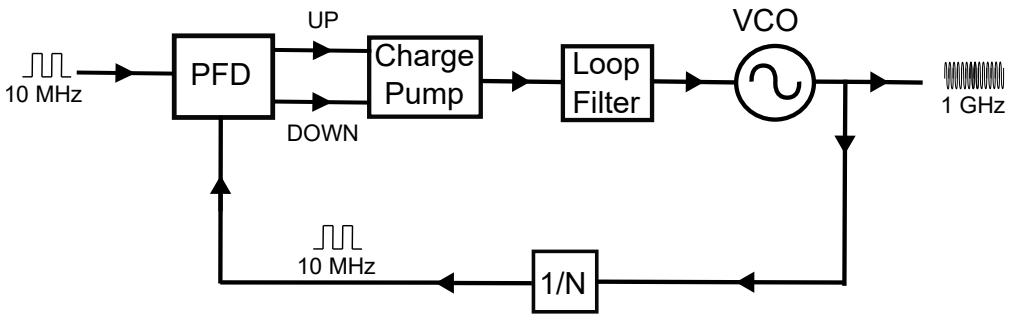

Figure 3.3: Illustration of a charge pump integer N PLL [100] to generate a phase-locked 1 GHz signal using a 10 MHz reference signal. The output of the VCO is divided by a factor of 100 and compared with the reference oscillator at the PFD. The UP and DOWN signals at the output of the PFD drive the charge pump. The charge pump output is transferred through a loop filter to the control input of the VCO. The PLL finally gets locked when both the reference signal and the divided signal are synchronised with each other.

A general example of a charge pump integer N PLL operation to generate an RF signal at 1 GHz using a 10 MHz stable reference oscillator is given in the figure 3.3 [100]. In the PLL simulation, the 1 GHz frequency was applied to PFD via a digital divider, reducing the frequency from 1 GHz to 10 MHz. The reference signal and the divider signal were compared in the PFD, and the PFD generated an error signal depending on the phase difference between the two input signals. The error signal drove the charge pump, and the charge pump output was provided to the control input of the VCO. The PLL output signal

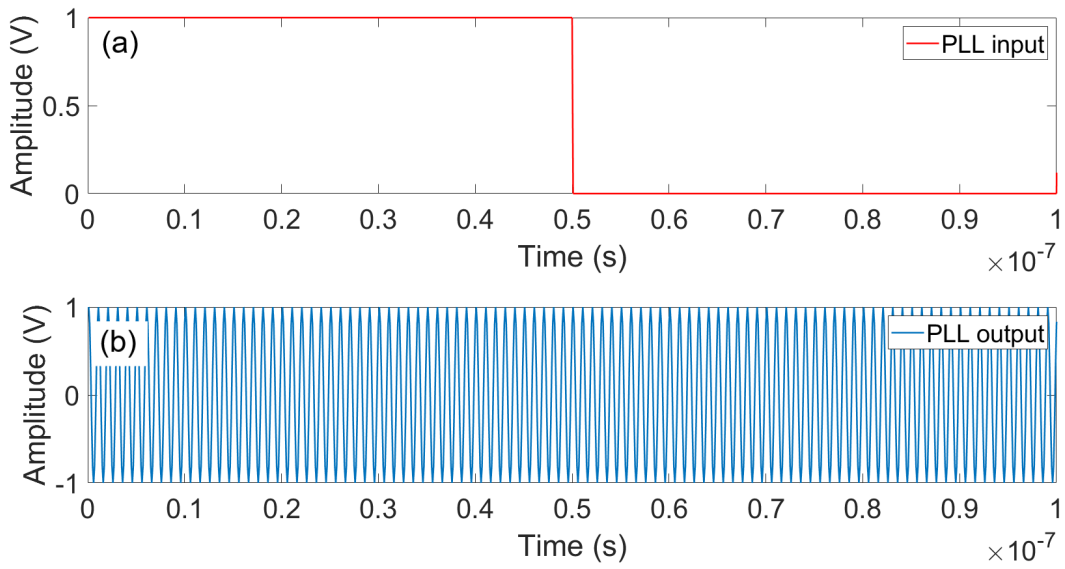

Figure 3.4: Time domain representation of (a) 10 MHz pulsed signal at the input of the PLL, (b) 1 GHz phase-locked VCO signal at the output of the PLL.

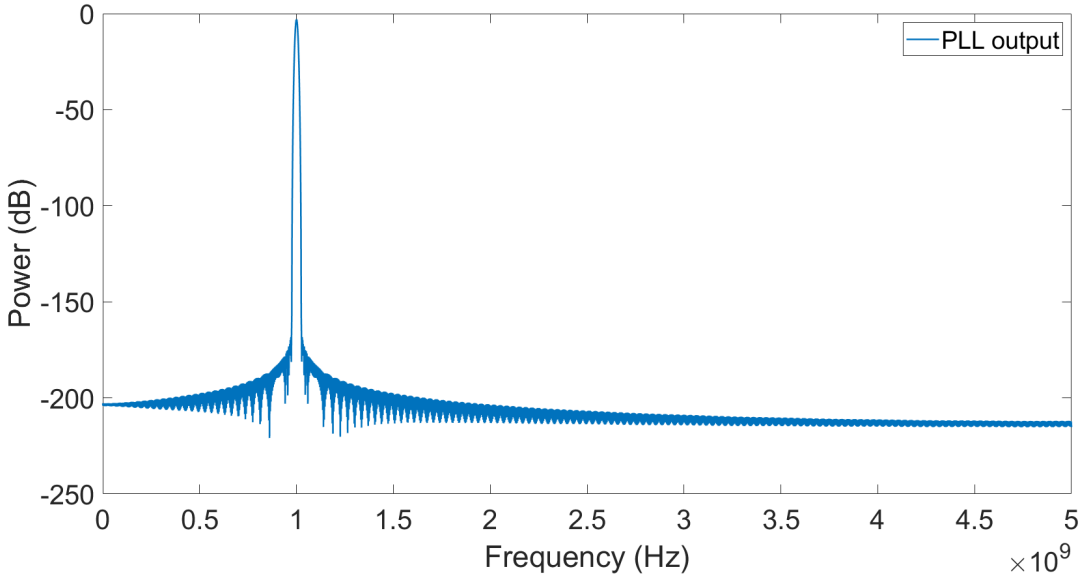

Figure 3.5: Power spectrum of the 1 GHz phase-locked VCO signal at the output of the PLL.

at 1 GHz finally gets locked to the 10 MHz reference signal when both the reference signal and the divided signal are phase locked. The 10 MHz pulsed reference signal to the input of the PLL and the 1 GHz phase-locked sinusoidal signal at the output of the PLL are given

in figure 3.4. The spectrum of the phase-locked VCO signal at the output of the PLL given in figure 3.5 shows a peak at 1 GHz, confirming the operation of the PLL in the simulation platform.

3.2.1.3 Transmit PLL in simulation

The ideal case scenario is to integrate a fully functional PLL model as described in the section 3.2.1.2 within the whole radar model simulation. Due to design and timing considerations, it was not possible to integrate the fully functional PLL into the radar model. As an alternate approach, the transmit PLL simulated in the model was based on the RF blockset in the Simulink and was modelled as a direct digital synthesiser to generate the signal directly at the RF frequency. As a result, the transmit frequency at L-band is directly generated in the simulation, and there is no stage of frequency upconversion or a PLL involved. The transmit PLL also has the option to add phase noise to the generated signal. Phase noise is very crucial in the characterisation and the performance of the radar, and the effects of phase noise in the radar system are discussed in detail in chapter 5. The transmit PLL can provide amplitude and frequency to any user-specified value. The block also has the option to provide the amplitude to both the in-phase and quadrature components of the signal. Apart from generating signals with a specific amplitude, the signals can also be specified in terms of current and power. The output frequency of the transmit PLL was set to the transmit frequency of the L-band staring radar. The amplitude of the signal generated was set to 1 V. The simplified equation of the mathematical model of the signal at the output of the transmit PLL is given by,

$$S_{PLL}(t) = A_{PLL}\cos[2\pi f_T t + \theta], \tag{3.1}$$

where $S_{PLL}(t)$ represents the sinusoidal signal at the output of the transmit PLL, A_{PLL} and θ represent the sinusoidal signal's amplitude and phase, respectively, and f_T represents the transmit frequency.

3.2.2 Envelope generator and vector modulator

Signal modulation is one of the important aspects of the transmit chain of the radar. Amplitude and frequency modulation are the two most common signal modulations used in radars [86]. The amplitude modulation provides an amplitude envelope over the generated RF signal, and the envelope can be of different shapes based on the radar requirements. The most common amplitude modulations are rectangular envelopes. In linear frequency modulation, the transmit signal frequency is modulated in a linear fashion. Linear frequency modulation is used to achieve high range resolution and large detection range simultaneously using the increased bandwidth of the transmit signal. The enveloper generator is one of the methods to generate the modulation required for the radar transmit signal. The vector modulator is fundamentally a mixer to add the baseband modulation to the RF signal. The vector modulator architecture is similar to a general mixer architecture.

3.2.2.1 Envelope generator in simulation

In the whole radar model, the envelope generator was used to provide the required amplitude envelope for the signal generated by the transmit PLL. The envelope generator can generate any user-defined amplitude envelope. The envelope generator also has the potential to include further sub-blocks to enable phase modulation and frequency modulation. In the simulation, the envelope generator generated a rectangular-shaped envelope with a pulse width of about 1 µs and a PRI of about 136 µs. The envelope generator was realised as a block that can provide amplitude values at a user-specified sampling rate. The amplitude

values were loaded into MATLAB as mat files and were read by Simulink at the specified sampling rate. The amplitude envelope at the output of the envelope generator is given in figure 3.6a.

3.2.2.2 Vector modulator in simulation

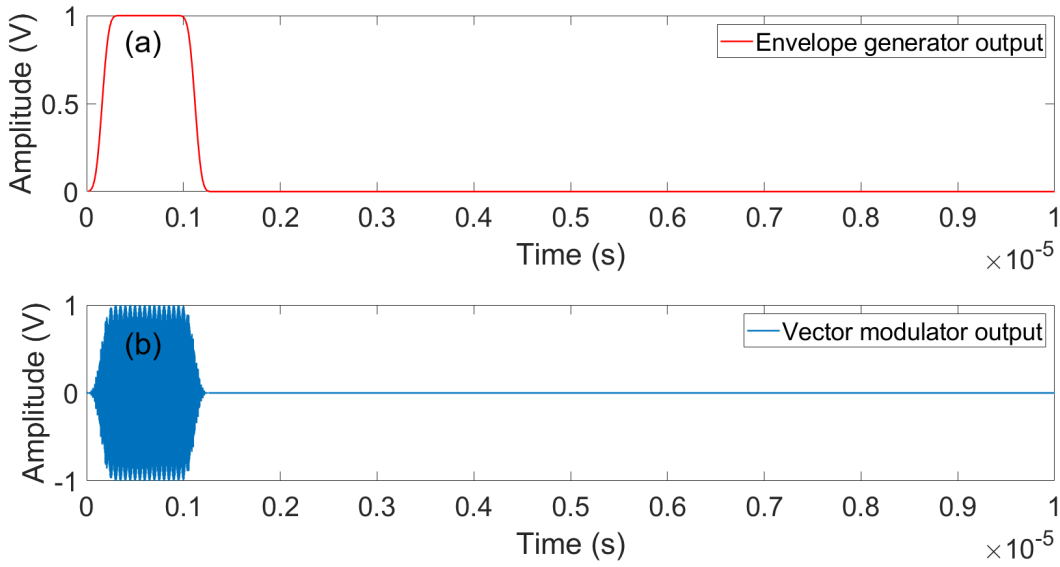

Figure 3.6: Time domain representation of the signals at the output of different blocks in the transmit chain. The representation only shows a partial section (10 µs) from a full PRI. (a) Envelope generator output showing an amplitude envelope of around 1 µs, (b) Vector modulator output showing the continuous sinusoidal signal inside the amplitude envelope. The transmit frequency at the L-band makes it difficult to resolve the sinusoidal signal in the representation. The appearance of the higher frequency sinusoidal shape within the envelope for the signal at the output of the vector modulator output is the artefact of the sampling rate of the envelope generator.

In the whole radar model, the vector modulator mixes the continuous sinusoidal signal at the output of the transmit PLL with the amplitude envelope at the output of the envelope generator. The vector modulator was realised in the simulation using an RF blockset mixer. The mathematical model of the signal at the output of the vector modulator is given by [101, 102],

$$S_V(t) = A_V \cos\left[2\pi f_T t + \theta\right], \tag{3.2}$$

where $S_V(t)$ represents the signal at the output of the vector modulator, A_V, f_T, and θ represents the amplitude, frequency, and phase of signal respectively. Even though the signal at the output of the vector modulator was a pulsed signal, for simplicity, the time dependency of the pulse is not explicitly mentioned in the equation 3.2. Hence the equation 3.2 is a simplified mathematical signal model. The pulsed RF signal at the output of the vector modulator is shown in figure 3.6b. Figure 3.6b clearly shows the amplitude envelope over the sinusoidal RF signal. The particular shape of the vector modulator output is the artefact of the envelope generator's sampling rate.

3.2.3 Amplifier

An RF amplifier is an electronic amplifier used in most communication systems to amplify the input signal to the required output signal. In radars, the RF amplifiers are used to convert the low-power RF signal generated by the transmitters to high power RF transmit signal. The RF amplifiers are generally located before the radar transmit antenna and drive the transmit antenna. The design parameters of an RF amplifier include gain, power output, bandwidth, input and output impedance matching, and linearity [103].

The gain of the RF amplifier is defined as the ratio of the output power to the input signal power. The bandwidth defines the operational signal bandwidth of the amplifier and, ideally, would need different amplifiers depending on the signal frequency. Impedance is defined as a measure of opposition to the electrical flow. Impedance is a complex-valued quantity with resistance as the real part and reactance as the imaginary part. The impedance matching is equalising the input and output impedance to maximise the signal power transfer by minimising the signal reflections. The linearity is described as a circuit's behaviour; the output signal strength variation is directly proportional to the input signal strength variation. The output-to-input signal power ratio remains the same for a linear amplifier, independent

of the input signal power.

3.2.3.1 Amplifier in simulation

In the whole radar model, a simplified signal amplifier was used to amplify the input signal to any user-defined value. The amplifier in the simulation has the option to perform both linear and non-linear amplification. The amplifier in the simulation was set to linear amplification. The amplification factor in dB can also be provided to the amplifier. From the radar power budget, the signal power's expected value at the amplifier's output is 33 dB. The power spectrum outputs the RMS value of signals. For an ideal rectangular pulse with a width of 1 µs and a PRI of 136 µs, the RMS peak will be reduced by a factor of 21.3 dB, resulting in a power spectrum peaked at 11.7 dB (instead of 33 dB). Since the amplitude envelope in the simulation is not a perfect rectangle, the peak at the spectrum will be reduced by an additional 3.8 dB, resulting in a total reduction of 25.1 dB. The power spectrum of the signal at the output of the amplifier is given in figure 3.7. In figure 3.7, we can see that the signal's peak power at the amplifier's output is 7.9 dB, equivalent to 33 dB of transmit power.

3.2.4 Transmit antenna

Antennas are widely used in all wireless systems. The behaviour of an antenna is dependent on the components within the antenna, and the antenna design is dependent on the application. In radars, transmit antenna is used to broadcast the RF transmit signal to the environment. Transmit antenna is a heavily studied field in radars [104–106]. The important parameters of an antenna are the radiation pattern, antenna gain, and directivity [103].

The radiation pattern of an antenna is a description of the angular dependence of its emissions, which are a result of its three-dimensional geometry. In the three-dimensional coordinate system, the horizontal plane (XY) is defined as the azimuth plane, and the vertical plane (YZ) is the elevation plane. An azimuth angle is defined as the horizontal axis angle from the antenna boresight direction. An elevation angle is defined as the angle above the horizon in the vertical direction. Based on the radiation pattern, the antennas can be divided into an isotropic and a directional antenna. An isotropic antenna is a theoretical antenna pattern where radiation power is equal in all directions of azimuth and elevation. In a directional antenna, the energy is dominated in one or more directions. Antenna gain is defined as the ratio of power transmitted in the main direction of a directional antenna to the power in an isotropic antenna. The main direction of a directional antenna is called antenna boresight. The directivity of an antenna is defined as the maximum signal power radiated in a given direction divided by the average power in all directions.

3.2.4.1 Transmit antenna in simulation

The transmit antenna was designed as a simplified antenna with a constant antenna gain in the whole radar model. There are significant differences between the antenna in simulation and the antenna in real radar. The simulation only corresponds to a single element of the receive antenna, whereas the real radar consists of 64 arrays of antenna elements. The simulator modelled an isotropic antenna and only included the gain parameter. There are antenna designs in Simulink that can include the parameters like directivity. The constraint in the total simulation time for the whole radar simulation was considered while simulating the simplified antenna model. Further modifications can be incorporated into the antenna design depending on the application. The antenna gain in the simulation was realised using an amplifier as described in the section 3.2.3.1. The simplified mathematical model of the

transmitted signal is given by,

$$S_T(t) = A_T \cos\left[2\pi f_T t + \theta\right], \tag{3.3}$$

where $S_T(t)$ represents the transmitted signal, A_T represents the amplitude of the transmitted signal. The power spectrum of the signal at the output of the transmit antenna is given in figure 3.7. The transmit antenna is expected to amplify the signal by 12.5 dB at transmission. The value of antenna gain was selected based on the system parameters of the L-band staring radar. From figure 3.7, we can see the signal at the output of the transmit antenna peaked at 20.4 dB, equivalent to a signal power of 45.5 at the output of the transmit antenna. The transmit antenna gain of 12.5 dB is visible in figure 3.7. In the simulation, the output of the transmit antenna was connected to the blocks in the environment.

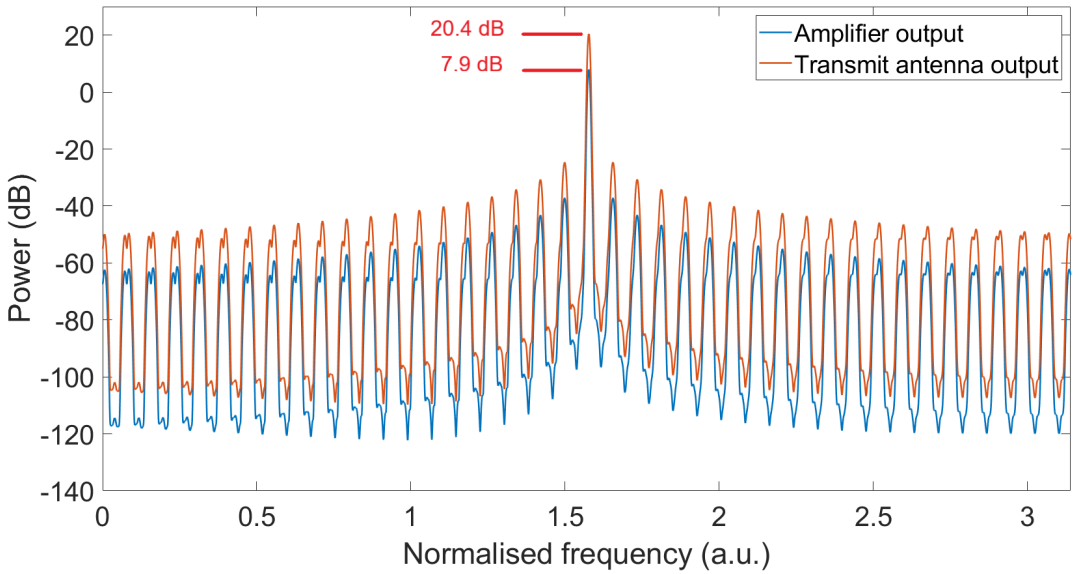

Figure 3.7: Power spectrum of the signal at the output of the amplifier and the transmit antenna. The power spectrum at the output of the amplifier is peaked at 7.9 dB, equivalent to a signal power of 33 dB. The power spectrum at the output of the transmit antenna is peaked at 20.4 dB, equivalent to a signal power of 45.5 dB. The transmit antenna gain is equivalent to 12.5 dB. The sidelobes in the power spectrum are the artefact of the sampling rate of the envelope generator.

3.3 Environment

The environment of a radar consists of both targets and clutter. The definition of targets and clutter depends on the radar application. For the case under consideration discussed in this thesis, the targets include drones, aircraft, ships, cars, and birds. All the moving targets have a Doppler frequency associated with the target, and the Doppler frequency is used to measure the velocity of the target. For the radar discussed in the thesis, the clutter includes stationary objects and can consist of buildings, trees, land, sea and other geographical features in the field of view. The weather is also classified as clutter. The electromagnetic signal interacts with the atmosphere, the clutter and targets, and the different kinds of interaction are discussed in section 2.1.2. The interaction of the electromagnetic signal with the environment is accommodated in the radar range equation as discussed in section 2.2.1.

3.3.1 Target and clutter in simulation

In the whole radar model, a simple representation of the magnitude response of both the targets and the clutter was simulated. Each of the sub-blocks within the environment, as shown in figure 3.1, represents the magnitude response of different objects in the environment, and the objects can be either targets or clutter. The targets and clutter are realised as point scatterers in the whole radar model. The output of the transmit antenna block was connected to the input of the magnitude response block. Each magnitude response block was designed based on the radar range equation. The range, velocity and the RCS of each object can be defined in the magnitude response block. The environment can ideally represent any number of objects with varying ranges, velocities and RCS values as point scatterers. Since the antenna's directivity is not included in the simulation, the position of

objects corresponds to ranges in the radar boresight. The simulation could include additional algorithms to place objects at a specific angle in the azimuth and elevation. The output of the magnitude response blocks was connected to the receive chain through an interface. The interface combined the reflected signal from all the different objects in the environment and was directed to the receive chain. The atmospheric loss is currently kept at unity in the simulation. Both targets and clutter are modelled as simple point scatterers, with the targets modelled at specific range bins and clutter distributed in every range bin. The environment modelling presented in the thesis is very basic modelling. There are many parameters that need to be included for a comprehensive radar environment modelling, including clutter RCS variation [107, 108] and target RCS variation [109, 110].

3.4 Receive chain

The receive chain of the radar model consists of components to perform signal reception, signal amplification, signal down-conversion and analogue to digital conversion. The receive antenna receives the reflected signal from the environment. The receive antenna also provides amplification to the signal. Generally, the radar receiver consists of thermal noise due to the random thermal fluctuation of electrons as described in the section 2.3.1.1. In the whole radar model, a separate block was used to generate the thermal noise in the receiver chain of the radar system. The thermal noise block was placed after the receive antenna, as shown in figure 3.1.

One of the crucial blocks in the receive chain of the whole radar model was the receive PLL. The frequency of the signal at the output of the receive PLL was different from the frequency of the signal at the output of the transmit PLL. The frequency offset between the transmit PLL and the receive PLL was equivalent to the IF. The combination of the

mixer and BPF performed the down-conversion of the received signal to IF. The output of the receive PLL was mixed with the received signal. In the whole radar model, since both the signals were digital signals, a signal multiplier was used to mix the received signal. The ADC is another crucial block in the receive chain of a radar system. The ADC performs the fundamental operation of converting an analogue signal to a digital signal. Whenever the sampling rate of the ADC does not follow the Nyquist criteria, aliasing happens, and the input signal will be represented as a down-converted signal at the output of the ADC. According to the Nyquist criteria, to reliably reproduce a signal, the sampling frequency should be at least twice the maximum frequency of the signal. The Nyquist frequency is defined as twice the highest frequency of interest. When frequencies above half the Nyquist frequency are sampled, the frequencies are incorrectly detected as lower frequencies, the process known as aliasing [111]. In the whole radar model, the signals were already in the digital domain, and ADC performed a second round of down-conversion through aliasing.

3.4.1 Receive antenna and thermal noise

The receive antenna is present in most wireless communication devices, including radars. Different kinds of radar receive antenna configurations depend on the application, including a single receive antenna or an array of receive antenna elements. These designs apply to both the transmit antenna and the receive antenna. In radar receiver, the antenna array consists of a collection of identical and uniformly spaced antenna elements that operate as a single unit [111]. The signals received in the individual array elements are combined with the required phase relationship to enhance signals from the desired direction and to cancel the signals from the undesired direction, thereby improving the SNR for target detection [112].

Thermal noise is an inevitable factor in any electronic device. Thermal noise defines

the lower bound for the target detection, and the radar range-Doppler plots are always limited by the thermal noise floor. As discussed in section 2.3.1.1, the thermal noise depends on the bandwidth and the temperature of the radar receive chain. The thermal noise can be lowered by reducing the bandwidth and the temperature of the radar receive chain.

3.4.1.1 Receive antenna in simulation

In the whole radar model, the receive antenna was designed as a single, simplified antenna with a constant antenna gain. The L-band staring radar used for comparison and validation consists of a two-dimensional array of 64 receive antenna elements. Considering the time constraint on the simulation of the whole radar model, the simulation currently has a single receive antenna element. Adding more antenna elements adds more receive chain components, and the model can accommodate more antenna elements at the cost of simulation time. The output of the magnitude response blocks in the environment was connected to the input of the receive antenna through the interface. The receive antenna gain in the simulation was realised using an amplifier similar to the one described in section 3.2.3.1.

Consider a radar that transmits a series of M pulses with $0 \leq m \leq M-1$, separated by a PRI of T. For a target with an initial range of R_o and a velocity of ν, the range of the target for the m^{th} transmitted pulse is $R_o - \nu mT$. For the m^{th} transmitted pulse, the signal that reaches the receiver antenna will have a time delay equivalent to $\frac{2}{c}(R - \nu mT)$. The mathematical model for the delayed received signal is given by,

$$\begin{aligned} S_R(t) &= S_T(t - \frac{2}{c}(R - \nu mT)), \\ &= A_R \cos\left[2\pi f_T t + 2\pi(\frac{2\nu}{\lambda})mT + (\theta - \frac{4\pi R_o}{\lambda})\right], \\ &= A_R \cos\left[2\pi f_T t + 2\pi f_d mT + \theta'\right], \end{aligned} \tag{3.4}$$

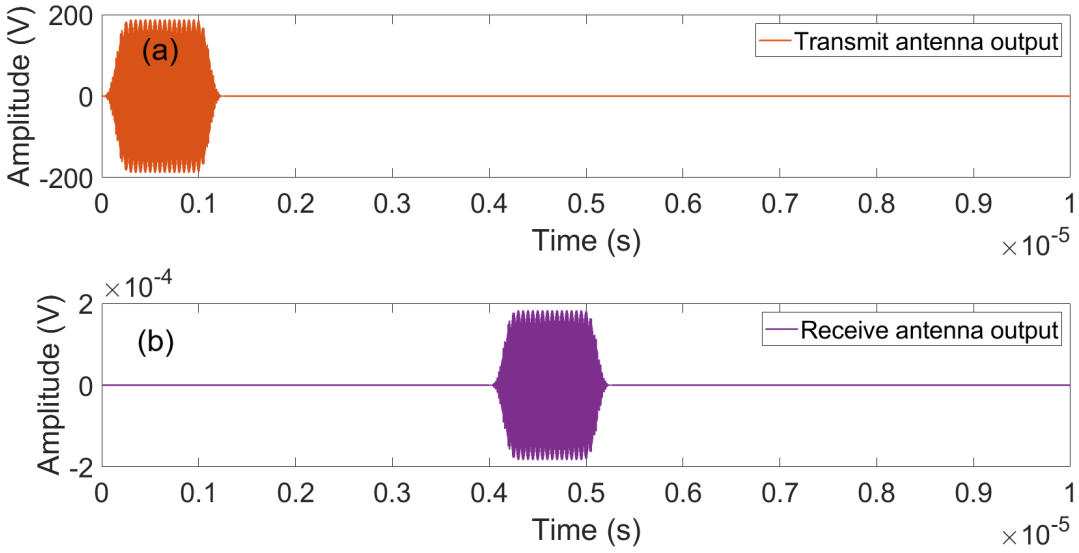

Figure 3.8: Time domain representation of the signals at the antenna outputs showing a time delay of 4 µs equivalent to a range of 600 m. The representation only shows a partial section (10 µs) from a full PRI. (a) The signal at the output of the transmit antenna, and (b) the signal at the output of the receive antenna.

where $\frac{2\nu}{\lambda} = f_d$ is the Doppler frequency of the target moving towards the radar and $\theta - \frac{4\pi R_o}{\lambda} = \theta'$ is the phase of the received signal. A_R represents the amplitude of the received signal and follows the radar range equation.

Throughout the sections 3.4 and 3.5 in the chapter, a drone target at a range of 600 m and a specific value of RCS is used. For the drone target at 600 m, the received signal will be delayed by 4 µs compared to the transmitted signal. The time domain representation of the signal at the output of the transmit antenna and the signal at the output of the receive antenna is given in figure 3.8. Figure 3.8 clearly shows a delay of 4 µs between the transmitted and received signal as expected. The radar range equation, equation 2.1, provides the expected value of the received signal power. For the test drone target at 600 m and the specific RCS value provided, the signal power at the output of the receive antenna is expected at -74.4 dB. The power spectrum of the signal at the output of the receive antenna is given in figure 3.10. Figure 3.10 shows the output of the receive antenna peaked at -99.6

dB. Since the peaks in the power spectrum are reduced by a factor of 25.1 dB due to the RMS value, the received signal power is -74.5 dB, very close to the expected value of -74.4 dB.

3.4.1.2 Thermal noise in simulation

In the simulation, the thermal noise was added using a separate block. The thermal noise block in the simulation can provide any value to the noise temperature. The noise bandwidth in the simulation was equivalent to the sampling rate of the simulation. The sampling rate of the simulation was set to 5 GHz, greater than twice the value of any frequency used in the simulation, satisfying the Nyquist criteria. For a noise bandwidth of 5 GHz and noise temperature equivalent to room temperature (290 K), the expected thermal noise power using the equation 2.4 will be -107 dBW. Figure 3.9 shows the histogram of the thermal noise power values generated by the thermal noise block. The Gaussian distribution of the thermal noise power values peaked at -107 dBW can be seen in the histogram in figure 3.9.

The SNR is an important parameter that defines the performance of the radar. The SNR of the received signal is given by the equation 2.5. The SNR of the received signal with an atmospheric loss factor of unity is given by,

$$SNR_R = \frac{P_T G_T G_R \lambda^2 \sigma}{4\pi^3 R^4 k T B}. \tag{3.5}$$

The power spectrum of the signal at the output of the thermal noise block is compared with the power spectrum of the signal at the output of the receive antenna in figure 3.10. In figure 3.10, we can see the thermal noise at all the frequencies. The resolution bandwidth (RBW) of the power spectrum was 5 MHz, and the noise bandwidth of the simulation was 5 GHz. Since the RBW of the power spectrum is 5 MHz, all the out-of-band noise outside 5 MHz

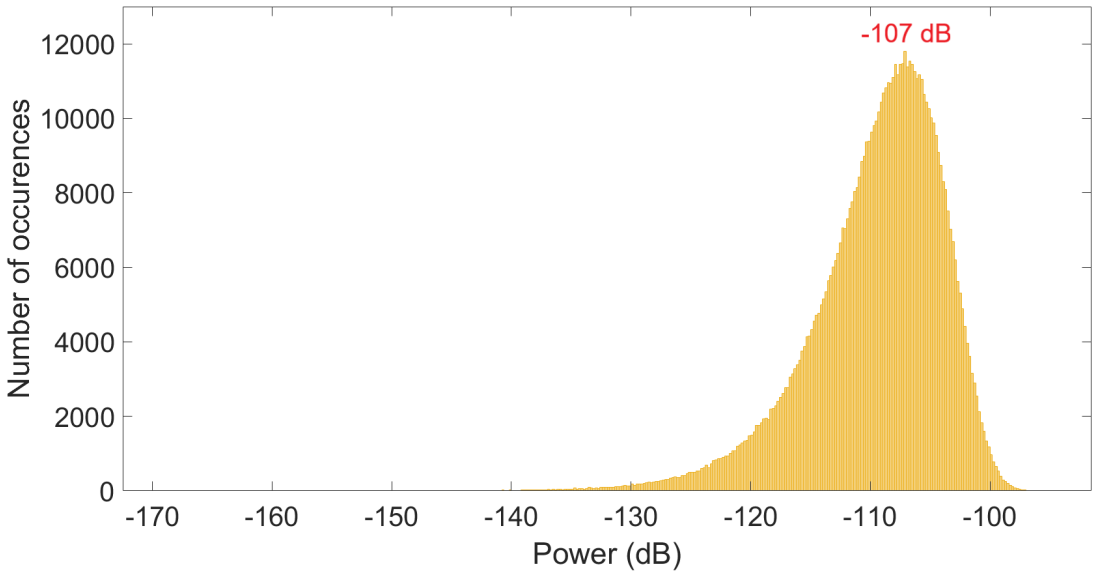

Figure 3.9: The histogram of the thermal noise at the output of the thermal noise block in the simulation. The histogram shows Gaussian noise distribution peaked at -107 dBW for the bandwidth and temperature of 5 GHz and 290 K, respectively.

will be filtered out by the spectrum analyser, resulting in an effective noise floor of 5 MHz at the spectrum analyser output. The 5 MHz of noise bandwidth equates to a thermal noise floor of -137 dB, instead of a thermal noise floor of -107 dB (equivalent to 5 GHz). Hence the thermal noise floor in figure 3.10 at -137 dB, 30 dB lower than the thermal noise power of -107 dB.

3.4.2 LNA

An LNA is an essential component in the receive chain of most communication systems, especially radars. The LNA is an electronic amplifier capable of amplifying weak signals without significant degradation of the SNR. In radars, the LNA is generally located after the receive antenna to amplify the weak received signal and to provide power levels appropriate for the analogue to digital conversion or further processing in the analogue domain. The performance of an LNA can be measured using different parameters, including

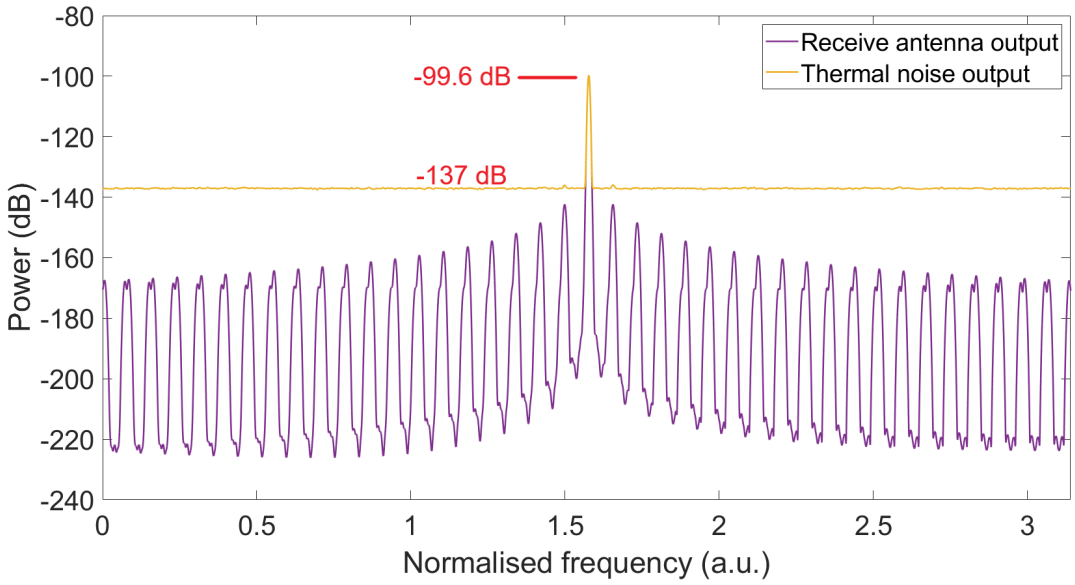

Figure 3.10: Power spectrum of the signal at the output of the receive antenna and thermal noise block. The power spectrum at the output of the receive antenna is peaked at -99.6 dB, equivalent to a received signal power of -74.5 dB. The power spectrum at the output of the thermal noise block shows the uniform thermal noise floor at -137 dB. Since the spectrum has an RBW of 5 MHz, the -137 dB is equivalent to the expected thermal noise power of -107 dB.

noise figure, gain, and dynamic range. The gain of an LNA is defined as the amplification factor of the LNA. The LNA gain is specified in dB. The LNA's noise figure (NF) is defined as the measure of degradation of the SNR of the received signal. For example, if an LNA has an SNR degradation of 3 dB at the output of the LNA compared to the input of the LNA, the NF of the LNA will be 3 dB. The radar engineers target to manufacture LNAs with NF as low as possible to reduce the degradation of the SNR due to LNA.

3.4.2.1 LNA in simulation

In the whole radar model, the LNA was realised using an amplifier with the option to specify the NF. The design of the LNA was based on the amplifier as discussed in the section 3.2.3.1. The LNA can provide any user-defined value of amplification. Along with the LNA

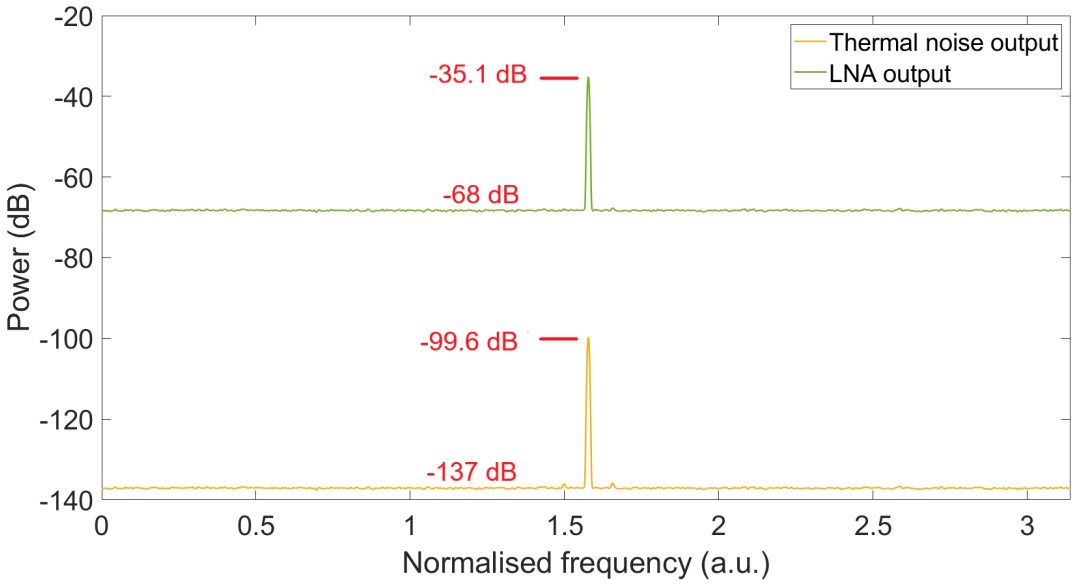

Figure 3.11: Power spectrum at the output of the thermal noise block and the LNA. The power spectrum at the output of the LNA is amplified to -35.1 dB, equivalent to a peak power of -10 dB. The noise floor is amplified to -68 dB, equivalent to the noise power of -38 dB. The SNR at the output of the LNA is less than the SNR at the output of the thermal noise block by a factor of 4.5 dB (equivalent to the LNA NF).

gain, the LNA block can also specify any value of the NF. The mathematical model for the received signal at the output of LNA (S_{LNA}) is given by,

$$S_{LNA}(t) = A_{LNA} \cos\left[2\pi f_T t + 2\pi f_d m T + \theta'\right], \tag{3.6}$$

where A_{LNA} represents the amplitude of the received signal after the LNA. The SNR at the output of the LNA (SNR_{LNA}) is given by,

$$SNR_{LNA} = SNR_R - NF, \tag{3.7}$$

where NF is the noise figure of the LNA. The power spectrum of the signal at the output of the LNA is compared with the signal at the output of the thermal noise block in figure 3.11. We can see the signal power and noise floor amplified by a factor equivalent to the LNA amplification factor. In figure 3.11, we can also see the SNR at the output of the thermal

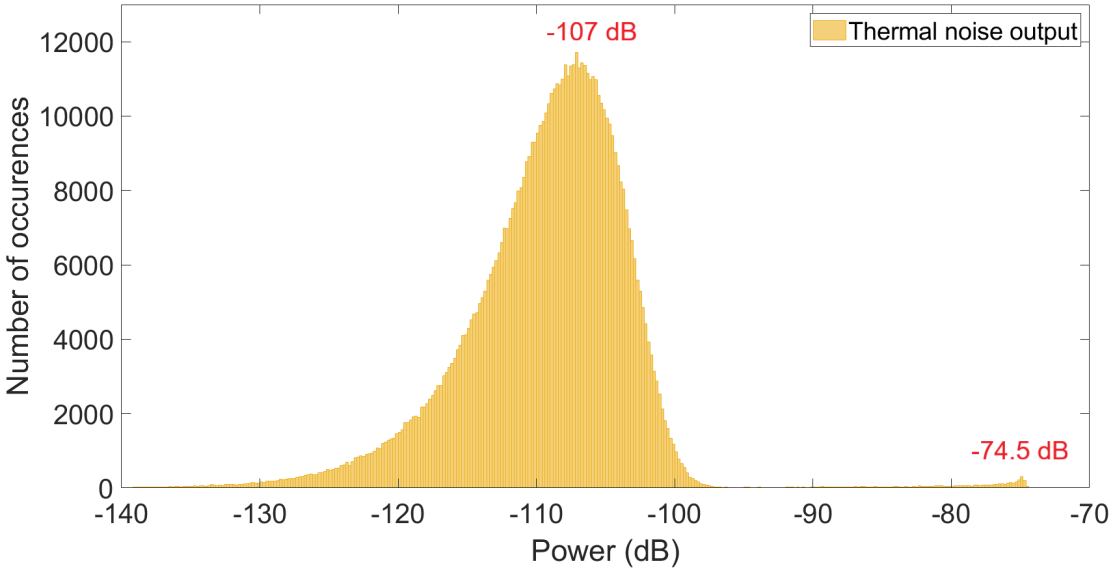

(a) Histogram at the output of the thermal noise block showing the signal power and noise power at -74.5 dBW and -107 dBW, respectively.

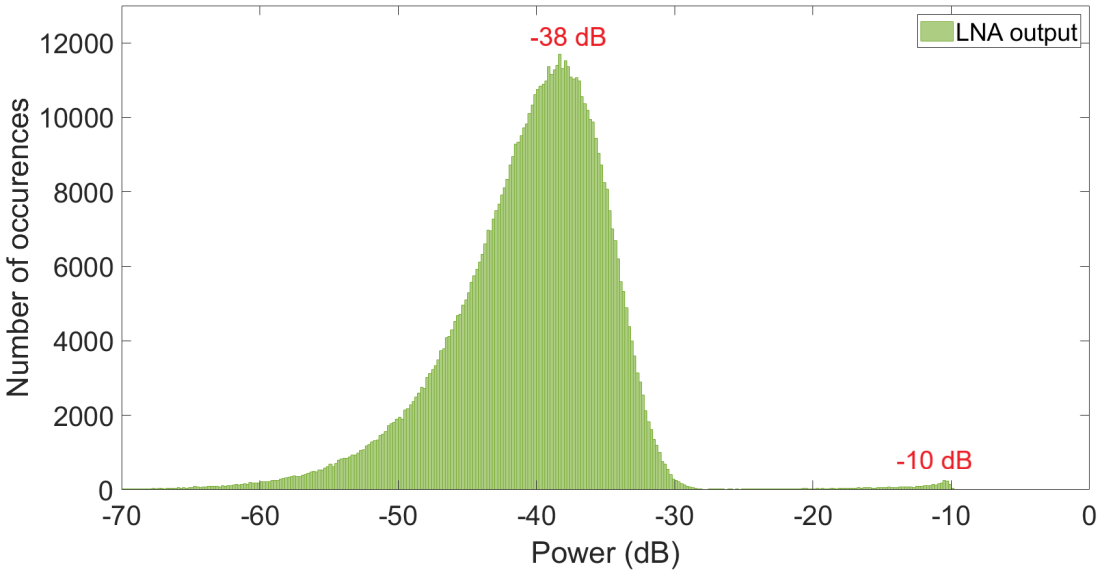

(b) Histogram at the output of the LNA showing the signal power and noise power at -10 dBW and -38 dBW, respectively.

Figure 3.12: The histogram at the output of the thermal noise block and the LNA showing the peak signal and noise power values.

noise block and LNA at 37.4 dB and 32.9 dB, respectively. The SNR at the output of the thermal noise block is reduced by a factor of 4.5 dB, equivalent to the LNA NF, compared to the SNR at the output of the thermal noise block.

The signal and noise powers at the output of the thermal noise block and the LNA are also compared by plotting the histograms in figure 3.12. In figure 3.12, the broad peak corresponds to the noise power, and the small peak towards the right end of the histogram corresponds to the peak signal power. Figure 3.12a shows the signal power and noise power after the thermal noise block peaked at -74.5 dBW and -107 dBW, respectively. Figure 3.12b shows the signal power and noise power after the LNA peaked at -10 dBW and -38 dBW, respectively. Figure 3.12 also shows the SNR at the output of the LNA reduced by 4.5 dB compared to the output of the thermal noise block.

3.4.3 Receiver PLL and mixer

One of the crucial steps in any of the receive chains of a radar system is to down-convert the received RF signal. The down-conversion to baseband can either be in a single step or through multiple steps as discussed in 2.1.3.1. In most cases, the received RF signal is down-converted through multiple stages, with each stage having a corresponding IF. The down-conversion to IF is generally carried out by mixing the received signal with either the LO signal in the transmit chain or a signal derived from the LO signal and hence preserves the coherency.

The mixers are generally used in a vast number of RF applications. An RF mixer is a three-port device used to up-convert or down-convert the signal frequency. The mixer has two inputs, an RF and a LO input. The output of a mixer will have two major frequencies, the sum of the two input frequencies and the difference between the two input frequencies.

An ideal mixer changes an input signal's frequency while preserving the input signal's phase. The mixers are used in the radar receive chain to down-convert the RF signal to a convenient frequency to perform further processing steps. Along with the sum and difference frequency, in reality, the mixer outputs a family of frequencies, including mRF $\pm$ nLO, where m and n are integers. Mixers also have leakages between all the ports that need to be accounted for. There are different kinds of mixers, including active mixers [113, 114], and image reject mixers [115, 116]. A typical mixer is illustrated in figure 3.13.

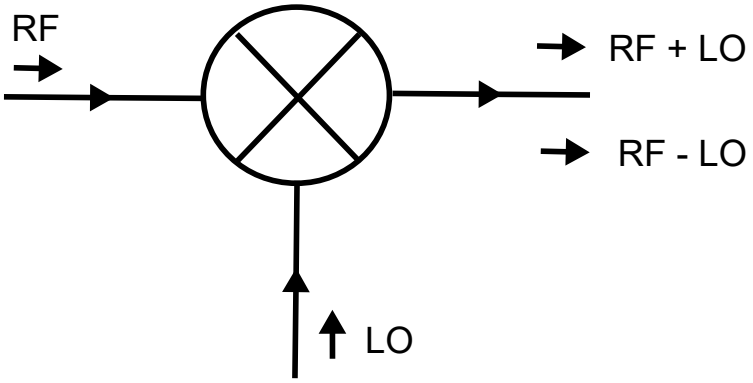

Figure 3.13: Schematic of a typical mixer consisting of RF and LO inputs and an output. The output consists of two major frequencies, the sum of the two input frequencies and the difference between the two input frequencies.

The two important parameters that affect the SNR of the mixer output are the mixer conversion loss and the NF of the mixer. The mixer conversion loss is defined as the ratio between the input RF power and the output IF power. The NF of a mixer is defined as the ratio between the input SNR and the output SNR. For an ideal mixer with a LO input amplitude of unity and an RF input amplitude of A, the amplitude of each of the outputs will be equivalent to $A/2$. Since the power is proportional to the square of the amplitude, the power of each of the output signals of the mixer will be 1/4 times the input power. Hence, the conversion loss of an ideal mixer will be 6 dB [117, 118]. The NF of the mixer (NF_{MXR}) is related to the image frequency. Along with the desired frequency band, there is also an undesired frequency band known as the image frequency for a mixer that down-converts the RF to IF using the LO. If the noise is present in both the desired and image frequency

band, the down-conversion folds back the noise in the image band on top of the noise in the desirable band, resulting in an NF of 3 dB.

3.4.3.1 Receiver PLL in simulation

In the whole radar model, the receive PLL was designed similarly to the transmit PLL. The receive PLL was designed as a direct digital synthesiser to output any user-defined frequency. The frequency at the output of the mixer was equivalent to the sum of the transmit frequency and the IF. The coherency between the receive PLL and the transmit PLL was achieved within the Simulink simulation. Both the transmit PLL and the receive PLL were run simultaneously in the simulation and were always turned on, making the phase relationship between the transmit PLL and the receive PLL coherent.

3.4.3.2 Mixer in simulation

In the whole radar model, the RF input of the mixer was connected to the output of the LNA, and the LO input of the mixer was connected to the output of the receive PLL. The difference frequency at the output of the mixer was equivalent to the IF1. The mixer in the simulation was realised using a product block to mix both the input signals.

The amplitude at the output of the receive PLL was kept at unity; hence, the mixer conversion loss followed the case of an ideal mixer and was obtained at 6 dB. The conversion loss affects both the signal and the noise equally, and the signal power and the noise power at the output of the mixer were 6 dB less than the output of the LNA. The effective SNR gain due to the conversion loss in the mixer was zero. In the simulation, the real-valued received signal was accompanied by the complex-valued thermal noise. Hence, the down-conversion folded the thermal noise present in the image band over the thermal noise present in the

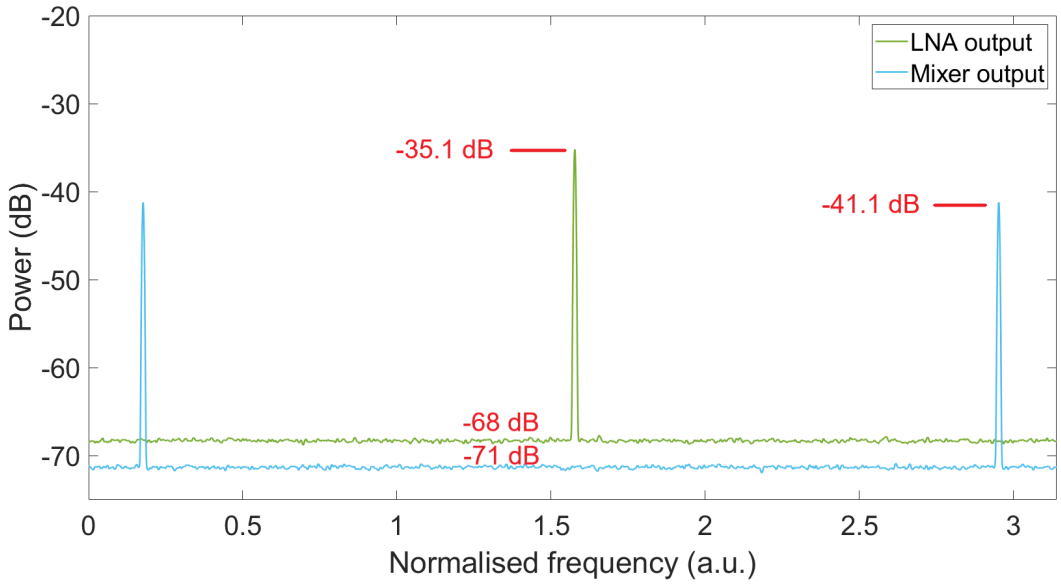

Figure 3.14: Power spectrum of the signal at the output of the LNA and mixer. The signal peak at the output of the mixer is reduced by 6 dB compared to the peak at the output of the LNA. The noise power at the output of the mixer is reduced by 3 dB compared to the noise power at the output of the LNA. The reduction in the signal and noise power values is as expected.

desirable band, making the noise figure of the mixer equivalent to 3 dB. The SNR at the output of the mixer SNR_{MXR} is given by,

$$SNR_{MXR} = SNR_{LNA} - NF_{MXR}, \tag{3.8}$$

where NF_{MXR} is the NF of the mixer. The power spectrum of the signal at the output of the mixer is compared with the signal at the output of the LNA in figure 3.14. In figure 3.14, we can see two peaks for the power spectrum at the output of the mixer. The two peaks correspond to the sum and difference frequency (IF1 signal). As expected, the mixer output spectrum peaks in figure 3.14 is reduced by 6 dB compared to the LNA output spectrum. Since the conversion loss of the mixer is 6 dB and the NF of the mixer is 3 dB, the effective noise power at the output of the mixer will be reduced by 3 dB compared to the output of the LNA, as shown in figure 3.14.

3.4.4 BPF

Filters are present in most communication systems. The filters are electronic components used to allow or prevent specific signal frequencies. The filters are crucial in filtering out noise and reducing interference from external signals to improve the performance of communication systems. Generally, the filters can be divided into four categories: band-pass filter, band-reject filter, low-pass filter, and high-pass filter [119]. The BPF transmits a specific frequency band and blocks all the remaining frequencies, thereby reducing the noise present in the receive chain of a radar system. A band-reject filter blocks a specific band of frequency and transmits all the other frequencies. The low-pass filter transmits all the frequencies below a specific value, and the high-pass filter transmits all the frequencies above a specific value. In radars, the BPF is placed outside the mixer to transmit the difference frequency at the mixer's output and block the sum frequency.

3.4.4.1 BPF in simulation

The mathematical model for the signal at the output of the BPF of the whole radar model (S_{BPF}) is given by,

$$S_{BPF}(t) = \frac{A_{LNA}}{2} \cos\left[2\pi f_{IF1} t + 2\pi f_d m T + \theta'\right], \tag{3.9}$$

where $\frac{A_{LNA}}{2} = A_{BPF}$ is the amplitude of the signal after the BPF. The signal power at the output of the BPF will be equivalent to the signal power of the difference frequency. The noise power at the output of the BPF is reduced by a factor of B/B_{BPF}, where B is the noise bandwidth before the BPF and B_{BPF} is the bandwidth of the BPF. The SNR at the

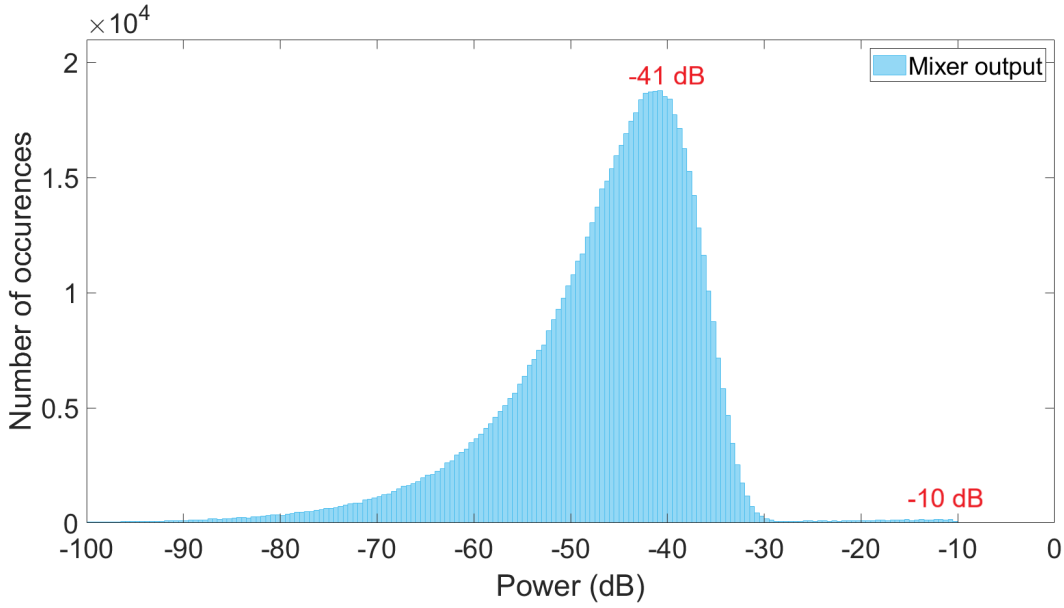

(a) Histogram at the output of the mixer showing the signal power and noise power at -10 dBW and -41 dBW, respectively.

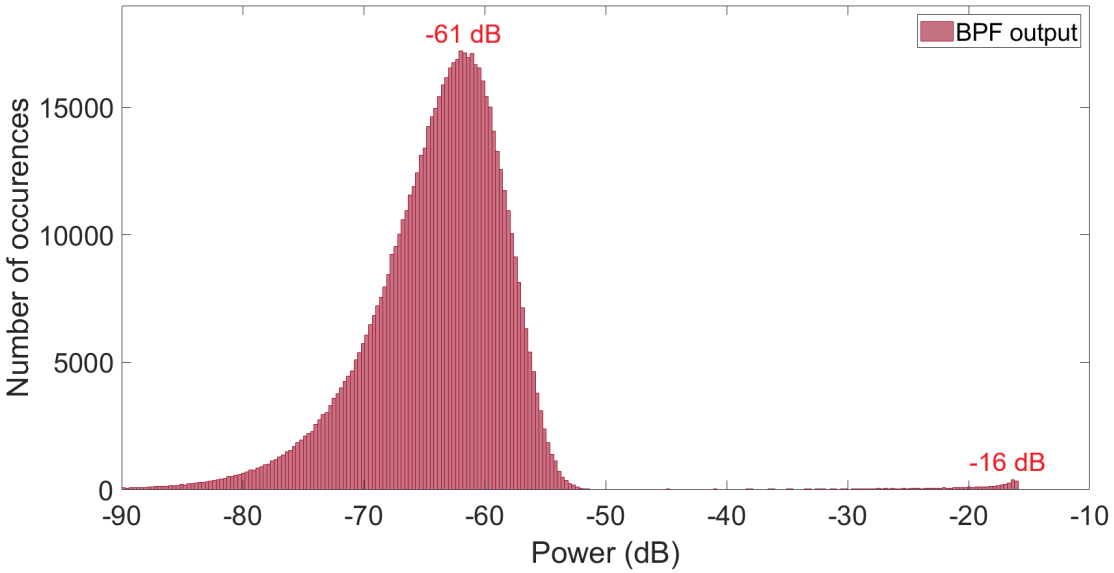

(b) Histogram at the output of the BPF showing the signal power and noise power at -16 dBW and -61 dBW, respectively.

Figure 3.15: The histogram at the output of the mixer and BPF showing the peak signal and noise power values.

output of the BPF (SNR_{BPF}) is given by,

$$SNR_{BPF} = SNR_{MXR} + 10log_{10}(\frac{B}{B_{BPF}}). \tag{3.10}$$

In the whole radar model, a BPF with a bandwidth of 25 MHz was kept at the output of the mixer. The histogram of the output of the mixer and BPF is given in figure 3.15. In figure 3.15a, we can see the signal power and noise power at the output of the mixer peaked at -41 dBW and -10 dBW, respectively. Even though the signal power at the output of the mixer is reduced by 6 dB, since both the frequency peaks are present before filtering, the signal peak at the output of the mixer in figure 3.15a will be the same as the signal peak at the output of the LNA as shown in figure 3.12b. The noise power at the output of the mixer will be reduced by 3 dB compared to the output of the LNA, hence is expected at -41 dBW. In figure 3.15b, we can see the signal power and noise power at the output of the BPF peaked at -61 dBW and -16 dBW, respectively.

Since the BPF allow only the difference frequency at IF, the signal power at the output of the BPF is expected at -16 dBW. The noise power at the output of the BPF will be reduced by a factor equivalent to the bandwidth ratio as given in the equation 3.10. For the 25 MHz bandwidth provided in the simulation, the expected reduction in the noise power after the BPF is 23 dB, which was also confirmed by the power budget calculation. The thermal noise consists of both the desired frequency and the image frequency band. The BPF operates on both the desired frequency band and the image frequency band, resulting in an additional 3 dB noise contribution from the image frequency band. Hence the effective decrease in the noise power after BPF will be 20 dB. In figure 3.15, the noise power at the output of the mixer and BPF are -41 dBW and -61 dBW, respectively, showing a reduction of 20 dB in the noise power after the BPF as expected.

3.4.5 ADC

An ADC is an electronic integrated circuit that converts signals from the analogue to the digital domain. The signals in the analogue domain are continuous signals with continuous values, whereas the signals in the digital domain are represented by a sequence of discrete values [120]. In radars, the ADC is located before the data processing blocks. The important parameters in an ADC are the sampling rate, resolution and quantisation error.

3.4.5.1 Fundamentals of an ADC

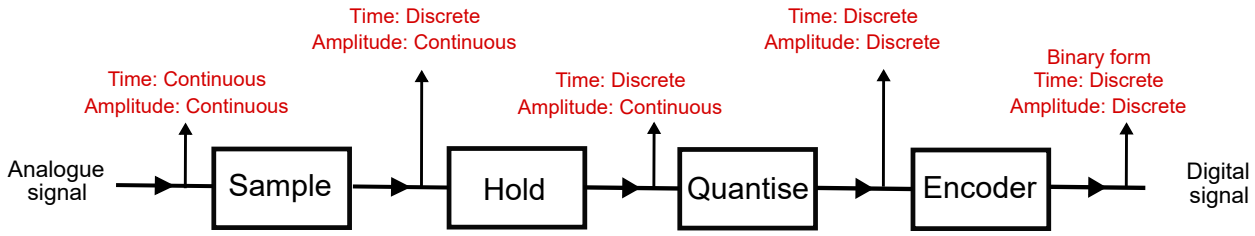

Figure 3.16: Schematic of a typical ADC consisting of sample block, hold block, quantise block, and an encoder block. The input to the ADC is sampled at a required frequency in the sample block and is stored in the hold block until the next sample. The signal is quantised using the quantise block. The digital signal at the output of the quantise block is converted to the binary form in the binary block.

The block diagram of a typical ADC is given in figure 3.16. The sample block is used to sample the ADC input signal at a specific sampling frequency. The input signal of the ADC is continuous in both time and amplitude. The output of the sample block is a signal with discrete time and continuous amplitude. The hold block is used to hold the output of the sample block until the next batch of sample block output [120]. The signal at the output of the hold block is discrete in time and continuous in amplitude and remains unchanged till the next sample set. The quantise block is used for the quantisation of the signal. The continuous analogue amplitude at the input is converted to the discrete amplitude at the

output of the quantise block. The signal at the output of the quantise block is digital since the signal is discrete in both time and amplitude. The last block, the encoder block, converts the digital signal into binary form.

The sampling rate in ADC is defined as the number of samples taken in a second. With the increase in the sampling rate, the ADC can handle higher frequencies. The reconstruction of an analogue signal in the digital domain depends on the sampling rate - the higher the sampling rate, the better the signal is reconstructed. If the sampling rate of an ADC is lower than twice the frequency of the analogue signal, aliasing happens, and the recreated digital signal characteristics differ from the analogue signal.

The digital signals have a discrete and finite number of values and are represented using bits. Each number of bits corresponds to a specific number of steps in the digital signal. The resolution of an ADC is equivalent to the number of bits representing the amplitude of the digital signal. The number of steps increases exponentially with the number of bits. With the increase in bit resolution, the digital signal becomes closer to the original analogue signal.

The digitised signal at the output of the ADC will always be different from the analogue counterpart. The quantisation error is the difference between the analogue signal and the nearest accessible digital signal at each sampling instant. The quantisation error introduces noise in the system known as quantisation noise. Similar to phase noise and thermal noise, quantisation noise also increases the noise floor in the receive chain of radar systems containing ADC. With the increase in the bit resolution, the difference between the digital and the analogue signal decreases, and the quantisation error and the quantisation noise decrease. For an ideal ADC, the quantisation noise and the bit resolution are defined in the signal-to-quantisation noise ratio. The signal-to-quantisation noise ratio for a number

of bits equal to n is given by [121],

$$SQNR = 20log(2^n). \tag{3.11}$$

The equation 3.11 is valid only for a linearly quantised uniform probability density function signal [121]. Similar to quantisation noise, there are other issues caused by ADC, including ADC resolution limiting the overall system range resolution [122].

3.4.5.2 ADC in simulation

The ideal scenario was adding the comprehensive ADC simulation to the whole radar model. Since the signals in the Simulink are already in the digital domain, the ADC in the whole radar model was used to perform the frequency down-conversion through aliasing. The ADC was sampled at a specific ADC clock frequency, and the ADC clock frequency was below the IF1 at the input of the ADC. Through frequency aliasing, the output of the ADC was down-converted to IF2. The ADC was realised in the whole radar model using a signal-to-workspace block. The ADC clock frequency was realised by sampling the signal-to-workspace block at the required sampling frequency. The ADC in the whole radar model has the potential to add further sub-blocks to realise quantisation noise. The mathematical model of the signal at the output of the ADC is given by,

$$S_{ADC}(t) = A_{ADC} \cos\left[2\pi f_{IF2} t + 2\pi f_d m T + \theta'\right], \tag{3.12}$$

where A_{ADC} is the amplitude of the signal after the ADC and is equivalent to the signal amplitude before ADC. The ADC in the simulation does not alter the SNR, and hence the

SNR at the output of the ADC becomes:

$$SNR_{ADC} = SNR_{BPF}. \tag{3.13}$$

The histogram at the output of the ADC is given in figure 3.17. Comparing figures 3.17 and

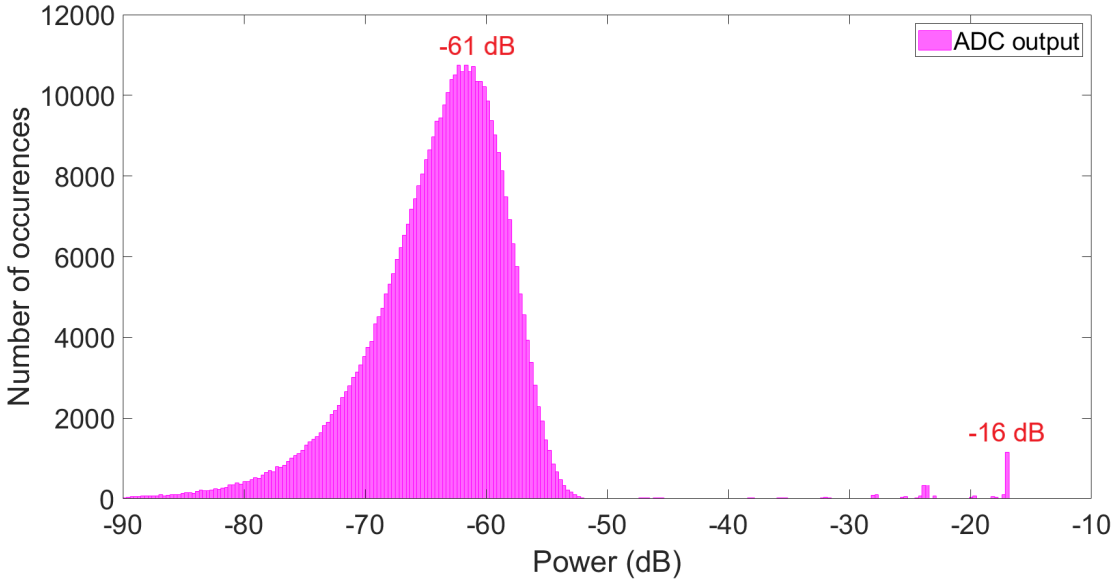

Figure 3.17: The histogram at the output of the ADC showing the signal power and noise power at -16 dBW and -61 dBW, respectively.

3.15b, we can see that there is no relative difference in the signal power or the noise power due to ADC. The signal-to-workspace block carried the Simulink data to the MATLAB workspace. All the radar data processing stages were realised in MATLAB.

3.5 Data processing chain

The radar data processing chain performs the function of both improving the SNR of the signal and calculating the target characteristics. The target characteristics include mainly target range and target Doppler velocity. The processing chain can differentiate the

targets and clutter in terms of range and velocity. One of the important aspects of the data processing chain is the data cube. A data cube is a three-dimensional matrix with receive channel number, slow time and fast time as the three axes. The fast time axis consists of a single PRI. In the final stages of data processing, the fast time axis will be further subdivided into different range bins with a specific range resolution. The slow time axis is updated every PRI. The slow time corresponds to a single PRI, and the adjacent PRI data are stacked along the slow time axis. The fast time and the slow time together represent a data matrix as shown in figure 3.18a. The data cube is an extension of the data matrix with multiple receive channels, as shown in figure 3.18b.

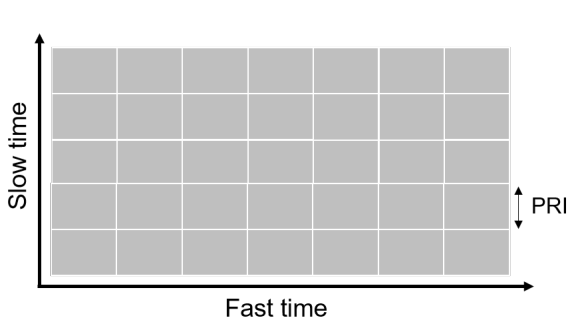

(a) A data matrix consisting of a single PRI in the fast time axis and stacks of PRIs in the slow time axis.

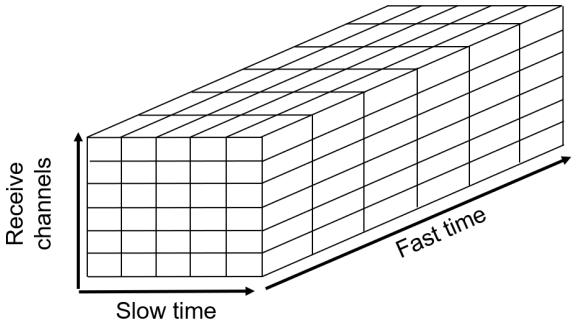

(b) A data cube consisting of data matrices from each receive channel stacked over each other.

Figure 3.18: Illustration of a data matrix and data cube in the data processing chain of a radar system.

In the data processing chain, one of the methods to improve the SNR is by performing beam-forming. Beam-forming is performed in cases where multiple receive antenna elements are present in a radar system. In radars, beam-forming is the technique in which the receive antenna arrays can be focused over any angle in the elevation and azimuth to improve the SNR. The whole radar model currently consists of only one receive antenna element; hence, the beam-forming is not performed in the data processing chain of the radar simulation. The components in a radar system's data processing chain depend on the radar's function. In a pulsed Doppler radar system, the data processing chain typically consists of Hilbert trans-

form, matched filtering, windowing, FFT, and range-Doppler plot generation. Alternative to the Hilbert transform, the radar data processing chain can also have in-phase/quadrature outputs and a pair of ADCs or a single ADC and a multiplier combination. The Hilbert transform is the process of generating a complex-valued signal from a real-valued signal [123]. Matched filtering involves the convolution of an unknown signal with a conjugated time-reversed reference signal to improve the SNR of the signal in the presence of random noise [119]. In the whole radar model, the Hilbert transform and the matched filtering block is used to perform both operations on the signal at the output of the ADC.

In radars, the FFT is performed to extract the frequency-domain information of the time-domain signal. The Fourier transform is also used to improve the SNR through pulse integration. The pulse integration can follow coherent and non-coherent fashion depending on the signal characteristics. The FFT is applied across the slow time axis. In the whole radar model, windowing is performed prior to the FFT to reduce the frequency components' leakage effects on the Fourier transform. A range-Doppler plot is generated by performing an FFT across the slow time axis of a data matrix. In the whole radar model, the windowing and FFT are followed by range-Doppler plot generation to provide the range and Doppler information of both the targets and clutter.

3.5.1 Hilbert transform and Matched filtering

In data processing, the Hilbert transform is defined as a linear operator when acted on a real-valued function $x(t)$ produces function $H[x(t)]$ [124, 125]. Mathematically, the Hilbert transform of $x(t)$ is given as [123],

$$\hat{x(t)} = H[x(t)] = x(t) * \frac{1}{\pi t}, \tag{3.14}$$

where $*$ denotes convolution operation. The Hilbert transform helps to generate an analytical signal. An analytic signal is a complex-valued function with no negative frequency components. The real and imaginary parts of an analytic signal are real-valued functions related to each other by the Hilbert transform. The analytic signal at the output of a Hilbert transform can be defined as,

$$z(t) = x(t) + jx\hat{(}t). \tag{3.15}$$

The real and imaginary parts of the equation 3.15 are known as the in-phase and quadrature values. In the frequency domain, the Hilbert transform imparts a phase shift of 90^o to the signal. In radars, the Hilbert transform is one of the methods used to down-convert the signal to the baseband. The Hilbert transform is generally performed through quadrature detection, where an IF signal is down-converted to the baseband along with the generation of the in-phase and the quadrature baseband signal. Hilbert transform and the generation of the analytic in-phase and quadrature signals are crucial in data processing and Doppler velocity calculation [126].

In communication systems, the matched filter is used as a linear filter to improve the SNR of a signal in the presence of additive white Gaussian noise. For an ideal matched filter, maximum SNR is obtained when the reference signal is a time-delayed mirror image of the received signal [119].

3.5.1.1 Hilbert transform and matched filtering in simulation

In the whole radar model, the Hilbert transform and matched filtering block was used to bring the IF2 down to the baseband and to perform matched filtering. The simplified mathematical model of the baseband complex signal at the output of the Hilbert transform

is given by,

$$S_{HT}(t) = A_{HT}e^{(2\pi f_d mT+\theta')}, \tag{3.16}$$

where A_{HT} is the signal's amplitude after the Hilbert transform. The complex baseband radar signal is used to measure the phase and amplitude independently [102]. The matched filter for the whole radar model was derived from the transmitted pulse. The MATLAB code for matched filtering was used to generate the matched filter output. The mathematical model of the signal at the output of the matched filter is given by,

$$S_{MF}(t) = A_{MF}e^{(2\pi f_d mT+\theta')}, \tag{3.17}$$

where A_{MF} is the signal's amplitude at the output of the matched filter. The crucial parameter in matched filtering is the gain of the matched filter. The gain of the matched filter is dependent on the matched filter coefficient. For a matched filter that provides an SNR gain of G_{MF}, the SNR at the output of the matched filter (SNR_{MF}) is given by,

$$SNR_{MF} = SNR_{ADC} + G_{MF}. \tag{3.18}$$

The time domain representation of the signal at the input and output of the matched filter is given in figure 3.19. A rectangular pulse undergoes matched filtering to output a triangular waveform. Since matched filtering performs the correlation between the input signal and the reference signal, the matched filtered output of a rectangular pulse will be peaked at the endpoint of the input signal. For any finite input signal, the duration of the matched filter output is twice the duration of the input signal [102]. Since the input to the matched filter is a near rectangular pulse and the reference derived from the transmit signal

is also a near rectangular pulse, the output of the matched filter in figure 3.19 is a triangular pulse as expected. The duration of the matched filter output in figure 3.19 is twice the duration of the input signal and is also peaked at the endpoint of the input signal. The histogram at the output of the matched filter is given in figure 3.20. The signal and noise power at the output of the matched filter is 79 dB and 23.5 dB, respectively. Comparing figures 3.20 and 3.17, we can see the SNR at the output of the matched filter improved by a factor of 10.5 dB. The improvement by matched filtering is very close to the expected value confirmed using the staring radar power budget.

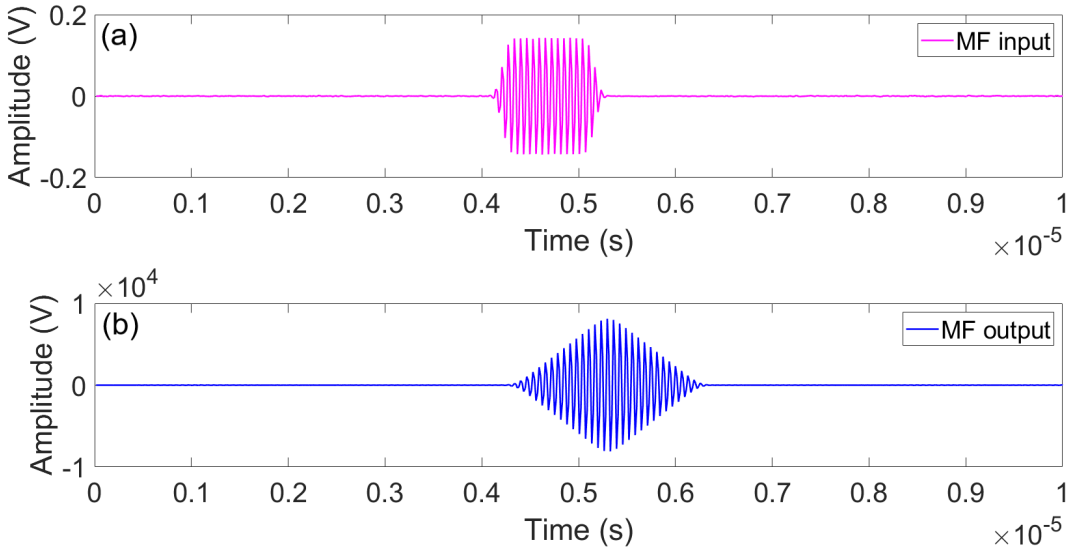

Figure 3.19: Time domain representation of (a) signal at the input of the matched filter, (b) signal at the output of the matched filter.

3.5.2 Windowing, FFT and range-Doppler plot

Fourier analysis converts a signal in its time or space domain to a representation in the frequency domain or vice versa. An FFT is an algorithm to perform Fourier analyses, including both the discrete Fourier transform (DFT) and the inverse discrete Fourier transform (IDFT). The DFT of a signal is obtained by decomposing the signal into its frequency

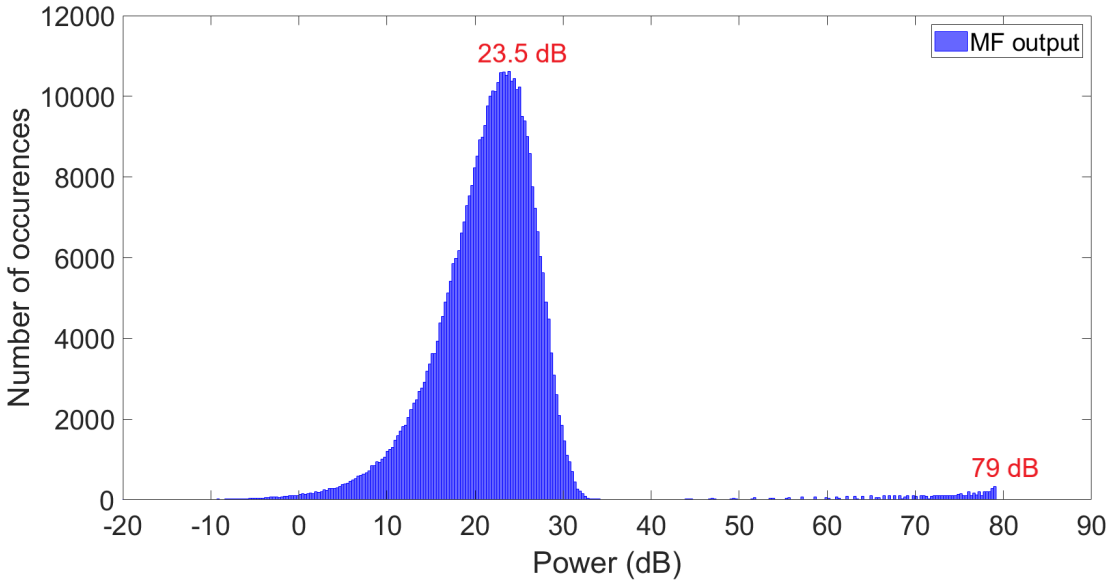

Figure 3.20: The histogram at the output of the matched filter showing the signal power and noise power at 79 dB and 24.5 dB, respectively.

components. The FFT is used in a wide range of applications in communication systems.

Performing FFT on a data matrix or data cube results in a range-Doppler plot with the slow time converted to the Doppler axis and fast time converted to the range axis. The Doppler axis consists of Doppler bins, and the range axis consists of range bins. Generally, in pulsed Doppler radars, the range-Doppler plot is used to represent the processed data from the radars. The range-Doppler plot consists of the range and Doppler information of targets and clutter. The range-Doppler plot can also be used to analyse the relative signal strength from different scatterers and to evaluate the effect of phase noise in radar target detection.

In radars, the FFT also performs pulse integration to improve the SNR. Since the FFT is performed along the slow time, the pulse integration is also performed along the slow time axis that consists of stacks of received pulses. The FFT performs coherent integration of both the signal and the noise. For a coherent integration of N pulses consisting of both the signal and noise, the power in the integrated signal component is increased by N^2 and

the integrated noise power is increased by N. Hence, the effective increase in the SNR is N in dB.

For any timed-domain signal undergoing Fourier transform to the frequency domain, the discontinuities due to the non-integer number of periods of the waveform result in frequency components leaking into adjacent frequency bins. The leakage causes the fine spectral lines in FFT to spread and is known as spectral leakage [127]. The spectral leakage is minimised by a technique known as windowing. The windowing multiplies the measured time domain discontinuous signal with an amplitude envelope that approaches zeros at both ends [128]. The SNR at the output of the windowing is degraded by a factor known as the loss factor. The loss factor is defined as the ratio of the maximum achievable SNR (SNR without windowing) to the actual SNR (SNR with windowing) [129]. There are different kinds of windowing functions, each with their own characteristics. Commonly used windowing functions include Hamming, Hann, and Blackman-Harris windows. Depending on the application, there are different kinds of windowing functions, including Hamming, Hanning, and Blackman-Harris. Both the Hann and Hamming window functions are sinusoidal and result in large peaks with low side lobes. Unlike the Hann window, Hamming does not reach zero on both ends, resulting in a slight discontinuity in the signal. The Hann window, however, reaches zero on both ends, erasing all discontinuity. The Blackman Harris window reaches zero on both ends, with the advantage of considerably better sidelobe compression. Hamming and Hann windows are used in applications with desirable frequency resolution, but moderate sidelobe levels are acceptable. Blackman-Harris windowing is used in applications where the lowest sidelobe levels are a priority.

3.5.2.1 Windowing, FFT and range-Doppler plot in simulation

The whole radar model applies windowing to the time domain signal before performing the FFT to generate the range-Doppler plot. The reference staring radar requires better sidelobe compression, and hence the reference staring radar uses the Blackman-Harris windowing. Following the staring radar, Blackman-Harris windowing was applied in the data processing chain of the radar model. The SNR at the output of windowing (SNR_W) is given by,

$$SNR_W = SNR_{MF} - LF, \tag{3.19}$$

where LF is the loss factor of the Blackman-Harris window. The FFT was performed after windowing. The SNR at the output of the FFT (SNR_{FFT}) is given by,

$$SNR_{FFT} = SNR_W + N, \tag{3.20}$$

where N is the number of pulses. Depending on the requirements, the FFT can be performed with any number of pulses. In the whole radar model, the FFT was performed with 2048 pulses ($N = 2048$). Since only a single stationary test target was present in the simulation, the FFT with 2048 pulses considerably reduces the number of occurrences of the target peak in the histogram. Hence, it is impossible to represent the signal power at the output of the FFT in the histogram plots. The range-Doppler plot with the stationary target at 600 m is given in figure 3.21. Figure 3.21 consists of the range-Doppler plots with and without Blackman Harris windowing. A range Doppler plot consists of a number of range bins on the vertical axis depending on the configuration of the radar. The number of Doppler bins in the horizontal axis is the same as the number of pulses used to generate the range-Doppler plot. The range-Doppler plot in figure 3.21 consists of 15 range bins and central Doppler bins equivalent to a span of 1400 Hz.

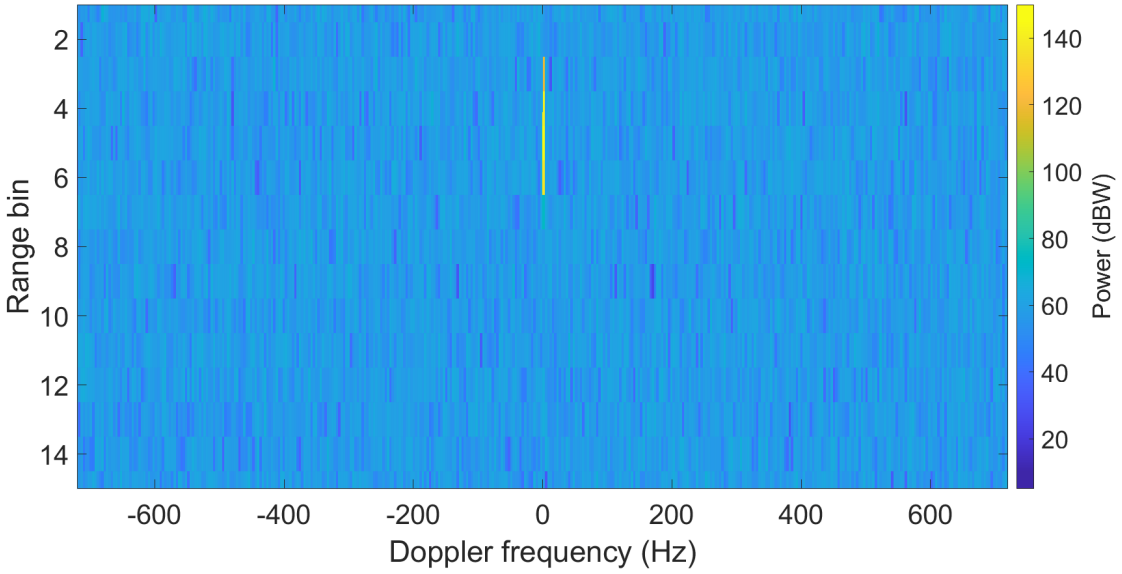

(a) Range-Doppler plot without Blackman-Harris windowing showing a target peak power of 145 dB and average noise power of 56.5 dB, equivalent to an SNR of 88.5 dB.

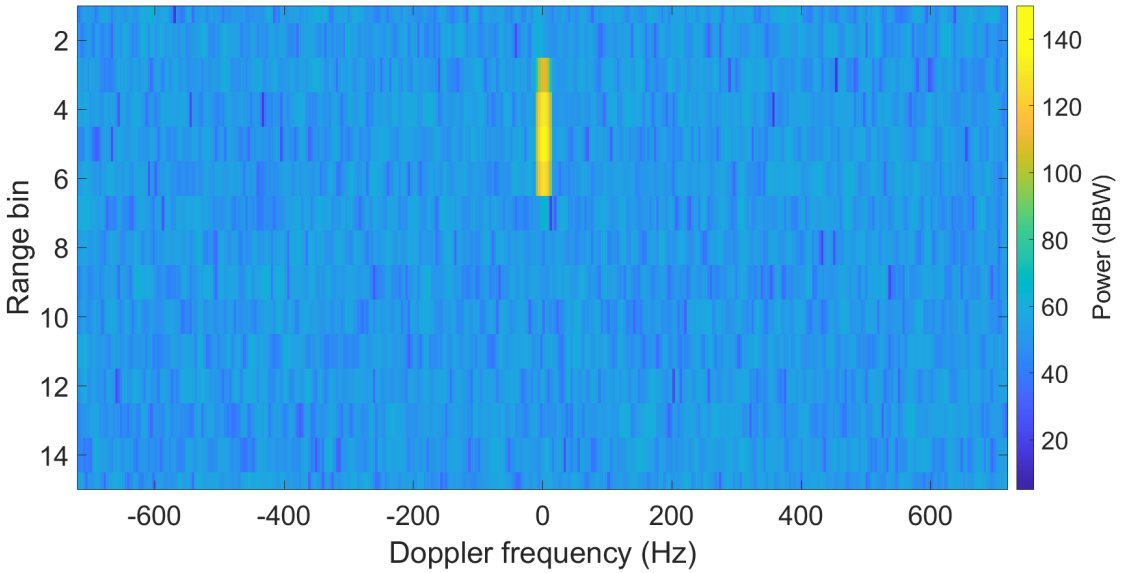

(b) Range-Doppler plot with Blackman-Harris windowing showing a target peak power of 136 dB and average noise power of 51 dB, equivalent to an SNR of 85 dB.

Figure 3.21: Simulated range-Doppler plots of a stationary test target at 600 m consisting of 15 range bins and central Doppler bins equivalent to 1400 Hz.

An FFT of 2048 pulses provides an SNR gain of 33 dB. The range-Doppler plot without the Blackman-Harris window in figure 3.21a has a target peak power of 145 dB and

average noise power of 56.5 dB, equivalent to an SNR of 88.5 dB. Since the SNR at the output of the MF was 55.5 dB, as depicted in figure 3.20, the 88.5 dB SNR at the output of the FFT is equivalent to the expected value of a 33 dB increase in the SNR. The range-Doppler plot with the Blackman-Harris window given in figure 3.21b has a target peak power of 136 dB and average noise power of 51 dB, equivalent to an SNR of 85 dB. The SNR of 85 dB at the output of the FFT with windowing is 3.5 dB lower than the value of 88.5 dB at the output of the FFT without windowing. The windowing follows the loss factor of the Blackman-Harris window. The loss factor of a Blackman-Harris windowing is between 3 - 3.5 dB [129], and the SNR values calculated from figure 3.21 also show a loss factor of 3.5 dB. In the simulation, the waveforms in the Fourier transform with stationary targets consist of only an integer number of periods. Hence, the frequency spread to adjacent frequency bins will not be visible in the stationary targets.

3.6 Validation of radar model

A radar model can be validated by comparing the results of a radar model with both theory and real radar data. By comparing the important metrics in the range-Doppler plot, it is possible to evaluate and validate a simulated radar model with a real radar in the best possible way. The SNR and clutter-to-noise ratio (CNR) are the two important metrics in radar target detection and hence in range-Doppler plots.

The whole radar model described in this chapter benefits from the ability to simulate targets and clutter in the environment at any given range, velocity, and RCS. The whole radar model is validated by comparing the simulated results with the experimentally measured results from the L-band staring radar. The validation of the radar model was facilitated by generating simulated data equivalent to a full coherent processing interval (CPI). The CPI

consisted of a time duration equivalent to 2048 PRIs. An actual range-Doppler plot from a radar trial was compared with the simulated range-Doppler plot to validate the model. A number of range bins and 2048 Doppler bins make up the real range-Doppler plot.

Three different comparisons were performed to verify the correctness of the simulated whole radar model. The system-level signal powers and SNR values at the output of the various blocks of the simulation were compared with the expected values in the first step. The fundamental parameters from the generated range-Doppler plot and the fundamental parameters from the real radar were compared in the second step. The CNR, the SNR, and the thermal noise floor from the simulated and real range-Doppler plots were compared at the third. In all three comparisons, the uncertainty in the power calculations was kept at 0.1 dB.

3.6.1 Comparison of system-level signal power and SNR

The first level was performed by comparing the SNR and the system-level signal power at the output of different building blocks in the transmit chain, the receive chain, and the data processing chain. A single stationary clutter was simulated at a range of 600 m and an arbitrary RCS value in the first stage. Simulation time equivalent to a full CPI was performed. The signal power, noise power, and SNR values were measured using the test probes placed at the output of the building blocks within the radar model. It is convenient to divide the first stage further into two sections. The signal powers are compared in the first section, and the SNR values are compared in the second.

In the first section, the simulated signal power at the output of the transmit amplifier, the transmit antenna, and the receive antenna, as given in the figures 3.7 and 3.8 is compared with the expected values. The expected value of the signal power at the output of the

Radar block	Simulated (dB)	Expected (dB)	Difference (dB)
Transmit amplifier	33.0	33.0	0.0
Transmit antenna	45.5	45.5	0.0
Receive antenna	-74.5	-74.4	0.1

Table 3.1: Simulated and expected values of signal powers at the output of different radar building blocks. The uncertainty for the calculations was kept at 0.1 dB.

transmit amplifier and the transmit antenna was taken from the staring radar power budget. The expected value of the signal power at the output of the receive antenna was calculated from the radar range equation (equation 2.1). The comparison of the simulated and expected values of signal powers are summarised in the table 3.1. Table 3.1 shows the expected values of the signal power at the output of the transmit amplifier and the transmit antenna precisely the same as the expected value. Since the simulator follows the equation 3.3, exact values are expected between the two. The simulated value of the signal power at the output of the receive antenna is offset by a negligible value of 0.1 dB. Again, since the radar model simulator follows the equation 2.1 with all the conditions ideal, including the environment with no atmospheric loss, the closeness between the values at the output of the receive antenna is expected.

Radar block	Simulated (dB)	Expected (dB)	Difference (dB)
Before LNA	32.5	32.6	0.1
After LNA	28.0	28.1	0.1
After mixer	25.0	25.1	0.1
After BPF	45.0	45.1	0.1
After ADC	45.0	45.1	0.1
After matched filter	55.5	55.1	-0.4
After FFT	88.5	88.1	-0.4

Table 3.2: Simulated and expected values of SNR at different stages in receive chain and data processing chain building blocks

The simulated SNR at the output of each building block in the receive chain and data processing chain was compared to the expected values of the SNR in the second section. The

simulated SNR values were determined using the signal power and thermal noise power at each building block's output. Radar theory and power budget reference values were used to compute the expected SNR values. The simulated and expected values of the SNR at the outputs of different radar building blocks are summarised and compared in the table 3.2. Table 3.2 shows a good agreement between the simulated and the expected SNR values at the output of every building block. The constant offset of 0.1 dB between the expected and the simulated SNR is present in all the values of SNR starting from the receive antenna. The difference of 0.1 dB in table 3.2 is attributed to the small difference in the parameters for the target modelling. The SNR at the output of the matched filter and the FFT in table 3.2 is offset by -0.4 dB. The difference of -0.4 dB is the net effect of 0.5 dB disparity in the expected and simulated value of SNR gain in matched filtering, along with the constant offset of 0.1 dB present across all building blocks. The high parity between the simulated and expected values of the system-level signal power and the SNR represented in the table 3.1 and 3.2 shows the fidelity of the building blocks of the simulated radar model with the theory and staring radar power budget.

3.6.2 Comparison of range and Doppler basic parameters

Having compared the system-level signal power and SNR in the first level of comparison in section 3.6.1, the fundamental parameters from the range-Doppler plots of both the simulation and staring radar are compared in the second level. Along with the stationary clutter at 600 m and an arbitrary RCS, a moving target at a range of 1500 m and an arbitrary RCS was also simulated in the second level. The RCS and range values were arbitrary and did not adhere to any particular reference. The target was kept moving at 251 Hz, equivalent to a velocity of 30 m/s for the particular L-band transmit frequency of the radar. A range-Doppler plot with thermal noise was simulated using the whole radar model,

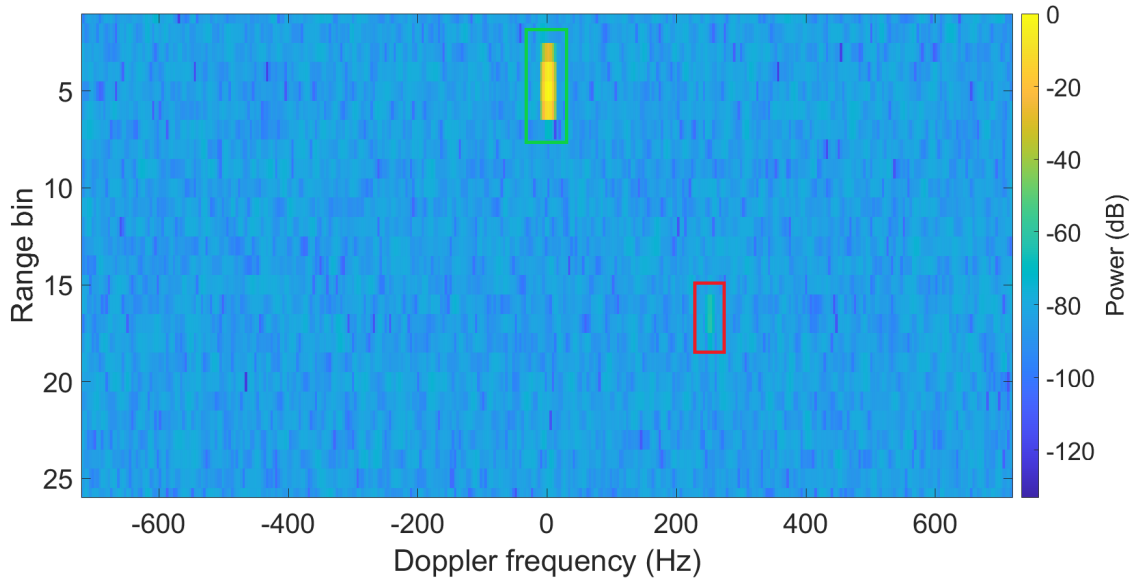

Figure 3.22: Simulated range-Doppler plot with range bin in the vertical axis and Doppler frequency in the horizontal axis. The spectrum is shown for -700 to +700 Hz. The single stationary clutter and the single Doppler target are highlighted within a green and red box, respectively. The range-Doppler plot is normalised to the clutter.

consisting of both the clutter and the target.

The simulated range-Doppler plot consisted of a number of range bins. The PRF of the simulated range-Doppler plot was the same as the staring radar range-Doppler plot. Figure 3.22 shows the simulated range-Doppler plot with the range bin on the vertical axis and the Doppler frequency on the horizontal axis. Figure 3.22 clearly shows a target (highlighted in red) with a Doppler frequency of around 251 Hz and a stationary clutter (highlighted in green) with a Doppler frequency of 0 Hz, confirming the ability of the whole radar model to simulate target and clutter at user-defined velocities.

The second level compares the range and Doppler basic parameters, including range bin, Doppler bin, range resolution, and Doppler resolution for both the simulated radar model and the L-band staring radar. Figure 3.22 was used to measure the range and the Doppler bin for both the target and the clutter. The range resolution and the Doppler resolution for the simulated whole radar model were also calculated from the dataset that

constitutes figure 3.22. The difference between the range values of any two adjacent range bins provides the range resolution, and the difference between any two adjacent Doppler bins provides the Doppler resolution. Technically, the radar model tries to replicate the range and Doppler resolution of reference radar, and there is good agreement in the range resolution and Doppler resolution between the simulated radar model and the real radar. The comparison of the basic parameters, including the range bin and the Doppler bin for the simulated radar model and the staring radar, are summarised in table 3.3.

Parameter	Simulated	Expected
Clutter range bin	5	5
Target range bin	17	17
Clutter Doppler bin	0	0
Target Doppler bin	70	70

Table 3.3: Simulated and expected values of range and Doppler basic parameters

The simulated values correspond to the values measured from the simulated range-Doppler plot in figure 3.22. The range resolution and Doppler resolution of the staring radar from the radar power budget were used to calculate the expected values of the range bin and the Doppler frequency bin for both the clutter and the target. Table 3.3 shows that the basic parameters from the simulation are the same as the expected parameters from the actual radar. The section concludes that the radar model has the ability to replicate staring radar range and Doppler basic parameters in the simulation. The radar model discussed in this chapter has the potential to optimise all the basic parameters, including the range resolution, Doppler resolution, CPI, and PRF, to any user-required configuration.

3.6.3 Comparison of whole range-Doppler plots

The third stage compares and validates the CNR, SNR, and thermal noise floor from the simulated range-Doppler plot with the real radar range-Doppler plot. The range-Doppler plot of an actual radar experiment was used as a reference for the third level of comparison.

The L-band staring radar was used for the actual radar trial, conducted on an airfield with a controlled drone (the target of interest) flying along a predetermined course. The real range-Doppler plot was made up of a single frame from a single beam at a fixed azimuth and elevation angle centre on the direction of the target of the drone radar trial, equivalent to a complete CPI. For the chosen frame, the drone approached the radar at a specific distance and radial velocity of 8.3 m/s. Even though the radar trial was performed in a rural environment, the real range-Doppler plot consisted of other unwanted targets in the radar's field of view.

The third stage of comparison was performed by simulating the actual range-Doppler plot using the whole radar model. At first, the clutter profile of the range-Doppler plot was modelled in the simulation. The clutter power was measured at each range bin of the range-Doppler plot from the actual radar trial. The clutter power is then used to back-calculate using the radar range equation and power budget values from the reference staring radar to find the RCS of the clutter corresponding to each range bin. The calculated RCS values are then used to add radar clutter to the simulation. In the simulation, a single clutter corresponding to the RCS of the clutter for every range bin calculated using the method described above was kept at the centre of every range bin. The current radar model cannot simulate the exact replica of the clutter for every range bin since each range bin's clutter power leaks to the neighbouring range bins, and it is impossible to back-calculate and find the exact values of RCS. The range-Doppler plot from the simulated and real radar trial was used to obtain the peak clutter powers at each range bin. At this stage of comparison, the CNR is calculated, taking into account only the thermal noise for both the simulated and actual range-Doppler plots.

Table 3.4 compares the CNR from the simulated range-Doppler plot with the CNR from the real range-Doppler plot for different range bins. The real radar environment consists of various clutter, each with a different RCS. Since the simulation consists of only a

Range bin	Simulated CNR (dB)	Expected CNR (dB)	Difference (dB)
A	103.4	105.7	2.3
B	94.9	90.1	-4.8
C	93.9	91.9	-2.0
D	96.8	96.8	-0.0
E	65.2	64.9	-0.3
F	73.2	72.8	-0.5

Table 3.4: Clutter-to-noise ratios from simulated and real range-Doppler plots for different range bins

single clutter in each range bin and since the clutter power from each range bin leaks to the adjacent range bins, it is acceptable to have a few dB of variation in the CNR levels between the simulation and the expected data. The values in table 3.4 demonstrate a strong agreement between the simulated and real CNR.

The second step in the final level of comparison added the target information to the range-Doppler plot in simulation. The target drone was represented in the simulation as an object at a distance equal to the target's real range. The target's Doppler frequency was simulated at 69.8 Hz, equivalent to the drone velocity of 8.3 m/s. The DJI Inspire 2 drone was used in the real trial. The RCS of the drone taken from the reference [130, 131] and extracted using the back calculation from the real radar trial were very close to each other, within a few dBsm (decibels relative to square meters). The RCS value extracted from the experiment was used in the simulation.

For any real radar, phase noise plays a significant role in target detection. The radar system's phase noise causes the range-Doppler plot's phase noise floor to emerge out of the thermal noise floor in range bins with stronger clutter power. The increase in the overall noise floor makes the detection of targets difficult.

The comparison of the simulated range-Doppler plot with the real range-Doppler plot is given in figure 3.23. Both the range-Doppler plots in figure 3.23 are normalised to the

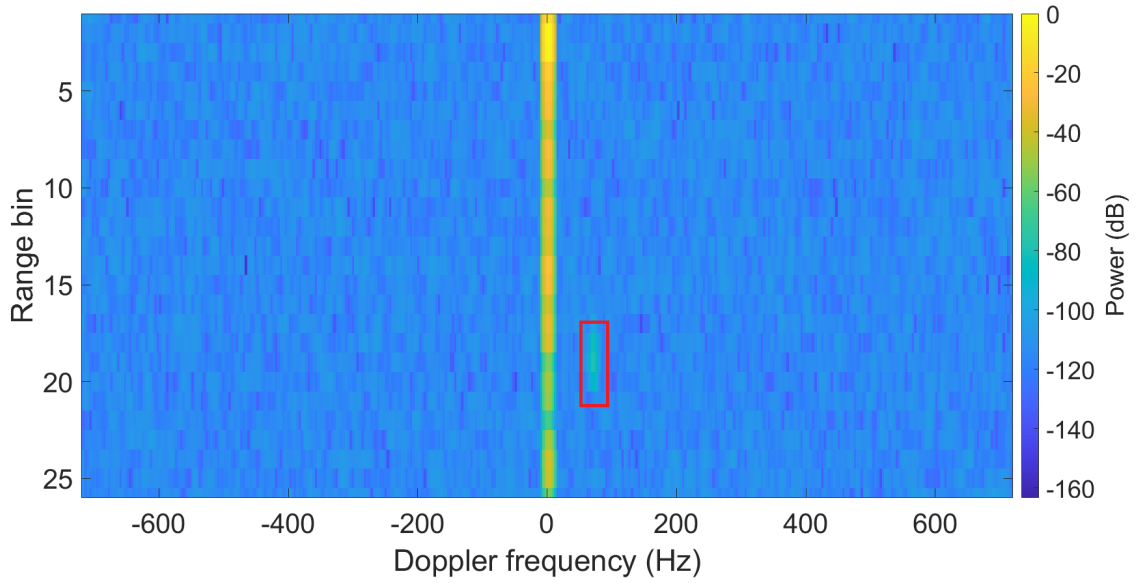

(a) Simulated range-Doppler plot without the oscillator phase noise. The plot consists of the stationary clutter and a single simulated target in the uniform thermal noise floor.

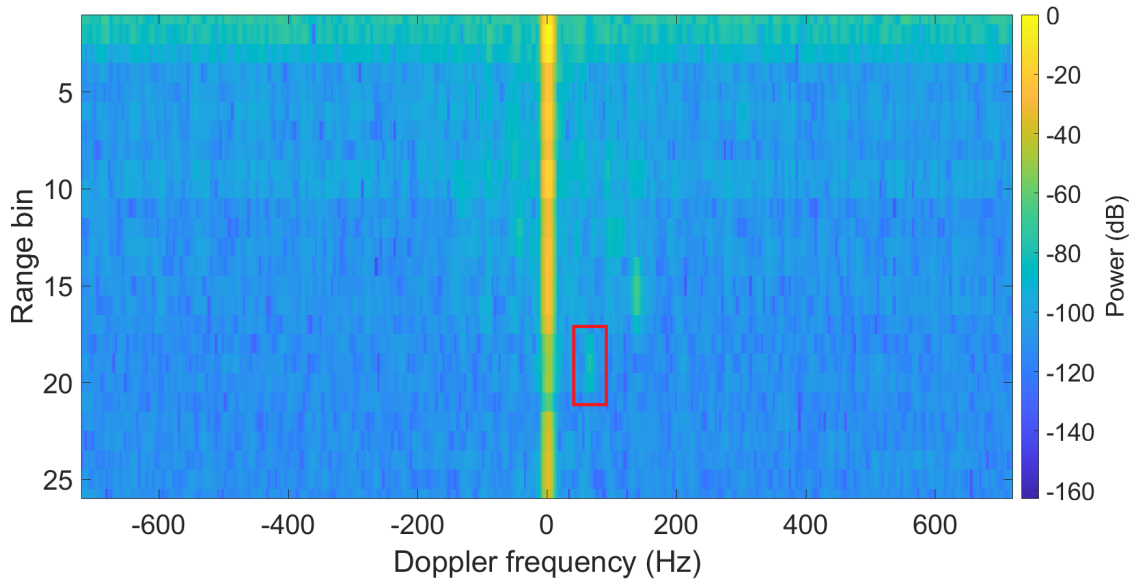

(b) Real range-Doppler plot from the staring radar trial at an airfield. The phase noise floor is seen emerging from the thermal noise floor for range bins with higher clutter. The plot also consists of other unwanted targets as seen by the radar. The integration time for the radar measurement is around 0.3 s.

Figure 3.23: Comparison of the simulated range-Doppler plot with the real range-Doppler plot. Both the range-Doppler plots are normalised to the strongest clutter. The target is highlighted in the red box. The target is present across both the plots in the same range and Doppler bin.

strongest clutter. Figure 3.23a shows the simulated range-Doppler plot, and figure 3.23b shows the real range-Doppler plot. In figure 3.23b, the increase in the overall noise floor and the emergence of the phase noise floor over the thermal noise floor is visible at ranges with extremely high clutter. Since the phase noise is not added to the whole radar model simulation, the simulated range-Doppler plot in figure 3.23a consists only of the uniform thermal noise floor. The real range-Doppler plot in figure 3.23b also consists of extra peaks corresponding to the unwanted targets in the radar field of view.

Apart from the phase noise floor and unwanted targets, the simulated and the actual range-Doppler plot are qualitatively similar in figure 3.23. The clutter power for each range bin independently does not match because the CNR for each range bin cannot be precisely recreated in the simulation. The target of interest is highlighted inside a red box for both the range-Doppler plots in figure 3.23. In both the simulated and real range-Doppler plots, the target appears at the 19^{th} range bin and 19^{th} Doppler bin. The signal-to-thermal noise ratio of the target was calculated from both the simulated and real range-Doppler plots and is given in the table 3.5. Table 3.5 shows an excellent agreement between the simulated and the real signal-to-thermal noise ratio. The high level of parity in signal-to-thermal noise ratio confirms the ability of the whole radar model to simulate a range-Doppler plot with the target and thermal noise floor that replicates the values from a real range-Doppler plot. One crucial difference between figure 3.23a and 3.23b is the presence of phase noise floor in 3.23b, which is not modelled in figure 3.23a. The introduction of the phase noise in the radar simulation and the effects of the phase noise in the range-Doppler plot is discussed in detail in chapter 5.

Parameter	Simulated	Real
Signal-to-thermal noise ratio (dB)	33.17	32.34

Table 3.5: The calculated signal-to-thermal noise ratio from the simulated and the real range-Doppler plots

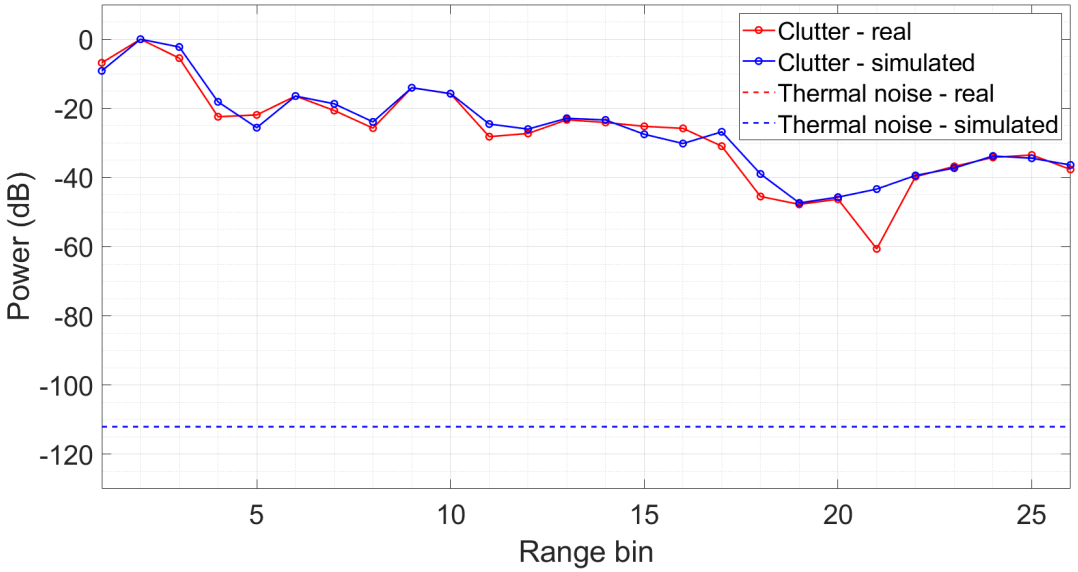

Figure 3.24: The comparison graph shows the clutter power and the thermal noise floor for every range bin. The comparison graph consists of data from the real and simulated range-Doppler plots. The clutter power for both the simulation and real data overlap to a good extent. The thermal noise floor in simulation fully overlaps with the real data and hence is not differentiable.

The peak clutter power and the thermal noise floor for each range bin were taken from the figures 3.23a and 3.23b to generate a comparison graph. The thermal noise floor refers to the noise floor for the range bin considerably away from the radar, where the effect of the clutter-induced phase noise is negligible. The graph in figure 3.24 compares the simulated and the real range-Doppler plot from the figures 3.23a and 3.23b, respectively. The inclusion of phase noise in the radar model and the effects of phase noise in radar systems, and the resulting range Doppler plots are discussed in detail in chapter 5.

Figure 3.24 clearly shows the overlapping thermal noise floor for both the real and simulated range-Doppler plots. The comparison graph also shows a good agreement between the simulated and real clutter power. The clutter power for the range bin 21 from the real range-Doppler plot was an exception which could not be replicated in the simulation. The clutter in real radar consists of complex objects and other weather phenomena in the radar

field of view. In contrast, the clutter in the simulation is represented by a single stationary clutter in each range bin. Since the pulse width of the radar is longer than the range bin, there is an extra effect of leaking the clutter power to the adjacent range bins. Because of these two effects, the clutter power in every range bin cannot be replicated with full parity in the simulation. Figures 3.23a, 3.23b, and 3.24, along with tables 3.4 and 3.5 show confidence and fidelity of the whole radar model to replicate real staring radar trial in the simulation.

3.6.4 Real radar trial

The real radar trial consisted of controlled drones flying at a predetermined trajectory. Throughout different trials, different drones, including DJI Inspire 2, DJI Mavic, and DJI Matrice, were used. For the radar trial discussed in the thesis, the DJI Inspire 2 drone was used. The reference staring radar was at the Cranfield airport facility, overlooking the airport runway. The drone was flown in a predetermined Pacman trajectory, as shown in figure 3.25. The waypoints of the trajectory are given in table 3.6. The range-Doppler plot generated from a single frame of data from this radar trial is used as the reference range-Doppler plot. For the specific frame under consideration, the DJI Inspire 2 drone was flying at a Doppler velocity of 8.3 m/s.

Waypoint	Latitude	Longitude
HOME	52.078851	-0.612639
P1	52.080149	-0.611053
P2	52.080304	-0.614284
P3	52.078391	-0.615001
P4	52.077599	-0.613477
P5	52.077709	-0.611711
P6	52.079073	-0.610545
END	52.078753	-0.612708

Table 3.6: Waypoints for the Pacman trajectory used in the real radar trial

Figure 3.25: Pacman trajectory for the real radar trial with DJI Inspire 2 drone.

3.7 Conclusion

This chapter presented the development of the radar model in the simulation and the comparison of the radar model with data from the real radar. A radar model consisting of all the fundamental building blocks in the transmit chain, the receive chain, and the data processing chain, along with targets and clutter in the environment, is a powerful tool to test hypothetical and real radar scenarios. Such a whole radar model was developed from scratch in this chapter, with a focus on the behaviour of the radar hardware building blocks, with reasonable simplifications. The radar simulator can take the fundamental parameters for each radar building block, which is discussed in detail in the chapter. The radar model was validated by comparing the results generated in the simulation with the actual experimental results from the L-band staring radar. The radar model was capable of replicating the real radar parameters at various levels.

A detailed study that characterises the performance of different classical and quantum oscillators will enable the comprehensive radar model to analyse the limitations of conventional radar oscillator phase noise and explore the potential advantages of quantum oscillators in radar systems. Such a detailed study of oscillators focussing on Allan deviation and phase noise is presented in chapter 4.

Chapter Four

OSCILLATORS

This chapter provides a detailed analysis of the performance of different classical and quantum oscillators. The characterisation of oscillators discussed in this chapter is applied to the comprehensive radar model presented in chapter 3 to study the limitations of conventional radar oscillators and to explore the potential of the quantum oscillator in radar systems. The chapter starts with a discussion of different kinds of oscillators and the oscillators available in the laboratory. The reader is then directed to a discussion on the two figures of merit significant to oscillators: Allan deviation and phase noise. The methods to measure the Allan deviation and phase noise of different oscillators and the measurement results are also discussed in the chapter.

4.1 Types of Oscillators

An oscillator is an electronic or mechanical device that generates a periodic output signal [132]. Oscillators are present in various primary devices, including radios, computers, and quartz clocks [132]. The amplitude-modulated radio transmitters use an oscillator to generate a specific frequency wave for the radio stations. In computers, specialised oscillators

generally made of quartz are used as master timing devices. A quartz clock uses a quartz oscillator to keep track of the time [133].

A typical example of a mechanical oscillator is a pendulum, whereas an inductor-capacitor (LC) oscillator is an example of an electric oscillator. Energy needs to move back and forth between different forms for an oscillation to occur. In pendulums, the energy switches between potential energy and kinetic energy. In LC oscillators, the energy switches between an electrostatic and magnetic field. Electronic oscillators generally use circuits with a combination of capacitors (C), inductors (L), and resistors (R) to generate a specific oscillator frequency [134].

An oscillator is a crucial component in radar hardware and is used to generate RF signals. Different radars house different kinds of oscillators. Some of the classical oscillators used in the radars include oven-controlled crystal oscillators (OCXO) [135], temperature-compensated crystal oscillators (TCXO) [135], voltage-controlled crystal oscillators (VCXO) [135], surface acoustic wave (SAW) oscillators [136], dielectric resonator oscillators (DRO) [137]. Radar oscillator technology also makes use of phase-lock oscillators (PLO) [138] and direct digital synthesisers (DDS) [139] to generate RF signals. In addition to the oscillators used in classical radar devices, a number of oscillators have the potential to substitute the current radar oscillators and radar oscillator technology. These oscillators include a universal time coordinated (UTC) rack [140], hydrogen maser [141], frequency comb-based microwave generator unit (MGU) [142], and optical atomic clock [68]. This section discusses each of the oscillators in detail.

4.1.1 Crystal oscillators

A crystal oscillator is an electronic oscillator that uses a crystal as the frequency element [143]. The crystal oscillators use the mechanical vibration of the crystals to generate electric signals through the piezoelectric effect. The piezoelectric effect is a reversible process where a mechanical strain generates an electrical charge and vice versa. The most common piezoelectric material used in crystal oscillators is quartz. The oscillation is maintained in a crystal oscillator by taking the voltage signal out of the piezoelectric crystal resonator, amplifying it and feeding it back to the resonator. The resonant frequency of the crystal oscillator is the crystal's rate of expansion and contraction and is primarily dependent on the size and cut of the crystal. The output frequency of a crystal oscillator is either the fundamental resonance frequency or a multiple of the fundamental resonance frequency, also known as overtone frequency. Crystal oscillators are the primary examples of constant-frequency oscillators, with stability and accuracy being the crucial factors. A mechanically vibrating crystal is equivalent to an electrical circuit consisting of R, L and C.

Crystal oscillators can be synthesised with a wide range of standard resonance frequencies between 10 kHz to 100 MHz. The stability of crystal oscillators is a few parts per million (ppm) higher than less stable electronic oscillators made of R, L and C. The crystal oscillators also have better temperature stability and quality factor. The quality factor (Q factor) is an indicator of the frequency stability of a crystal. It is the ratio between the energy stored in a crystal and the sum of all energy losses.

A crystal oscillator's resonant frequency depends on environmental factors, including humidity, pressure, vibration, and temperature. There are different oscillator designs to reduce the effects of the environment, including OCXO and TCXO. In addition to generating a stable signal, the crystal oscillators are also used as frequency references for PLOs.

4.1.1.1 OCXO

Figure 4.1: Image of an OCXO from Axtal [144]

The OCXOs are a subset of crystal oscillators where the crystal is enclosed inside a temperature-controlled chamber called an oven which is kept at a constant temperature. An image of an OCXO from Axtal is shown in figure 4.1. OCXOs can provide very high levels of temperature stability to the crystals. The temperature stability and hence the frequency stability in the OCXO is realised by placing the crystal in a thermally insulated container consisting of a thermostatically controlled oven. The crystal is heated using the oven and maintained at a temperature higher than the typical temperatures encountered by the crystal. The crystal oven typically runs at temperatures around 75°C. Maintaining the crystal oscillators at a constant value provides higher frequency stability to the OCXOs. The degree of frequency fluctuations also depends on how the crystal is cut. The frequency fluctuations within the OCXOs are typically in the range of ± 0.005 ppm for an operating temperature range of -40°C to 85°C. The OCXOs have the highest frequency stability within crystal oscillators with a Q factor of a few parts in 10^6.

4.1.1.2 TCXO

The TCXOs are another subset of crystal oscillators where a temperature-sensitive correction voltage is applied to compensate for the temperature-dependent frequency changes [135]. TCXOs are used when high-frequency stability within a variant environmental temperature is required. The frequency accuracy of an oscillator varies with the temperature, with maximum accuracy generally at an ambient temperature of around 25°C. A typical crystal oscillator can undergo a maximum frequency deviation of about ±100 ppm from its central frequency at extreme environmental temperature conditions. The TCXOs generally constrain the frequency fluctuations within ±0.5 ppm for the entire operating temperature that ranges from -20°C to 85°C.

4.1.1.3 VCXO

The VCXOs are a subset of crystal oscillators where the frequency is controlled by applying a voltage across a varactor diode [135]. The voltage control using a varactor and associated circuitry can be achieved in a general crystal oscillator, a TCXO (giving a TC/VCXO - temperature compensated voltage controlled crystal oscillator) or an OCXO (giving an OC/VCXO - oven controlled voltage controlled crystal oscillator). The varying voltage signal applied to the input terminal of VCXO to change the frequency is known as control voltage. The control voltage is also known as the modulation voltage when the input signal is alternating. The change in the control voltage can either increase or decrease the frequency of the crystal and is dependent on the transfer function of the crystal. The transfer function of a crystal is the direction of frequency change with respect to the control voltage.

4.1.2 SAW oscillators

SAW oscillators are used in several applications, including radars and communications. The SAW oscillators consist of a substrate, an input transducer, and an output transducer [145]. The substrates are typically piezoelectric materials that can propagate mechanical vibrations as surface acoustic waves. The transducers are metallic inter-digital transducers that function as electrodes on the SAW substrate. When the transducers are fed with an alternating signal, an alternating electric field is generated within the piezoelectric substrate material, inducing mechanical stress. The mechanical stress generates vibrations that propagate as surface acoustic waves at the interface of the transducers and the substrate. The input transducer converts the electrical signal to acoustic waves, and the output transducer converts the acoustic waves back to the electric signal. The transducer pattern determines the centre frequency and the bandwidth of the SAW oscillators. The SAW oscillators are used in applications where small oscillators with high Q factor, typically in the frequency range of 200 to 1200 MHz, are required.

4.1.3 Dielectric resonator oscillators

Dielectric resonator oscillators (DRO) are widely used in electronic warfare, communications, and radar applications. A DRO consists of a hollow dielectric element that exhibits resonance behaviour when excited by an electromagnetic field [146]. In order to guarantee that the majority of the electromagnetic fields will be confined within the dielectric medium, DROs are often built using low-loss materials with a high dielectric constant. The physical dimensions, shape (rectangle or disc), and dielectric constant of the dielectric material used affect the resonance frequency of a DRO. The DROs are used in millimetre-wave applications that require very high signal stability and high-quality factor. The frequency stability of the DROs is around ± 4 ppm for every degree change in the temperature.

4.1.4 Direct digital synthesizers

Recent advances in digital technology resulted in the implementation of direct digital synthesis of signal sources. The DDS is used in various applications within radars and communications. Direct digital synthesis is a technique for generating RF signals with significant control over the signal's frequency, phase, and amplitude. Unlike other analogue radar oscillator technologies, the DDS generates waveforms digitally. The DDS can also filter the signals to remove unwanted components and multiply the signal to higher frequencies. The DDS can apply amplitude, frequency, and phase modulation to the generated signals through software, providing flexibility when complex and accurate waveforms are needed. The output of the DDS is generally in the range of a few Hz to a few MHz. The DDS output can be frequency multiplied or used as reference oscillators in PLLs to generate RF signals at frequencies of UHF and above [147]. An analogue reference signal is used in DDS to provide an invariant sampling interval, from which a series of signal amplitudes is calculated and output as digital codes. A DAC receives the digital signal and filters the output to create an analogue signal at the desired frequency. Due to DAC faults and numerical truncation, the DDS also emits more spurious emissions than its analogue counterparts.

4.1.5 Phase-locked oscillators

Phase-locked oscillators are used in applications where both short-term and long-term frequency stability are required. A typical PLO consists of a PLL and a reference oscillator. The reference oscillator used in PLO has a very high short-term stability and Q factor. The VCO inside the PLL has high long-term stability. A typical PLO architecture includes TCXO or OCXO as a reference oscillator to the PLL with a VCO, such as a dielectric resonator oscillator. The PLO architecture is less complex than the DDS architecture and provides fewer spurious signals. The PLO architecture also gives the advantage of low phase noise for

both frequencies close to the carrier and far from the carrier by phase-locking the reference oscillator to the VCO.

4.1.6 UTC Rack

Universal time coordinated rack is a multipurpose rack consisting of three caesium standard-based oscillators from microchip (5071A) referenced to each other. The caesium oscillators consisting of caesium beam tubes act as primary frequency standards and can maintain accuracy and stability. The caesium beam tube mainly consists of a caesium oven, vacuum tube, microwave cavity, magnets, and detector [148]. The ^{133}Cs atoms heated by the oven reach the vacuum tube. The microwave cavity consists of microwave frequency from a quartz oscillator. The magnetic energy state changes for caesium atoms whose resonance frequency matches the frequency of the microwave cavity. The magnets serve the purpose of a gate to allow atoms with the microwave frequency of the cavity to get detected at the detector. The UTC rack is also referenced with the global positioning system (GPS)

Figure 4.2: Image of a UTC Rack from Chronos technology [140]

to verify the accuracy of the caesium oscillators. An image of a UTC rack from Chronos

technology is given in figure 4.2. The oscillator accounts for environmental factors that might significantly affect the long-term stability of a caesium standard. Digital electronics are used to continuously monitor and optimise the performance of the caesium oscillator in the UTC rack to the environmental changes. The caesium beam tube-based caesium oscillators have a Q factor of about a few parts in 10^8 [149]. The caesium oscillator-based UTC rack has applications in telecommunications, satellite communications, and navigation systems. The RF outputs of the UTC rack provide the UTC rack with the potential to be used as oscillators in radars.

4.1.7 Hydrogen Maser

Figure 4.3: Image of an active hydrogen maser from T4 Science [150]

The word MASER stands for microwave amplification by stimulated emission of radiation. An image of a hydrogen maser from T4 Science is given in figure 4.3. Hydrogen masers are frequency standards that operate at the resonance frequency of hydrogen atoms. In a hydrogen maser [148], the hydrogen gas reaches a storage bulb through a magnetic gate that allows only a certain magnetic energy state to pass through. The atoms inside the bulb drop to lower energy levels releasing photons of microwave frequency, initiating stimulated

emission of photons from other atoms. A tuned resonant cavity around the bulb redirects the atoms back into the system to support the stimulated emission. The phenomenon generates a microwave frequency locked to the resonance frequency of the hydrogen atom. The hydrogen maser is one of the well-defined frequency standards and has a Q factor of about a few parts in 10^9 [149]. The hydrogen maser oscillators are used in applications including time-keeping, radio astronomy, and global navigation satellite system (GNSS). The RF outputs of the hydrogen maser oscillator, derived from the stable resonance frequency of hydrogen atoms, have the potential to be used as oscillators in radars.

4.1.8 Microwave generator unit

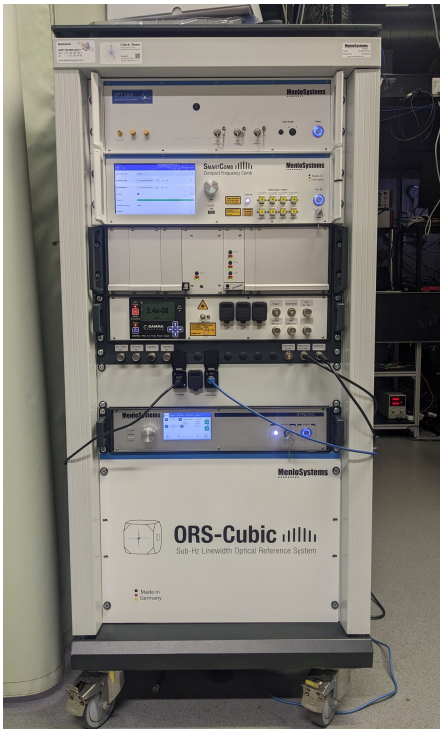

Figure 4.4: Image of an MGU from Menlo Systems [151]

The microwave generator unit is a comprehensive device capable of generating signals in the microwave domain by phase-coherent division of high-fidelity optical signals using the frequency comb technology. An MGU consists of a frequency comb to down-convert the

optical signals and an ultra-stable optical system acting as a reference for the frequency comb. The frequency comb can also be referenced by an external optical signal. The frequency comb is a pulsed mode-locked laser that produces evenly spaced frequency outputs in the frequency domain. Mode locking is a technique for generating a pulsed laser in the order of picosecond or femtosecond. The evenly spaced frequency outputs, known as 'teeth', are spaced by the pulsed laser's repetition rate frequency (f_{rep}). The frequency of each tooth is equivalent to the tooth number (mode number) multiplied by the spacing between the teeth. The change in the pulse-to-pulse phase of the laser introduces another parameter called the carrier-envelope offset frequency (f_{ceo}). An image of an MGU from Menlo Systems is given in figure 4.4.

The MGU can generate frequencies in both the optical and RF domain. The RF signals generated by the MGU have low phase noise characteristics due to the conversion of optical signals to RF. The MGU also has the potential to lock to an optical atomic reference and to translate the ultra-high precision and stability of an optical atomic clock in the RF domain. The MGU is used in applications including deep space navigation, precision metrology, telecommunications and next-generation wireless communications. The low phase noise RF outputs make the MGU a potential candidate for realising quantum oscillators in radars. Whilst an MGU-generated RF source locked to an optical atomic clock will be the ultimate realisation of a quantum oscillator for radar applications, the RF signal generated from the MGU locked to its cavity-stabilised internal laser is referred to as one manifestation of quantum oscillators in the thesis.

4.1.9 Optical atomic clock

Atomic clocks can be subdivided into two categories based on frequency: microwave and optical. Optical atomic clocks are oscillators with the highest level of frequency stability.

There are two primary categories of optical clocks: the first uses one or more trapped ions, second uses a large number of neutral atoms in a lattice of light with a 'magic' wavelength. An optical atomic clock mainly consists of a local oscillator and an atomic reference. The local oscillator provides the optical frequency that will be disciplined to the atomic reference. A carefully produced sample of atoms or a single ion typically has some "forbidden" electronic transition that serves as the atomic reference [152]. Electronic transitions that are prohibited under the electric dipole approximation are known as forbidden transitions. The forbidden transition can be made possible by applying an external magnetic field. These forbidden transitions have very narrow linewidth making them a useful well-defined frequency reference. By tuning the frequency of the local oscillator (laser) to the optical atomic resonance frequency, the optical clock is referenced to the atomic transition. The highest frequency stability of the optical atomic clocks is attributed to the narrow linewidth of the transition. The RF output of an MGU locked to an optical atomic clock is another potential candidate for realising quantum oscillators in radars. The Q factor of crucial oscillators discussed in the section is summarised in the table 4.1.

Oscillator	Q factor
OCXO	10^6
UTC Rack	10^8
Hydrogen Maser	10^9
Optical atomic clock	10^{14}

Table 4.1: Q factor of different oscillators

4.1.10 Oscillators in the University of Birmingham laboratory

In this subsection, the oscillators available in the laboratory for the figure of merit measurements are summarised. The Alkaline group laboratory at the University of Birmingham houses a wide variety of oscillators, from standard OCXOs to optical atomic clocks, with most of the oscillators having the potential to replace the current oscillators used in the

radars. The two OCXOs in the laboratory include an OCXO from Axtal (AXIOM70LN-21) [144] and an OCXO from Vectron (0X-200-0165-62M500000) [153]. Both the OCXOs are standard crystal oscillators used in different types of radars. The oscillators in the laboratory also include a highly stable hydrogen maser from T4 Science (iMaser 3000) [150] and UTC rack from Chronos technology [140]. Both high-performing oscillators have RF frequency outputs and have the potential to be used as radar oscillators. The MGU from Menlo Systems (PMWG-1500) is a crucial device capable of providing very high stable frequencies in both the optical and RF domains. The optical atomic lattice clock currently being built is based on strontium. Quantum oscillators like MGU, when referenced with the optical lattice clock, have the potential to provide ultra-high precision and accuracy of the atom-referenced optical signal to radars. The MGU, currently referenced to a laser housed inside the MGU, also has the potential to replace the current oscillators in radars. The different oscillators available in the laboratory and their output frequencies are summarised in table 4.2.

Oscillator	Outputs
Axtal OCXO	10 MHz
Vectron OCXO	62.5 MHz
UTC Rack	{1, 10, 100} MHz
Hydrogen Maser	{5, 10, 100} MHz
	{10, 62.5} MHz
MGU	{1.25, 5, 10} GHz
	1542 nm
Strontium lattice clock	698 nm

Table 4.2: Different oscillators in the laboratory and their outputs (frequency/wavelength)

4.2 Figure of Merits

A figure of merit is defined as a quantity representing a device's efficiency or performance. The efficiency and performance of an oscillator are generally represented in terms of its stability. Modern navigation and tracking devices, including radars, require extremely

stable primary oscillators [154]. The performance of an oscillator is generally specified in terms of its frequency and phase stability. The two significant figures of merit used to quantify the oscillator performance are Allan deviation and phase noise [91].

4.2.1 Allan Deviation

Allan deviation measures the frequency stability of an oscillator in the time domain [91], one of the crucial parameters that define the performance of an oscillator. The basic standard deviation techniques cannot fully characterise the frequency stability of an oscillator since the standard deviation does not converge for a few types of noises [155]. Also, the standard deviation climbs logarithmic with the number of samples. A modified variance, known as Allan variance, can converge all types of noises [156] and is used in characterising the frequency stability of oscillators. Allan deviation, also known as sigma-tau, is the square root of Allan variance. Allan variance is developed from the deviation of the measured frequency of an oscillator from its nominal frequency. For an oscillator with a measured frequency of f and nominal frequency of f_0, the normalised frequency deviation is given by,

$$y(t) = \frac{f(t) - f_0}{f_0}. \tag{4.1}$$

The Allan variance analyses the derivative of the normalised frequency deviation. Averaging is performed to accommodate different time scales in measuring the derivative of the normalised frequency deviation. The average value of $y(t)$ over a sampling interval of τ is given by,

$$\bar{y}(t) = \frac{1}{\tau} \int_t^{t+\tau} y(t')\, dt', \tag{4.2}$$

where $y(t')$ is the time derivative of $y(t)$. The Allan variance is determined by taking N measurements of the oscillator frequency at a regular interval of period T, with no dead time

between the measurements. The Allan variance is defined as [157],

$$\sigma_y^2(N,T,\tau) = \frac{1}{N-1}\sum_{n=1}^{N}\left\{\bar{y}(t+nT) - \frac{1}{N}\sum_{k=1}^{N}\bar{y}(t+kT)\right\}^2. \tag{4.3}$$

Similar to the representation of different power law components in the phase noise spectrum in figure 2.8 and the equation 2.21, different kinds of noises in a typical oscillator can be generally characterised using the power law spectrum as [157],

$$S_y(f) = h|f|^{\alpha}, \tag{4.4}$$

where y is the normalised frequency deviation as given in equation 4.1, h is the amplitude of the noise process, f is the frequency, and α is the power law factor for each power law component and is constant over some range of f. The expectation value of the Allan variance is proportional to the sampling interval and is given by,

$$\mathbb{E}[\sigma_y^2(N,T,\tau)] \propto \tau^{\mu}, \tag{4.5}$$

where the function $\mathbb{E}[\sigma_y^2(N,T,\tau)]$ represents the expectation value of the Allan variance. The factor μ in the equation 4.5 is related to α in the equation 4.4 as [157],

$$\mu = \begin{cases} -2 & \text{if } \alpha \geq 1, \\ -\alpha - 1 & \text{if } -3 < \alpha \leq 1, \\ \text{undefined} & \text{otherwise.} \end{cases} \tag{4.6}$$

The frequency spectrum's power law component and the noise type are summarised in the table 4.3. The power law factor (α) for each power-law component of the frequency spectrum given in table 4.3 is related to the power law factor (β) for each power-law com-

ponent of the phase noise spectrum given in the table 2.2. The relation between α and β is,

$$\beta = \alpha - 2. \tag{4.7}$$

The relationship between μ and α provides a good insight into the performance of an

Term	Type of noise
$1/f^2$	Random walk frequency modulation
$1/f^1$	Flicker frequency modulation
f^0	White frequency modulation
f^1	Flicker phase modulation
f^2	White phase modulation

Table 4.3: The noise type associated with different power law components of the frequency spectrum

oscillator. Since μ is also equal to the slope of the Allan variance plot in the log scale, information on the types of noises dominant at different time scales can be obtained.

The Allan deviation is the square root of the Allan variance. For N measurements of the oscillator frequency with a time period of T and sampling interval of τ, the Allan deviation is given by,

$$\sigma_y(N,T,\tau) = \sqrt{\frac{1}{N-1}\sum_{n=1}^{N}\left\{\bar{y}(t+nT) - \frac{1}{N}\sum_{k=1}^{N}\bar{y}(t+kT)\right\}^2}. \tag{4.8}$$

Allan deviation inherently provides a measure of the variation of the measured frequency from a nominal frequency averaged over different periods. Allan variance and hence the Allan deviation are both functions of the sampling interval. Different noise types have different scaling of Allan variance and Allan deviation with τ. The scaling depends on the term μ, and μ is related to α, as discussed in the equation 4.6. The table 4.4 summarises the power law frequency components, Allan variance and the Allan deviation components for different types of noise in a typical oscillator.

Type of noise	Component		
	power law	Allan variance	Allan deviation
Random walk frequency modulation	f^{-2}	τ^{1}	$\tau^{1/2}$
Flicker frequency modulation	f^{-1}	τ^{0}	τ^{0}
White frequency modulation	f^{0}	τ^{-1}	$\tau^{-1/2}$
Flicker phase modulation	f^{1}	τ^{-2}	τ^{-1}
White phase modulation	f^{2}	τ^{-2}	τ^{-1}

Table 4.4: Allan variance and Allan deviation response to different types of noises and its respective power law components

In table 4.4, we can see that the Allan deviation and Allan variance response for both the white phase modulation and Flicker phase modulation are identical and hence cannot be separated. Allan deviation plot is generally plotted with Allan deviation in the y-axis and the averaging time in the x-axis. The sampling interval is denoted as averaging time in the Allan deviation plot. A general Allan deviation plot of a typical oscillator with different noise components is given in figure 4.5. There are different methods to measure the Allan deviation of different oscillators, and they are discussed in detail in section 4.3.

4.2.2 Phase Noise

The stability of an oscillator in the frequency domain is another crucial parameter that defines the performance of an oscillator. Phase noise is the measure of the stability of an oscillator in the frequency domain [49]. Phase noise is the frequency domain representation of the fluctuations in the phase of an oscillator output. In the frequency domain, the phase fluctuations are converted into noise sidebands around the carrier frequency. Detailed analysis of the derivation of phase noise and the phase noise of a typical oscillator are given in section 2.3.3. There are different methods to measure the phase noise of different oscillators, and they are discussed in detail in section 4.4.

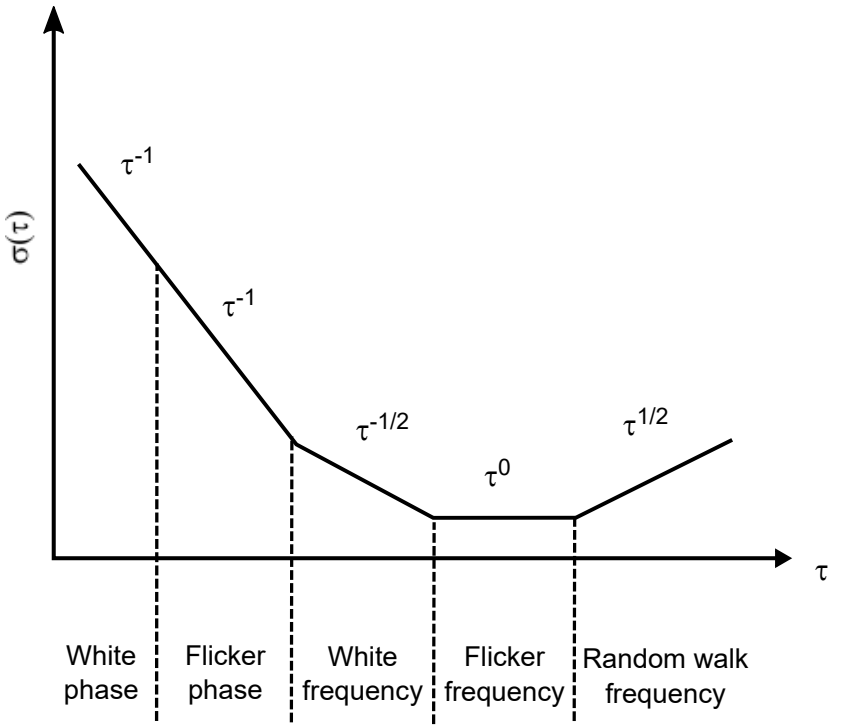

Figure 4.5: The general Allan deviation of an oscillator with different noise components [158].

4.3 Allan deviation measurements

In this section, the different methods for Allan deviation measurements and the measurement results are discussed in detail. As discussed in section 4.2.1, Allan deviation is one of the crucial figures of merit used to assess the frequency stability of the oscillators in the time domain. The measurement campaign includes the measurement of different oscillators consisting of oscillators used in current radars and the oscillators that have the potential to be used in the radars. The Allan deviation of most of the oscillators available in the laboratory given in table 4.2 was measured.

4.3.1 Measurement methods

There are different methods to measure the Allan deviation of oscillators. Since Allan deviation is the frequency stability in the time domain, one common factor is the measurement of the frequency of the oscillator in the time domain. The frequency of the oscillators in the time domain was recorded using frequency counters. The frequency counters generally have a reference frequency input, typically at 10 MHz and a number of inputs for counting the frequency of the device under test (DUT). Two frequency counters were available for counting the frequency of the oscillators. The former counter has two inputs for frequency counting, a measurement frequency range of 10 Hz to 350 MHz, with 12 digits/s and a resolution of 20 ps. The latter has four inputs for frequency counting, a measurement frequency range of 4 kHz to 130 MHz, with 13 digits/s and a resolution of 12.2 ps. The frequency values were converted to Allan deviation using stable32 software. In all the frequency counting measurements, the gate time of the frequency counter was set to 1 s.

The Allan deviation measurements can be broadly divided into four methods. In the first method, the output of the DUT is directly fed to the frequency counter. In the second method, the output of the DUT is mixed and down-converted, and the beat note is fed into the frequency counter. The third method is specific to the Allan deviation of the optical output of the MGU, where the f_{rep}, f_{ceo} and the beat frequency (f_{beat}) of the comb are fed into the frequency counter simultaneously. In all three methods, since we always use a reference oscillator in the frequency counting, the Allan deviation will be relative to the reference oscillator. In the fourth method, a three-cornered hat setup is used to independently measure the Allan deviation of three constituent oscillators.

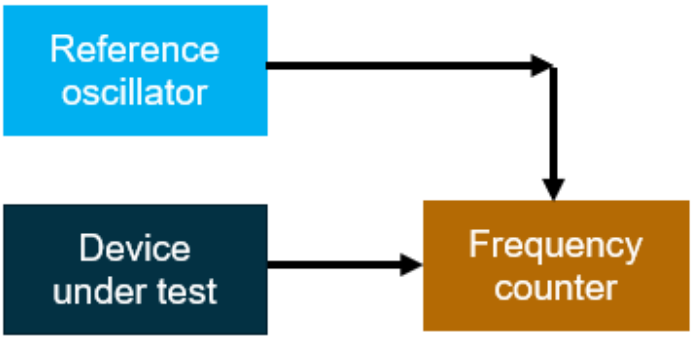

Figure 4.6: An illustration of method 1 for the measurement of Allan deviation showing the output of the DUT directly connected to the frequency counter. The reference oscillator is used to reference the frequency counter.

4.3.1.1 Method 1

In the first method, the frequency of the DUT is directly counted using the frequency counter. An illustration of the method is given in figure 4.6. Since the measurement also consists of a reference oscillator at 10 MHz, the Allan deviation obtained will be a relative Allan deviation between the DUT and the reference oscillator. The method is also limited by the frequency counter's measurement range, typically up to 100s of MHz.

4.3.1.2 Method 2

The second method is an improvisation of the first method in cases where the oscillator frequency is outside the measurement frequency range of the frequency counter. The method is also used for frequency counting where higher resolution is required. In the second method, as illustrated in figure 4.7, the output of the DUT is mixed, down-converted and filtered to a frequency lower than the oscillator frequency. The DUT output is mixed with the output of a frequency synthesiser. The frequency synthesiser and the frequency counter are referenced to the same reference oscillator. The beat frequency is fed to the frequency counter.

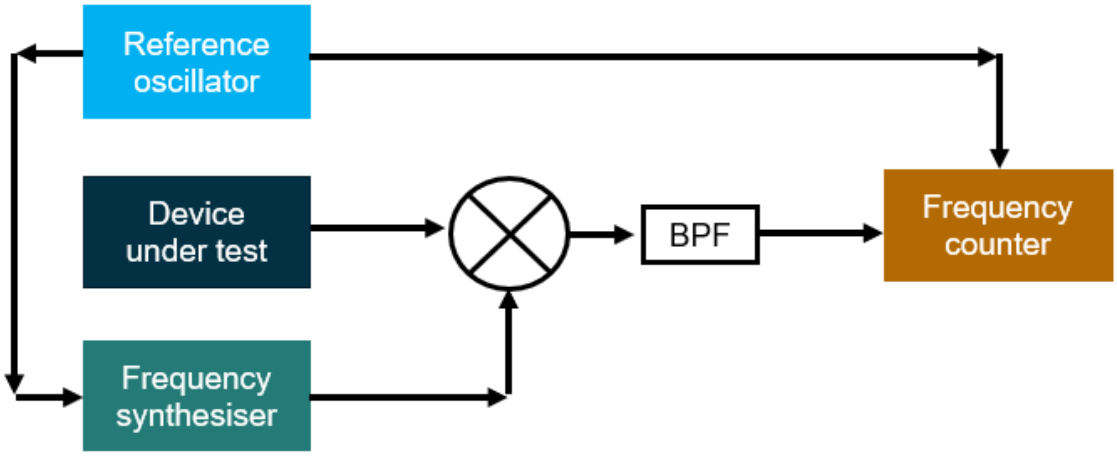

Figure 4.7: An illustration of method 2 for the measurement of Allan deviation showing the output of the DUT mixed with the output from the frequency synthesiser. The mixer output is filtered and fed into the frequency counter. The reference oscillator is used to reference both the frequency counter and the frequency synthesiser.

4.3.1.3 Method 3

The third method is a specific method used to measure the Allan deviation of the internal laser of the MGU. The MGU has an internal laser at 1542 nm, and all the frequencies are derived from the internal laser using the frequency comb. The optical frequency (f_{opt}) of the internal laser can be calculated using f_{rep}, f_{ceo}, and f_{beat} between the laser and the nearest comb tooth as,

$$f_{opt} = f_{rep} + f_{ceo} + n f_{beat}, \tag{4.9}$$

where n is the mode of the frequency comb. In the third method, as illustrated in figure 4.8, the 19^{th} harmonic of the repetition rate of the frequency comb of the MGU is mixed, downconverted, filtered, and amplified before feeding to the frequency counter. Similar to method two discussed in 4.3.1.2, the DUT (MGU in this case) is mixed using the output of the frequency synthesiser. The frequency synthesiser and the frequency counter are referenced to the same reference oscillator. Along with measuring the beat of the repetition rate, the f_{ceo} and f_{beat} are simultaneously measured using the frequency counter. The equivalent optical

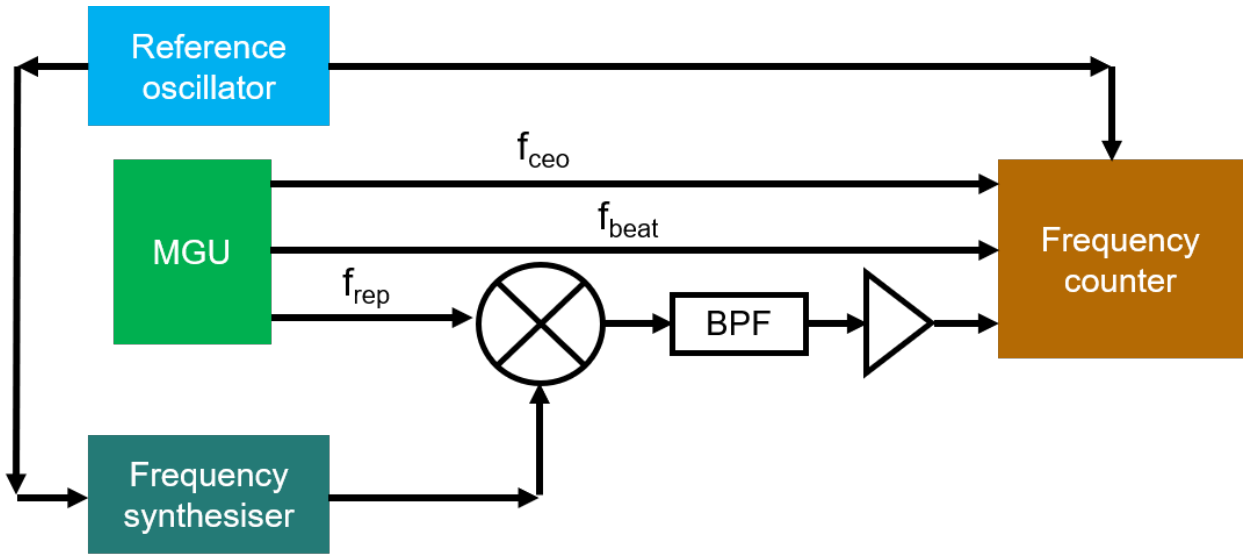

Figure 4.8: An illustration of method 3 for the measurement of Allan deviation showing the f_{rep} of the MGU mixed with the output from the frequency synthesiser. The mixer output is filtered and fed into the frequency counter. Along with the mixer output, the f_{ceo} and f_{beat} are also simultaneously counted using the frequency counter. The reference oscillator is used to reference both the frequency counter and the frequency synthesiser.

frequency is derived from the equation 4.9.

4.3.1.4 Method 4

All the Allan deviation measurements performed using the first three methods effectively provide the relative Allan deviation between the reference oscillator and the oscillator under test. The three-cornered hat, as illustrated in figure 4.9, is the most comprehensive method for the measurement of Allan deviation, where we count the frequencies of three DUTs simultaneously. The three-cornered hat method can be used to measure the phase noise of any oscillators, including the oscillators where the methods mentioned above were used. The three-cornered hat is ultimately limited by the worst among the three oscillators; hence oscillators with similar performance are usually compared. Since there are three pairs of measurements for three DUTs with similar performance, the individual Allan deviation of the three devices can be calculated. The three-cornered hat method can only be used for

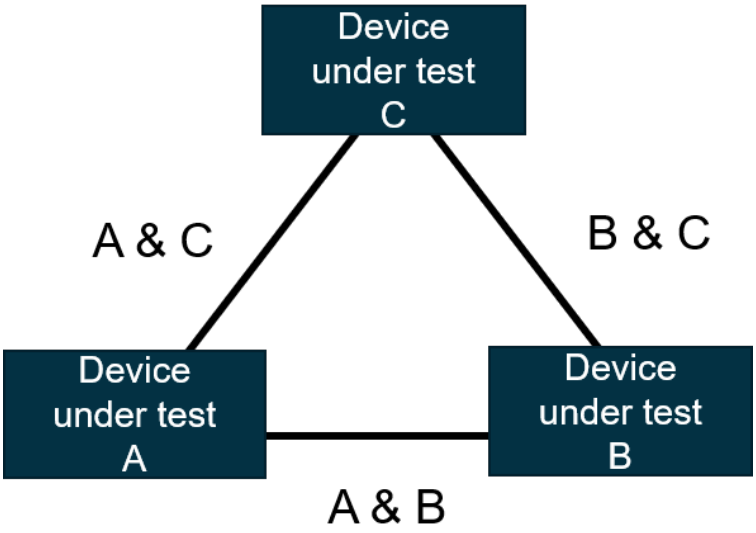

Figure 4.9: An illustration of method 4 for the measurement of Allan deviation showing three DUTs (A, B, and C) at the three corners of a hat. The frequency of the three DUTs is counted simultaneously using a frequency counter.

uncorrelated devices with similar performance.

4.3.2 Results

Allan deviation measurements were carried out for most oscillators in table 4.2. The hydrogen maser was kept as the reference oscillator for all Allan deviation measurements discussed in the thesis. The Allan deviation of the Axtal OCXO, Vectron OCXO and the UTC rack were carried out using method 1 discussed in 4.3.1.1. The Allan deviation of the 1542 nm internal laser of the MGU was performed using method 3 discussed in 4.3.1.3. The table 4.5 summarises the crucial Allan deviation measurements performed to evaluate the frequency stability of the oscillators in the time domain.

The Allan deviation measurements of the oscillators are compared and plotted in figure 4.10. In figure 4.10, we can see that the Allan deviation of the highly stable oscillators is considerably better than the OCXOs. The Axtal OCXO and Vectron OCXO have an

DUT	Reference oscillator	Method
Axtal OCXO	Hydrogen Maser	Method 1
Vectron OCXO	Hydrogen Maser	Method 1
UTC Rack	Hydrogen Maser	Method 1
MGU	Hydrogen Maser	Method 3

Table 4.5: The summary of the crucial Allan deviation measurements performed consisting of the DUT, reference oscillator and the method used.

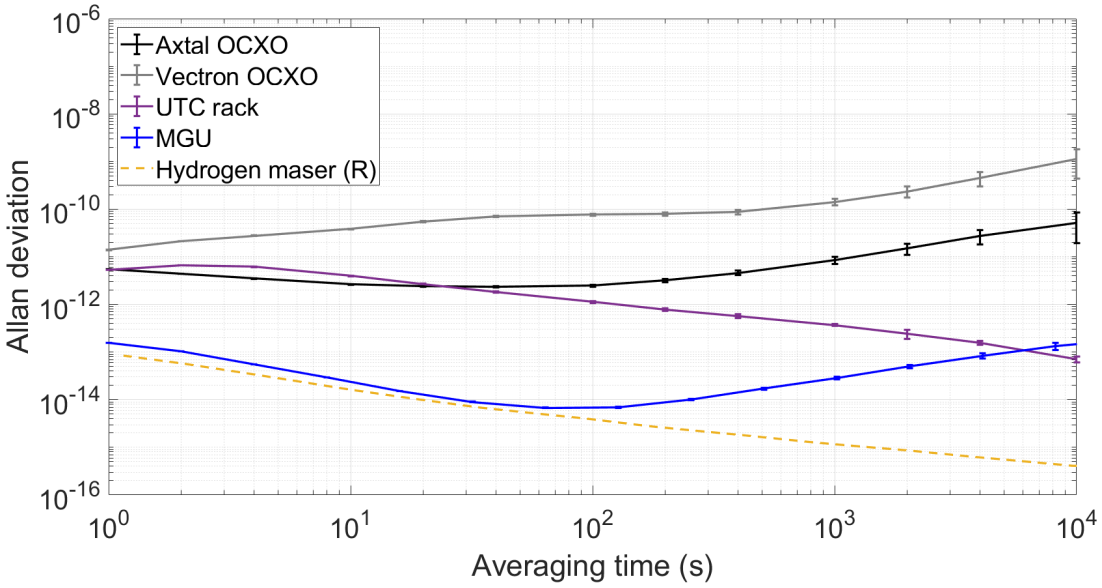

Figure 4.10: Allan deviation measurements of different oscillators in the laboratory along with the Allan deviation reference values of hydrogen maser. The Allan deviation values of the highly stable oscillators, including MGU and hydrogen maser, are considerably better than the OCXOs. At higher averaging times, the Allan deviation of both the OCXOs is getting worse, indicating the limitations in the long-term stability. The Allan deviation of the UTC rack and hydrogen maser is getting better with averaging time, indicating long-term stability. The Allan deviation of MGU is getting worse beyond 100 s, showing the frequency drift of the internal laser of the MGU. The Allan deviation of MGU is limited by the reference oscillator (hydrogen maser) used for frequency counting.

Allan deviation value of around 10^{-11} at 1 s averaging time. At higher averaging times, the Allan deviation of both the OCXOs is getting worse, indicating the limitations in the long-term frequency stability of the OCXOs as expected. The Allan deviation of the UTC rack is also at a value of around 10^{-11} at 1 s averaging time and continuously gets better with the averaging time. The improvement in the Allan deviation value for the UTC rack

with averaging time is expected since the UTC rack has good long-term frequency stability. The Allan deviation of MGU clearly shows a considerable improvement compared to the measured values of the Allan deviation of OCXOs and UTC rack.

The better Allan deviation of the MGU is attributed to the stability of the reference to which the MGU is locked. The MGU is expected to have better Allan deviation values and is currently restricted by the reference oscillator (hydrogen maser) used for the Allan deviation measurement. The reference values for the Allan deviation of the hydrogen maser are also added to the figure 4.10. The limitation of the hydrogen maser in the measurement of the Allan deviation of the MGU is evident in the overlap between the Allan deviation values of MGU and hydrogen maser for an averaging time of up to 100 s. In the current configuration, the internal laser of the MGU also drifts with time. The increase in the Allan deviation values of the MGU beyond 100 s of averaging time depicts the drift in the frequency of the MGU internal laser. The drift in the internal laser of the MGU can be removed by referencing the MGU to an atomic reference having long-term stability, like an optical atomic lattice clock.

Since the optical atomic clocks consist of a forbidden transition (in optical frequency) with narrow linewidth, the optical atomic clocks are expected to have the highest frequency stability and hence better Allan deviation values. The MGU can also provide very low Allan deviation values by locking the MGU to an optical reference (from atomic clocks). The Allan deviation reference values from the measurement of a pair of strontium atomic lattice clocks [65] are shown in figure 4.11. Figure 4.11 also shows the Allan deviation measurement performed in the laboratory by locking the MGU to an internal laser and the Alan deviation reference values from the measurement of a pair of MGU to an optical reference. Figure 4.11 clearly shows that the frequency stability of an optical atomic clock can be translated to the MGU by locking the MGU to an optical reference. Comparing figures 4.10 and 4.11,

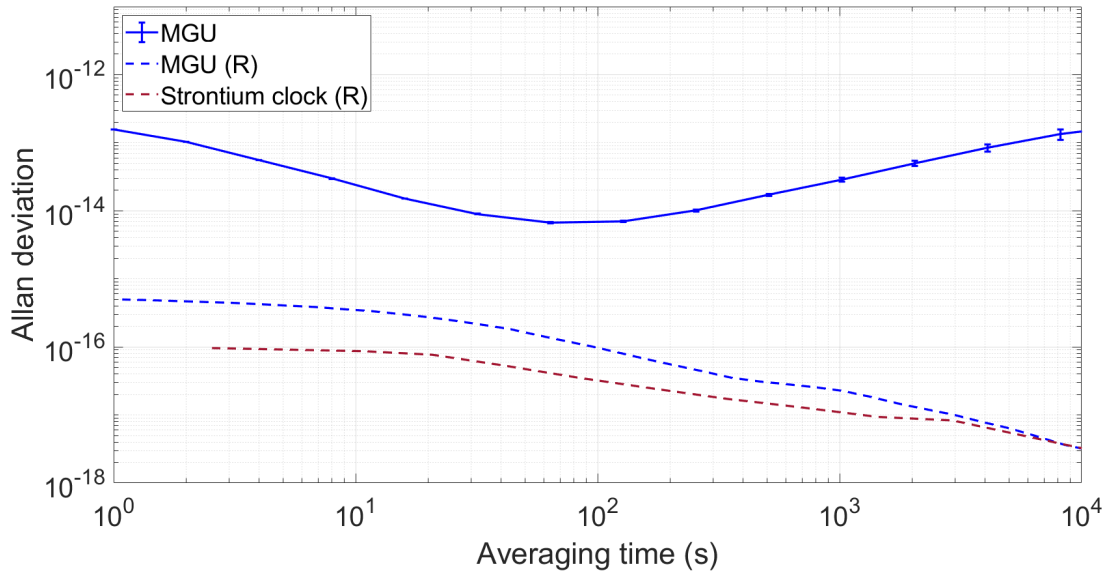

Figure 4.11: Comparison of the laboratory measurement of the Allan deviation of MGU (with hydrogen maser as reference oscillator) with the Allan deviation reference value of a pair of MGU locked to an optical reference and Allan deviation reference value of a pair of strontium atomic lattice clock. Atomic clocks have excellent Allan deviation values. The very high long-term stability of the atomic clocks can be translated to the MGU by locking the MGU to highly stable optical references.

we can see that the MGU, either locked to an optical reference or locked to the internal laser, has very high-frequency stability compared to OCXOs currently used in radars. Also, referencing the MGU with optical reference takes care of the frequency drift in MGU and hence provides very high long-term frequency stability. Hence, replacing the classical radar oscillators with quantum oscillators (like MGU) has the potential to improve the frequency stability in the time domain by a few orders of magnitude.

4.4 Phase Noise measurements

In this section, the different methods for phase noise measurements and the measurement results are discussed in detail. As discussed in section 4.2.2, phase noise is a crucial figure of merit that represents the stability of an oscillator in the frequency domain. The

measurement campaign includes the measurement of the phase noise of different oscillators at different output frequencies. The phase noise of an oscillator at different offset frequencies from the carrier depends on the carrier frequency itself, with a general rule of thumb that the phase noise increases with the carrier frequency. The phase noise of different oscillators used in current radars and oscillators that have the potential to be used in radars were measured. In addition to the measurement of the phase noise of different oscillators available in the laboratory in table 4.2, the phase noise at the transmit frequency of the staring radar system is also discussed.

4.4.1 Measurement methods

The phase noise can be measured through different methods. All the measurement methods discussed in the thesis consist of a phase noise analyser (PNA) to directly generate the phase noise spectrum of the signal at the input of the PNA. The PNA has a measurement frequency range of 1 MHz to 26.5 GHz. The PNA was set to measure the phase noise at frequency offsets between 1 Hz and 10 kHz. The increase in cross-correlations reduces the level of uncorrelated noise in the phase noise measurement. The value of cross-correlation needed in the PNA also depends on the DUT. Better the phase noise performance of the DUT, the higher the cross-correlation factor required. The cross-correlation factor was usually set at 1000.

The phase noise measurement methods can be broadly divided into three methods. In the first method, the output of the DUT is directly connected to the input of the PNA. In the second method, the beat between the optical signals from the DUT and the MGU is used to lock the MGU. The RF output of the MGU is then fed into the PNA. The third method is used to directly measure the phase noise of optical frequencies, where the beat note between the DUT and reference oscillator is fed into the PNA.

4.4.1.1 Method 1

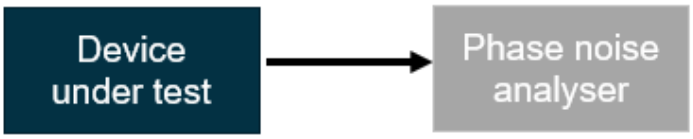

Figure 4.12: An illustration of method 1 for the measurement of phase noise showing the output of the DUT directly connected to the phase noise analyser.

In the first method, as illustrated in figure 4.12, the output of the DUT is directly fed into the PNA. The method can measure the phase noise of any oscillators at frequencies ranging between 1 MHz and 26.5 GHz, limited by the frequency span of the PNA.

4.4.1.2 Method 2

In the second method, as illustrated in figure 4.13, the optical frequency at the outputs of the DUT and MGU is fed into a beat detection unit (BDU) setup. The output of the photodiode consists of an RF signal equivalent to the beat between the DUT and the MGU. The RF signal at the output of the photodiode is used to lock the MGU. The locked MGU can generate RF signals that can be fed to the PNA. For the method to work, both optical frequencies should be comparable.

4.4.1.3 Method 3

The third method is used to measure the phase noise of optical signals. As illustrated in figure 4.14, the method consists of a DUT and a reference oscillator, both at comparable optical frequencies. A photodiode setup generates the beat note between the two optical

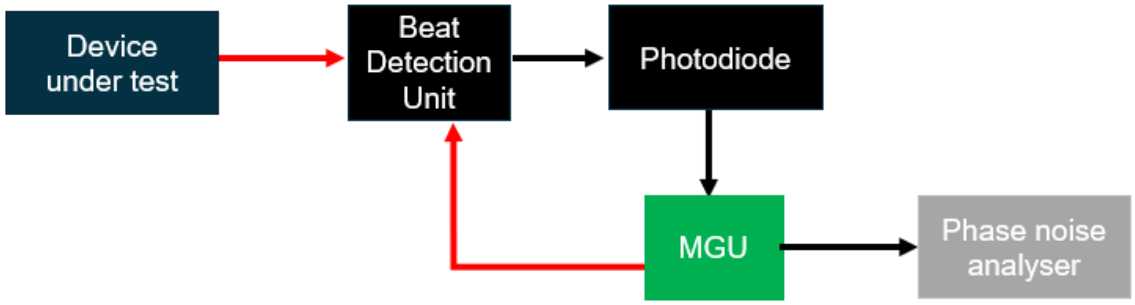

Figure 4.13: An illustration of method 2 for the measurement of phase noise showing the optical outputs from the DUT and MGU fed into the beat detection unit. The RF output from the beat detection unit is used to lock the MGU. The RF output from the MGU is connected to the phase noise analyser.

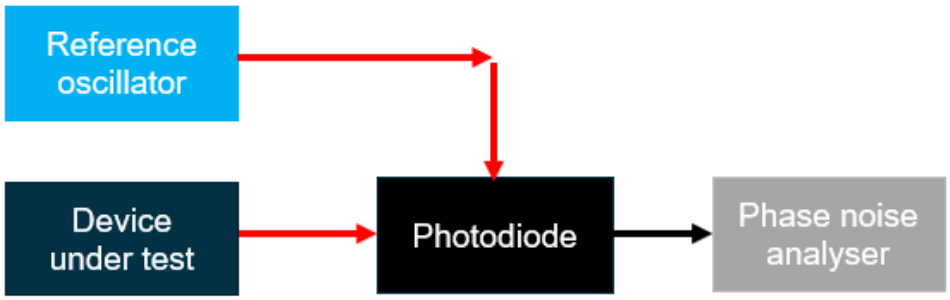

Figure 4.14: An illustration of method 3 for the measurement of phase noise showing the optical outputs from the DUT and reference oscillator beat using a photodiode. The RF beat note at the output of the photodiode is directly connected to the phase noise analyser.

frequencies. The beat note generated will be at RF frequencies compatible with the PNA. The output of the photodiode is directly connected to the PNA.

4.4.2 Results

The phase noise measurements were carried out for most of the carrier frequencies for the oscillators given in table 4.2. All the phase noise measurements in the thesis fol-

lowed method 1, discussed in 4.4.1.1. Table 4.6 summarises the phase noise measurements performed for evaluating the frequency stability of the oscillators in the frequency domain.

Oscillator	Carrier frequency			
	10 MHz	62.5 MHz	1.25 GHz	10 GHz
Axtal OCXO	✓			
Vectron OCXO		✓		
UTC Rack	✓			
Hydrogen maser	✓			
MGU	✓	✓	✓	✓

Table 4.6: The summary of the phase noise measurements performed on different oscillators and the respective carrier frequencies

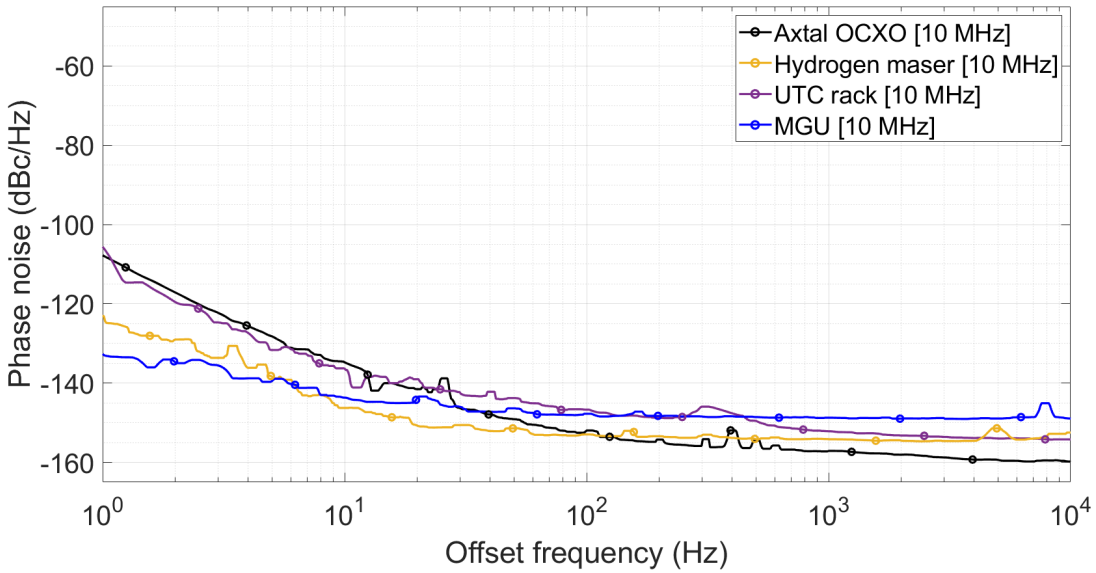

Figure 4.15: Phase noise spectrum of different oscillators in the laboratory at 10 MHz carrier frequency. At lower offset frequencies, the phase noise of Axtal OCXO and UTC rack is comparatively higher than hydrogen maser and MGU. Beyond the 100 Hz frequency offset, the phase noise of Axtal OCXO is relatively better.

The phase noise spectrum in figure 4.15 shows the phase noise of all the oscillators at 10 MHz carrier frequency. In figure 4.15, we can see that at lower offset frequencies from the carrier, up to about 30 Hz, the phase noise of both the UTC rack and the Axtal OCXO is higher than the phase noise of the MGU and hydrogen maser. Between the MGU and hydrogen maser, the phase noise of the hydrogen maser is better for all offset frequencies

above 10 Hz. In figure 4.15, we can also see that the phase noise of the Axtal OCXO is better than other oscillators beyond the offset frequency of 100 Hz. The phase noise spectrum produced by the PNA automatically undergoes smoothing. Since the phase noise values are very low, the PNA is configured at a high cross-correlation factor to ensure the measurement is not limited by the PNA noise floor.

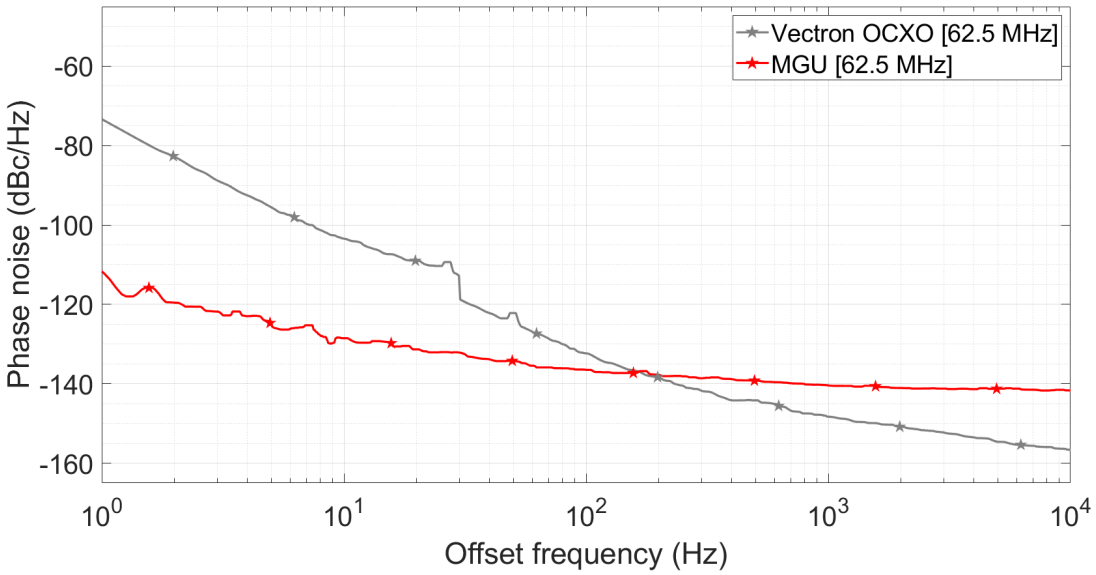

Figure 4.16: Phase noise spectrum of Vectron OCXO and MGU at 62.5 MHz carrier frequency. At lower offset frequencies, the phase noise of MGU is better than Vectron OCXO. Beyond 100 Hz, the phase noise of the Vectron OCXO is relatively better.

The phase noise spectrum in figure 4.16 shows the phase noise spectrum of both MGU and Vectron OCXO at 62.5 MHz. In figure 4.16, we can see that the phase noise of the MGU is relatively very low compared to Vectron OCXO for frequency offsets up to 100 Hz. Beyond 100 Hz, the Vectron OCXO phase noise is below the phase noise of the MGU. The phase noise spectrum of Vectron OCXO also shows a sudden jump at 30 Hz. The jump was the effect of an unwanted peak in the phase noise spectrum at 30 Hz due to external interference in the lab, but the effect was reduced after the smoothing function within the phase noise analyser resulting in the jump.

The phase noise spectrum in figure 4.17 shows the phase noise of the output of the

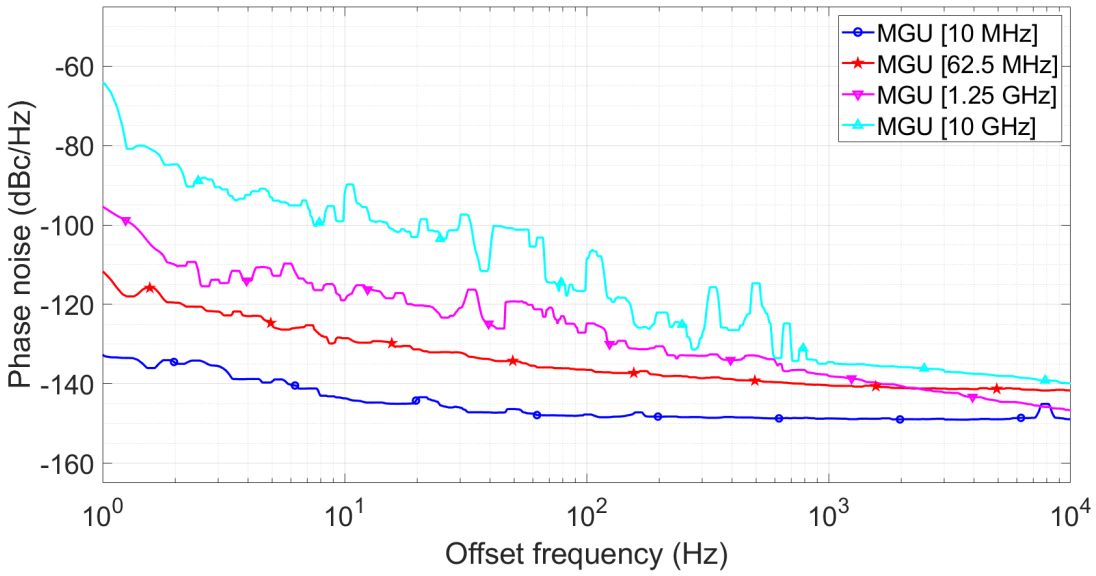

Figure 4.17: Phase noise spectrum of different carrier frequencies of MGU. The phase noise can be seen increasing with the carrier frequency.

MGU at different RF frequencies. The increase in the phase noise values with the increase in the carrier frequency for a specific oscillator is evident in figure 4.17. We can see spurious peaks at different offset frequencies in most phase noise spectra. These spurious peaks are the artefact of the PNA and are more frequent at higher carrier frequencies. The peaks also relate to environmental disturbances and frequency cross-talk. Out of all the phase noise measurements performed, the spurious peaks were highest for the phase noise measurement of MGU at 1.25 GHz and 10 GHz, as shown in figure 4.17. The phase noise measurements were very noisy at higher frequencies, even after providing higher cross-correlation values. The measurement duration for these higher frequencies is more than 48 hours, and the external disturbance in the laboratory also affects the phase noise spectrum. The phase noise at the 10 GHz carrier frequency of Menlo is worse than the 10 MHz carrier frequency scaled to 10 GHz (using the 20log10(N) formula). The reason is that the Menlo MGU uses two different comb nodes to derive the 10 GHz and 10 MHz outputs. Also, the electronics inside the Menlo to derive 10 GHz and 10 MHz is different from the electronics for 10 MHz giving extra phase noise.

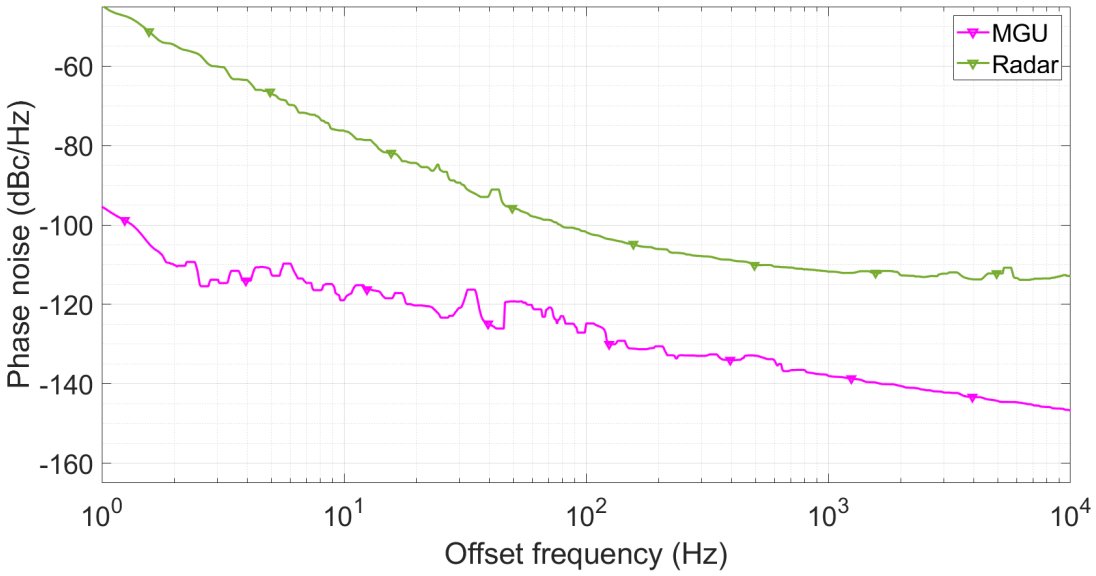

Figure 4.18: Phase noise spectrum at the transmit frequency of the L-band staring radar and phase noise spectrum of MGU at a frequency equivalent to the transmit frequency. The phase noise of the MGU is at least 20 dB less compared to the phase noise at the transmit frequency of the radar at every offset frequency from the carrier.

In addition to the phase noise measurements performed by the author, the phase noise at the transmit frequency of the staring radar, by taking the CW output of the transmit signal prior to the vector modulator, was measured using the PNA by other colleagues within the research group. Method 1, discussed in section 4.4.1.1, was used to directly connect the CW output of the transmit signal to the PNA. Since the PNA cannot measure the phase noise of a pulsed signal, the only point where a realistic measurement of the phase noise can be performed is before the vector modulator. The timing and waveform generator (TWG) board inside the radome, which houses the vector modulator, along with the envelope generator and other modules, has a CW test output which is used as the probe to measure the phase noise of the reference staring radar. The phase noise spectrum in figure 4.18 compares the phase noise at the transmit frequency of the staring radar with the phase noise at the output of the MGU at carrier frequency equivalent to the transmit frequency of the staring radar. In figure 4.18, we can see that the phase noise of the MGU is at least 20 dB less compared

to the phase noise at the transmit frequency of the radar at every offset frequency from the carrier. Figure 4.18 shows the huge potential of the MGU to provide ultra-low phase noise.

The MGU is a suitable oscillator to replace the conventional radar oscillators to provide low phase noise at the transmit frequency. However, the staring radar can currently take in a signal only at the local reference frequency, which is then up-converted to the transmit frequency within the radar. This up-conversion process adds additional phase noise. If the radar transmitter can operate directly with an external reference source operating at the transmit frequency, more of the lower phase noise can be preserved in the radar transmit chain.

The MGU is currently referenced to its internal laser. The MGU can be further improved by referencing it with optical atomic clocks. The ultra-high precision and stability of the optical atomic clocks can be transferred to the RF signal at the output of the MGU by locking the MGU to the optical atomic clocks [69].

4.5 Conclusion

This chapter provides a detailed insight into the characterisation of a wide variety of oscillators, both classical and quantum. The oscillators were characterised using two figures of merit: Allan deviation and phase noise. Allan deviation quantifies the frequency stability of oscillators in the time domain, and phase noise is the measure of oscillator frequency stability in the frequency domain. The phase noise of different oscillators at 10 MHz and 62.5 MHz carrier frequency is theoretically upscaled to a carrier frequency of 1.25 GHz and is compared with the MGU at 1.25 GHz and radar transmit signal at frequency offsets of 1 Hz, 10 Hz, 100 Hz, and 1000 Hz and is given in the table 4.7. From table 4.7, we can clearly see that the phase noise of the MGU is much lower than the phase noise of any other

oscillator at 1.25 GHz.

Oscillator	Phase noise (dBc/Hz)		
	1 Hz	10 Hz	100 Hz
Axtal OCXO (10 MHz upscaled to 1.25 GHz)	-65.7	-92.7	-109.9
Hydrogen Maser (10 MHz upscaled to 1.25 GHz)	-80.9	-104.2	-110.8
UTC Rack (10 MHz upscaled to 1.25 GHz)	-63.6	-94.3	-104.7
Vectron OCXO (62.5 MHz upscaled to 1.25 GHz)	-47.2	-77.3	-106.2
MGU (1.25 GHz)	-95.7	-118.9	-127.1
Radar (Transmit frequency)	-45.2	-76.2	-101.8

Table 4.7: Phase noise at offset frequencies of 1 Hz, 10 Hz, and 100 Hz for all oscillators, either directly at carrier frequency 1.25 GHz or upscaled to the carrier frequency of 1.25 GHz

The chapter also clearly showed that the quantum oscillators have better Allan deviation and phase noise values compared to conventional radar oscillators. The MGU provided Allan deviation values of at least two orders of magnitude below the conventional radar oscillators. The MGU has the further potential to provide Allan deviation values of at least four orders of magnitude below the conventional radar oscillators. MGU is also shown to have phase noise values of at least 20 dB (at all offset frequencies) below the phase noise of the radar at the transmit frequency.

The detailed study of the characterisation of the classical and quantum oscillators discussed in this chapter, along with the comprehensive radar model discussed in chapter 3, is used to study the fundamental limitations of oscillator phase noise and to explore the performance capabilities of the quantum-enabled radar in chapter 5.

Chapter Five

QUANTUM-ENABLED RADAR AND PHASE NOISE

This chapter explores the fundamental limitation of the oscillator phase noise in the performance of a radar system and the performance capabilities of a quantum-enabled radar in simulation. The experimental characterisation of the classical and quantum oscillators described in chapter 4 is applied to the comprehensive radar model detailed in chapter 3 to perform the simulations in this chapter. The chapter starts with a general overview of the phase noise in radar systems. The reader is then directed to modelling the oscillator phase noise in the simulation. The chapter then discusses the limitations of classical oscillator phase noise in radar systems. The chapter also discusses the advantages of quantum-enabled radar with low phase noise quantum oscillators.

5.1 Phase noise in radar systems

Out of the different internal and external noise sources in a radar system, phase noise and thermal noise are the two crucial internal noises. As described in detail in section 2.3.3,

the phase noise of an oscillator is related to the random frequency/phase fluctuations in the frequency domain. In radars, the random fluctuation of the frequency/phase of the output of the radar oscillator is a significant contributor to the overall phase noise. The radar oscillator phase noise is translated through the different hardware blocks and data processing chain to radar range-Doppler plots. In range-Doppler plots, the phase noise is manifested as clutter-induced phase noise floor.

In radars, the thermal noise is attributed to the thermal agitation of electrons in the various components of the radar receive chain and is described in detail in section 2.3.1.1. Radar target detection is always limited by the receiver's thermal noise. In range-Doppler plots, the thermal noise is manifested as uniform thermal noise floor present in all range bins. The thermal noise provides a lower bound to the noise level in the range-Doppler plots. Throughout the receive chain and data processing chain of a radar system, different levels of processing are performed to reduce the noise levels and to improve the SNR.

Radar range-Doppler plots provide the range and Doppler information of targets and clutter in the radar field of view. In an ideal radar, without any phase noise, the SNR of a radar target is defined as the target peak power with respect to the thermal noise floor in the range-Doppler plot. In a real radar, however, the stationary clutter in all the range bins results in clutter-induced phase noise in the range-Doppler plots. The clutter-induced phase noise floor is related to the clutter power levels in the range bins: the higher the clutter power, the higher the phase noise floor. However, the presence of clutter can make it more difficult to detect weak signals and may require higher transmitter power, which can, in turn, increase the level of phase noise in the system. Therefore, the relationship between clutter and phase noise is indirect and depends on the specific characteristics of the radar system and the environment in which it operates.

In range bins with higher clutter power, the clutter-induced phase noise floor emerges

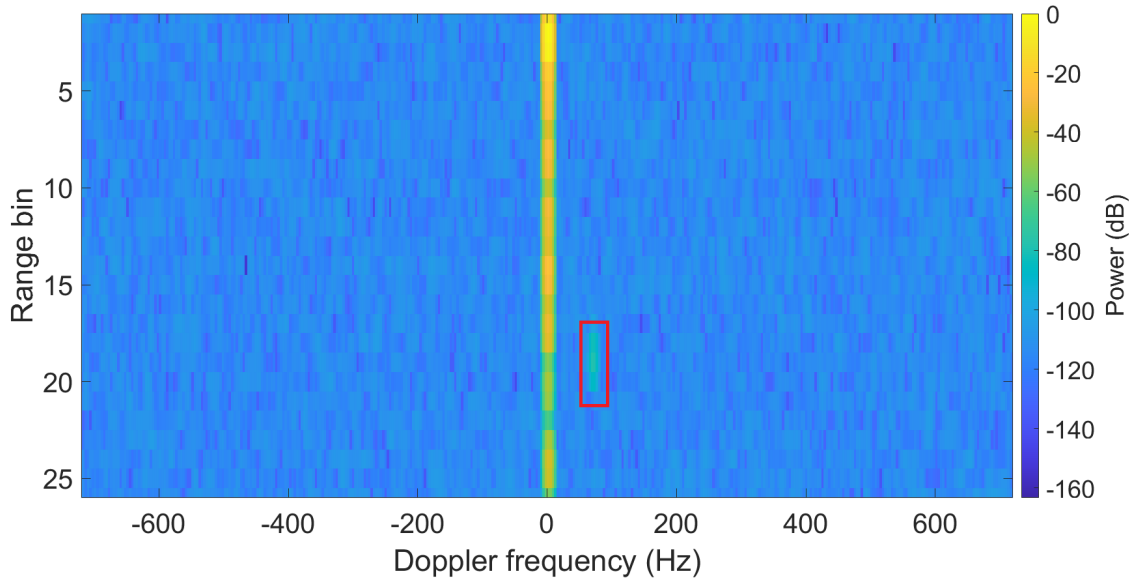

(a) Simulated range-Doppler plot of an ideal hypothetical radar without any phase noise showing the uniform thermal noise background.

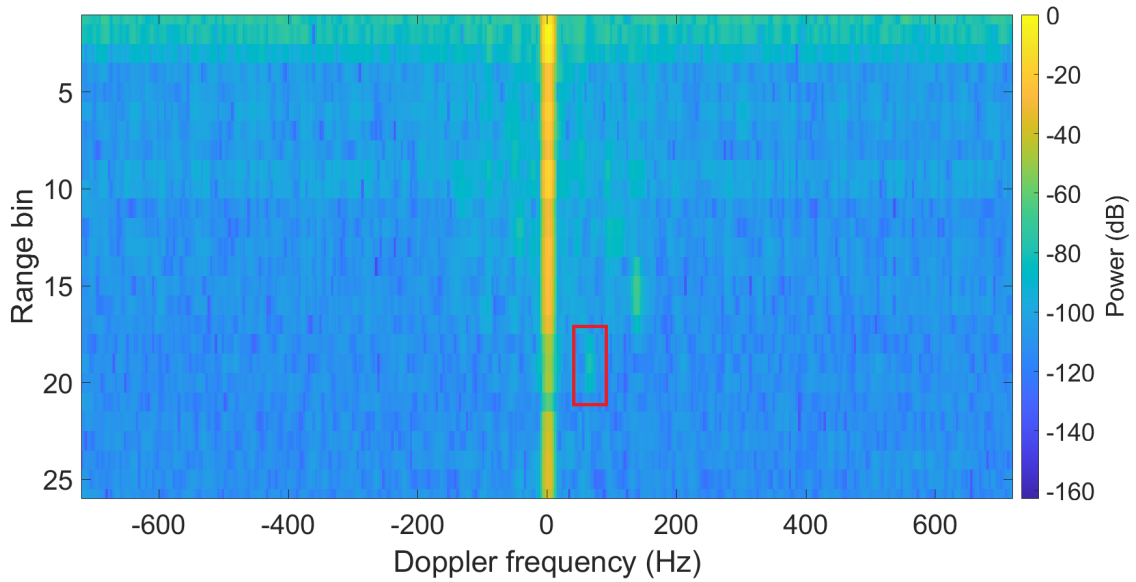

(b) Real range-Doppler plot from a radar trial with clutter-induced phase noise emerging out of the thermal noise floor for range bins with higher clutter power.

Figure 5.1: Comparison of the simulated range-Doppler plot of an ideal radar without any phase noise with the range-Doppler plot from the staring radar trial. The target of interest is highlighted in the red box.

out of the uniform thermal noise floor. The increase in the overall noise floor, consisting of phase noise floor and thermal noise floor, demands a higher target return power for efficient

detection. Thus, the increase in phase noise floor due to higher clutter power can result in the misdetection of weak targets.

The range-Doppler plot with a target of interest for an ideal hypothetical radar without any phase noise and the real range-Doppler plot from the staring radar with oscillator phase noise is given in figure 5.1 (same as figure 3.23). The increase in the phase noise floor, as seen in figure 5.1b, results in the reduction of the SNR available for efficient target detection. Since the simulated radar model consists of only one element of the receive antenna, the real data corresponds to the data from a single beam direction of the staring radar trial.

5.2 Oscillator phase noise in simulation

The oscillator phase noise is crucial in any radar system. The comprehensive radar model discussed in chapter 3 and the oscillator phase noise measurements described in chapter 4 can be used to perform advanced simulations to explore the effects of phase noise in radar systems. The first step in exploring the effects of phase noise in radar systems through simulation is to confidently replicate the measured oscillator phase noise spectrum in the simulation. As discussed in section 3.2.1.3, the comprehensive radar model simulates the transmit PLL as a DDS to generate the signal directly at the RF transmit frequency. Hence, the first stage at which the oscillator phase noise can be introduced into the comprehensive radar model is at the transmit PLL of the simulation.

The phase noise block within the Simulink was used to add phase noise into the simulation. The phase noise block can add phase noise at any oscillator carrier frequency. The phase noise block inputs user-defined frequency offset values and the corresponding phase noise levels. The frequency offset and the phase noise level of any characteristic oscillator can be fed into the phase noise block, and the phase noise block generates a phase

noise spectrum passing through the specified points. To replicate the measured classical and quantum oscillator phase noise in simulation, the phase noise block was integrated into the transmit PLL block of the comprehensive radar model.

The transmit PLL block outputs the waveform at both the baseband and the carrier frequency. Since the phase noise is defined as the noise sidebands per Hz at an offset frequency from the carrier frequency, the phase noise spectrum in the simulation essentially needs a resolution bandwidth of 1 Hz. Since the transmit frequency of the staring radar is in L-band, generating a phase noise spectrum with 1 Hz bandwidth for an L-band carrier frequency requires very high processing capability. In the simulation, the phase noise spectrum was generated in MATLAB by taking the baseband signal at the output of the transmit PLL block using the test probes. The phase noise spectrum in the simulation was able to replicate the reference phase noise spectrum for different oscillators at offset frequencies of 10 Hz and above. Below 10 Hz, the phase noise spectrum showed a small deviation between the expected and simulated phase noise values. Since we are interested in slow-moving targets like drones that generally have a Doppler frequency range of a few 10s to 100s of Hz, the phase noise at offset frequencies above 10 Hz is of greater interest.

The phase noise block in the simulation was able to replicate the phase noise spectrum of any oscillator at any carrier frequency and for offset frequencies of 10 Hz and above. Since the comprehensive radar model simulates phase noise at the transmit PLL level, the phase noise at the transmit frequency of the L-band staring radar is of utmost significance. The phase noise at the transmit frequency of the staring radar and the MGU at a frequency equivalent to the transmit frequency of the radar was measured and plotted in figure 4.18. In order to study the limitations of the oscillator phase noise and to explore the possibility of using the quantum oscillator with low phase noise (MGU) in radar systems, the phase noise spectra in figure 4.18 were replicated in the simulation. Figure 5.2 shows the measured phase noise at the transmit frequency for both the staring radar and the MGU and the equivalent

phase noise spectra generated in the simulation.

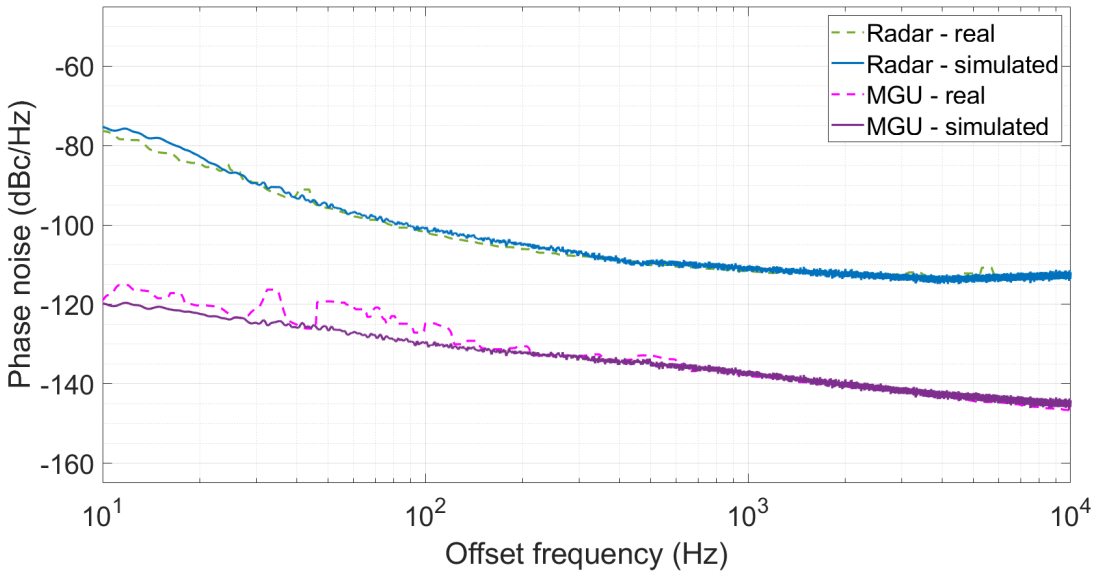

Figure 5.2: Comparison of the measured and simulated phase noise spectra at the transmit frequency of the staring radar and MGU at a frequency equivalent to the transmit frequency. The simulated phase noise spectra overlap with the measured phase noise spectra to a good extent.

In figure 5.2, we can see that the phase noise spectra generated in the simulation are comparable to the measured phase noise spectra. The phase noise spectra are generated by making use of the MATLAB signal analyser application. The signal analyser application generates the frequency spectrum for any input signal. A separate code was developed to produce the phase noise spectrum from the frequency spectrum by taking only the positive half of the frequency spectrum and by changing the RBW to 1 Hz. The measured phase noise spectra consisted of spurious peaks attributed to the PNA, environmental disturbances and frequency cross-talk. The spurious peaks of the measured phase noise spectra were intentionally removed in the simulated phase noise spectra. The lower phase noise level of the quantum oscillator, MGU, is expected to reduce the clutter-induced phase noise floor in the range-Doppler plot and hence improve the performance capabilities of the radar.

5.3 Limitations of phase noise in classical radars

The limitation of phase noise in the performance of a classical radar system, introduced earlier in section 5.1, is further explored by studying the effects of classical oscillator phase noise in radar range-Doppler plots. The simulated replica of the phase noise at the transmit frequency of the radar discussed in section 5.2 was integrated into the comprehensive radar model discussed in chapter 3 to study the effects of phase noise in a classical radar system. As a first step, the comprehensive radar model with phase noise was used to replicate a real staring radar trial range-Doppler plot. The staring radar trial considered was the same trial discussed in the validation of the radar model with thermal noise (section 3.6.3). The real staring radar trial consisted of a drone flying towards the radar at a radial velocity of 8.3 m/s. In section 3.6.3, the capability of the comprehensive radar model to replicate the thermal noise floor, clutter power levels, and the target SNR was discussed in detail.

The range-Doppler plot of the radar trial realised in the simulation and the real staring radar trial is given in figure 5.3. Figure 5.3 clearly shows good parity between the real and simulated range-Doppler plot with classical oscillator phase noise. Figure 5.3 represents the capability of the comprehensive radar model to replicate real staring radar trials with a great level of detail. The real range-Doppler plot in figure 5.3b consists of unwanted targets in the radar field of view along with the target of interest. At the same time, only the target of interest was modelled in the simulated range-Doppler plot in figure 5.3a. In both the range-Doppler plots in figure 5.3, we can clearly see the presence of phase noise floor. The phase noise floor can be seen coming out of the thermal noise floor for range bins with higher clutter power. Since the reflected power from the clutter is inversely proportional to the fourth power of the clutter range, in almost all cases, the range bins closer to the radar will have the highest clutter powers. In figure 5.3, the phase noise floor can be evidently

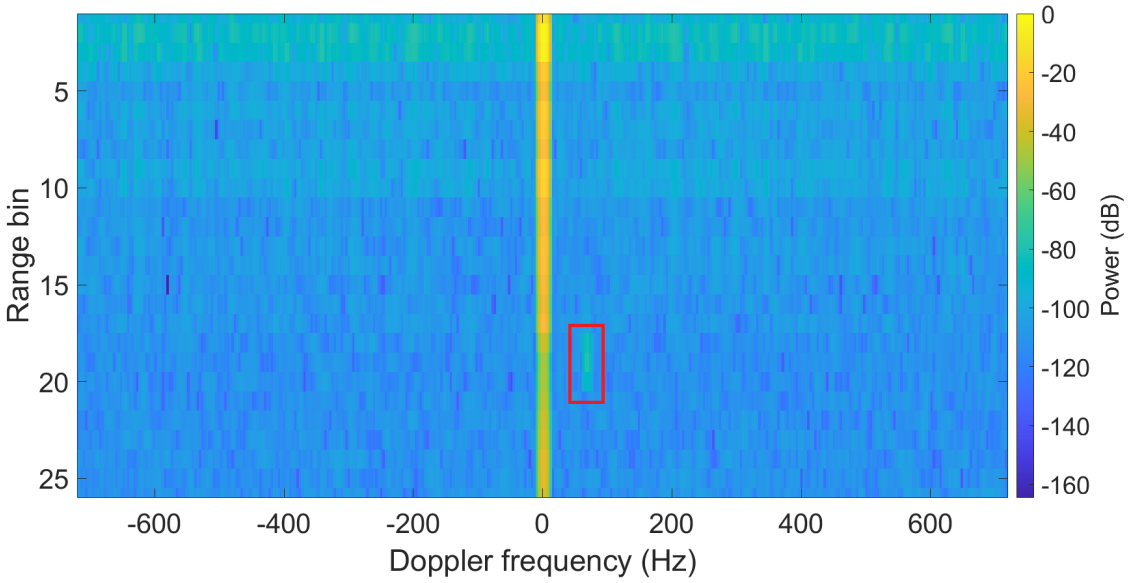

(a) Simulated range-Doppler plot with classical oscillator phase noise.

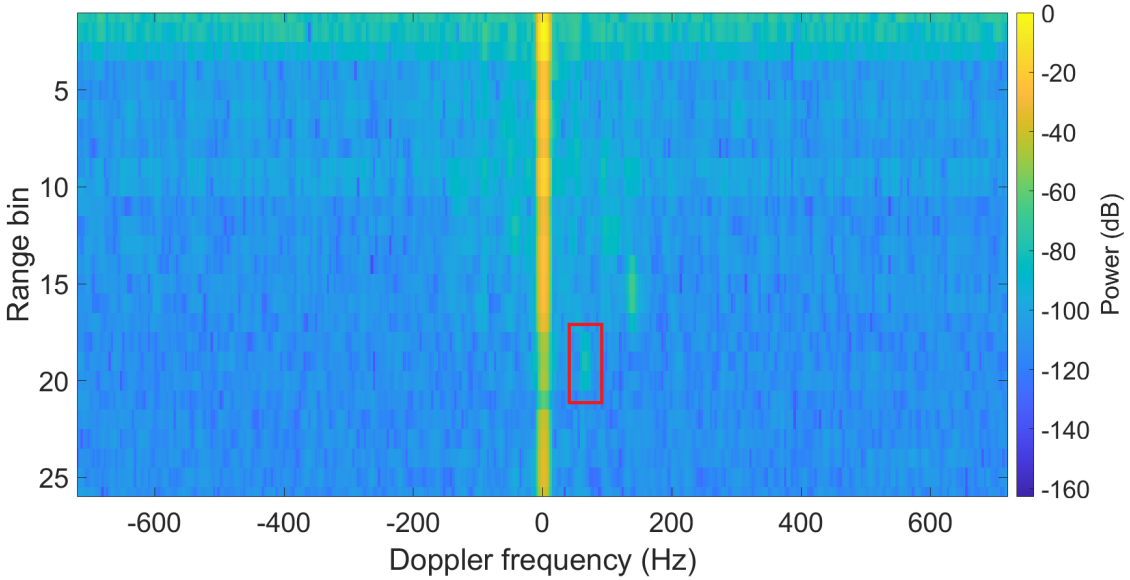

(b) Real range-Doppler plot from the staring radar trial with classical oscillator phase noise. The range-Doppler plot also consists of other unwanted targets as seen by the radar.

Figure 5.3: Comparison of the simulated and real range-Doppler plot with classical oscillator phase noise. The phase noise floor can be seen coming out of the thermal noise floor for range bins with higher clutter power. The target of interest is highlighted in the red box.

seen coming out of the thermal noise floor in range bins close to the radar (range bins 1 - 4), where the clutter power is high. The effect of phase noise is also visible for range bins 6,

7, 9, and 10, with relatively higher clutter power.

A better comparison of the relationship between the simulated and real-range range-Doppler plot with classical oscillator phase noise is given in figure 5.4. The comparison graph in figure 5.4 shows the peak clutter power, the thermal noise floor, and the overall noise floor for both the simulated and real range-Doppler plot in figure 5.3. The thermal noise floor refers to the noise floor for the range bin considerably away from the radar and the Doppler bin considerably away from the central Doppler bin, where the effect of the clutter-induced phase noise is negligible. The comparison graph in figure 5.4 is an extended version of the comparison graph described in section 3.6.3 with the inclusion of the overall noise floor in each range bin. The overall noise floor consists of both the thermal noise floor and the phase noise floor.

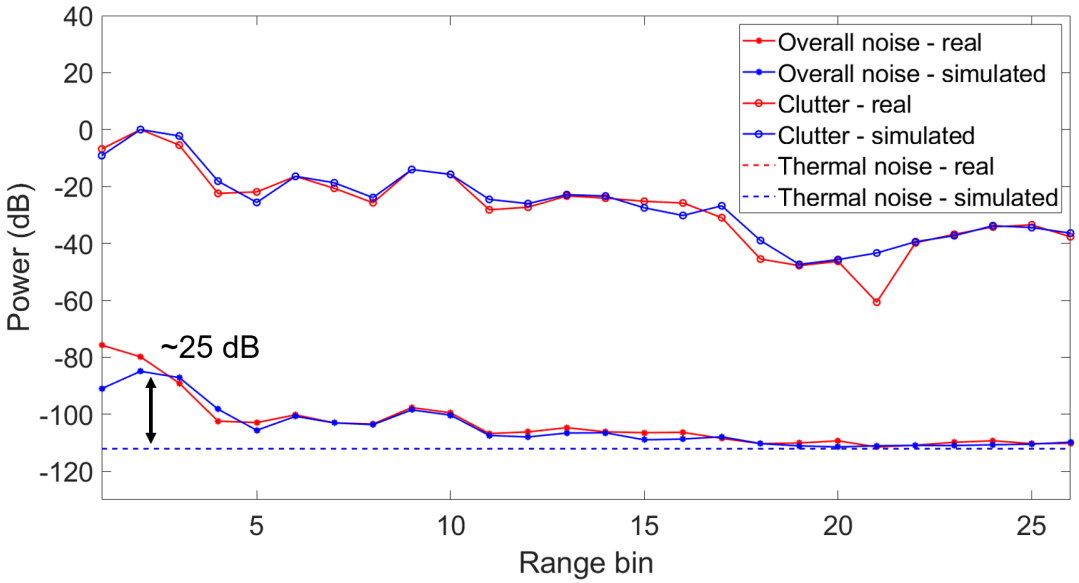

Figure 5.4: The comparison graph showing the peak clutter power, overall noise floor, and thermal noise floor for each range bin for both the simulated and real range-Doppler plot with classical oscillator phase noise. The overall noise floor for both the simulation and real data overlap to a good extent. The overall noise floor for range bins close to the radar is increased by nearly 25 dB above the thermal noise floor. The thermal noise floor in simulation fully overlaps with the real data and hence is not differentiable.

In figure 5.4, we can see that the overall noise floor for both the real and simulated

range-Doppler plots overlaps to a great extent. Since the clutter power in each range bin cannot be fully replicated in the simulation, a minor deviation in the overall noise floor between the simulation and the real range-Doppler plot is expected. The overall noise floor for the first range bin in the simulation is considerably away from the real range-Doppler plot and is an artefact of the staring radar hardware. The good parity of the overall noise floor between the real and the simulated range-Doppler plot validates the confidence in the comprehensive radar model as a tool to explore the limitations of phase noise in classical radars.

In figure 5.4, we can clearly see an increase in the phase noise floor for those range bins with higher clutter levels. The effect is very evident in range bins close to the radar, where we can see the phase noise floor increased by at least 25 dB above the thermal noise floor. The clutter-induced phase noise floor in the range-Doppler plot is the manifestation of the classical oscillator phase noise. For every dB of increase in the phase noise floor above the thermal noise floor, the effective SNR available for target detection is reduced by a dB.

The overall noise floor in the simulated range-Doppler plot in figure 5.3 was used to generate detection plots for the classical radar in simulation, as shown in figure 5.5. The detection plot in figure 5.5 also includes the detection threshold, at 20 dB above the overall noise floor, equivalent to an SNR of 20 dB, typical for a radar system. The target in the detection plots was mathematically shifted to be present in the different range bins, following the $1/R^4$ relation between the range and the reflected target power. In the detection plots in figure 5.5, the value of one (1) corresponds to the target getting detected in the specific range bin, and a value of zero (0) corresponds to the target not getting detected in the specific range bin. The detection plot in figure 5.5 represents two different simulations. Figure 5.5a shows the detection plot with the target used in the staring radar trial simulated in the range-Doppler plot in figure 5.3a. Figure 5.5b shows the detection plot from a mathematical simulation with a hypothetical target having an RCS 15 dBsm lower than the target used in

the staring radar trial simulated in the range-Doppler plot in figure 5.3a, with all the other parameters same as 5.3a.

The simulated detection plot with the classical radar in figure 5.5 shows that even though the specific target used in the trial gets detected in all range bins, mathematical simulation with the target with an RCS 15 dBsm lower than the target used in the trial fails to get detected in all the range bins. The weaker targets fail to get detected in range bins 2, 3, 14, 15, and 18, and this is the consequence of the increased phase noise floor resulting in the reduction in the SNR available for target detection. The misdetection could also happen with the same target used in the radar trial in a higher clutter environment. The detection plot in figure 5.5 clearly demonstrates the limitation of the classical radar in detecting low-RCS targets in the specific clutter environment modelled in the simulation. The solution to detect weaker targets, even in extreme clutter environments, is to replace the classical radar oscillators with ultra-low phase noise oscillators, for which quantum oscillators are one possible candidate.

5.4 Advantages of quantum-enabled radars

The comprehensive radar model with the capability to replicate real staring radar trials with classical oscillator phase noise, described in section 5.3, is a powerful tool for exploring the advantages of quantum oscillators in radar target detection. A quantum-enabled radar consists of a quantum oscillator that replaces a classical radar oscillator. The very first modelling of a quantum-enabled radar was successfully realised in the simulation by replacing the phase noise at the transmit frequency of the classical radar with the phase noise of the MGU at a frequency equivalent to the radar transmit frequency. The simulated phase noise spectrum of the MGU discussed in section 5.2 was integrated into the comprehensive radar

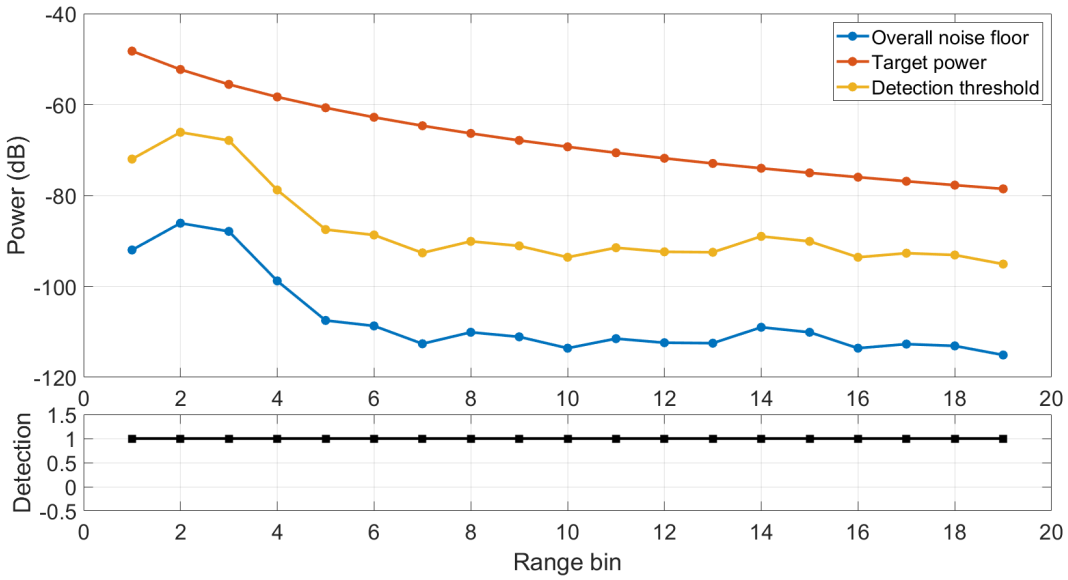

(a) Detection plot for classical radar with the target simulated in the classical radar range-Doppler plot in figure 5.3a. The target is getting detected in all the range bins.

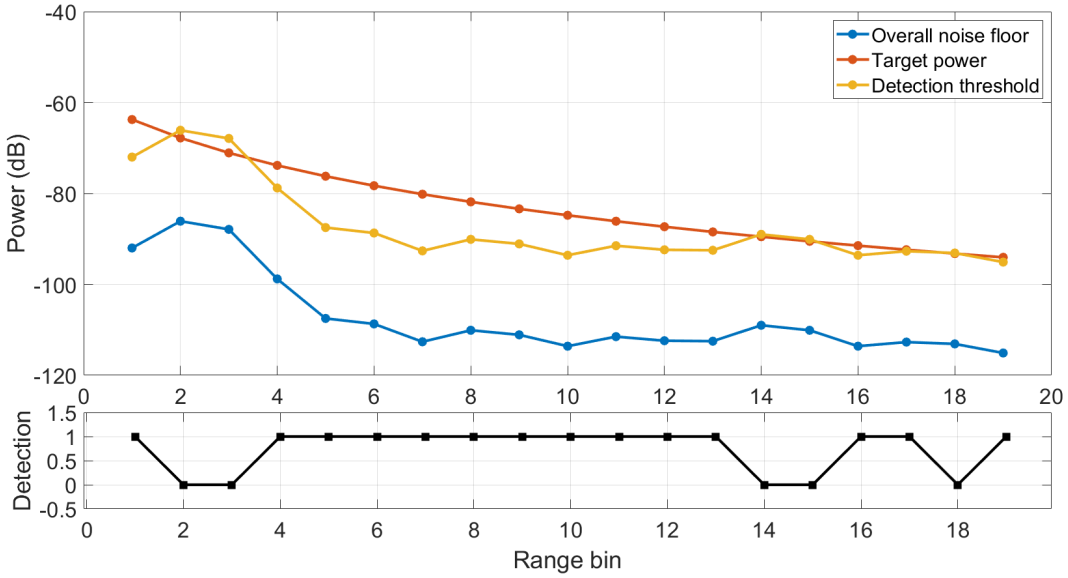

(b) Detection plot for classical radar with a hypothetical target having RCS 15 dBsm lower than the target simulated in the classical radar range-Doppler plot in figure 5.3a. The target fails to get detected in range bins 2, 3, 14, 15, and 18. The failure in detection is the consequence of increased phase noise floor due to higher clutter power.

Figure 5.5: Simulated classical radar detection plots consisting of the overall noise floor, the detection threshold at 20 dB above the noise floor, and the target power for each range bin. The values one and zero in the detection plot correspond to the target getting detected and the target not getting detected in the specific range bin, respectively.

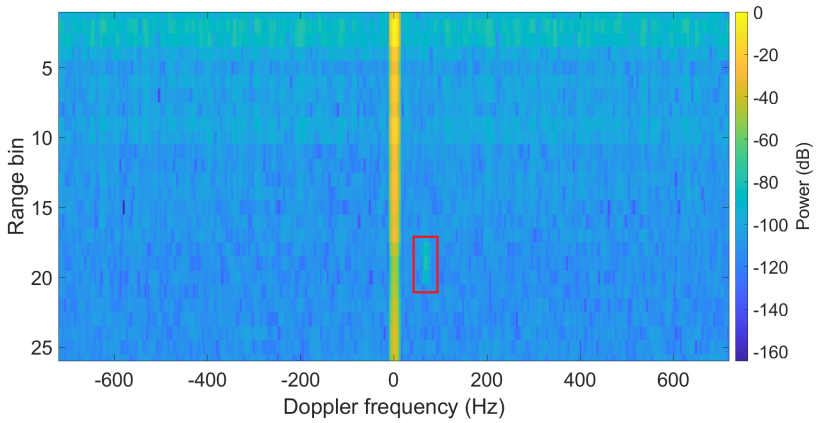

(a) Simulated range-Doppler plot with classical oscillator phase noise.

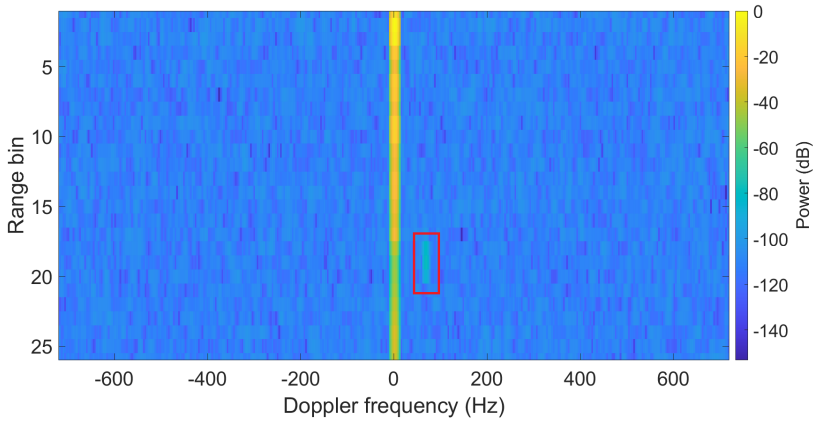

(b) Simulated range-Doppler plot with quantum oscillator phase noise.

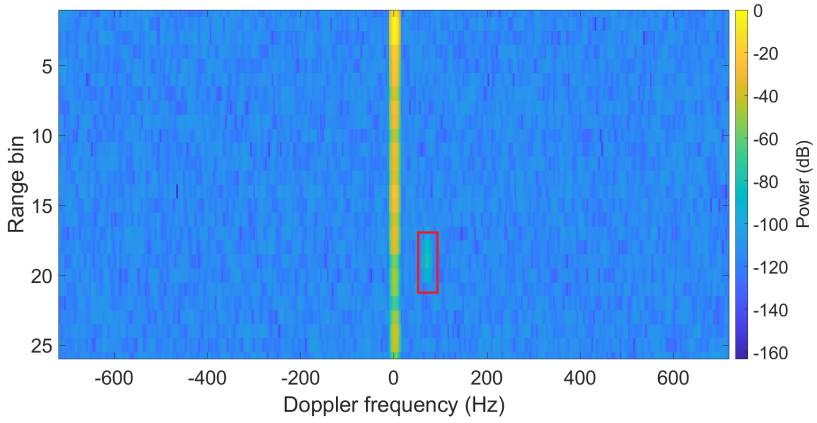

(c) Simulated range-Doppler plot without phase noise.

Figure 5.6: Comparison of the simulated range-Doppler plots with classical oscillator phase noise, quantum oscillator phase noise and no phase noise. The clutter-induced phase noise floor is almost invisible in the range-Doppler plot with quantum oscillator phase noise.

model to generate the quantum-enabled radar range-Doppler plot with all other parameters the same as the classical staring radar trial discussed in section 5.3.

Figure 5.6 compares the range-Doppler plot of the classical radar in simulation (as discussed in section 5.3) with the range-Doppler plot of a quantum-enabled radar in simulation and with the ideal range-Doppler plot without any phase noise. The range-Doppler plot of the quantum-enabled radar in simulation, given in figure 5.6b shows a considerable reduction in the clutter-induced phase noise floor compared to the range-Doppler plot of the classical radar in simulation, given in figure 5.6a. We can also see that, qualitatively, the range-Doppler plot of the quantum-enabled radar in simulation is very close to the range-Doppler plot without any phase noise, given in figure 5.6c. Figure 5.6b is mainly limited by thermal noise with a minor contribution of clutter-induced phase noise in the range bins close to the radar. Figure 5.6 clearly shows the ability of the quantum oscillator with low phase noise, in comparison to a classical oscillator, to substantially bring down the clutter-induced phase noise floor in the range-Doppler plot for the same clutter environment.

The parameters from the classical and quantum-enabled radar range-Doppler plot in figure 5.6 were utilised to quantitatively compare quantum-enabled radar with classical radar. The comparison graph in figure 5.7 consists of peak clutter power, overall noise floor, and thermal noise floor for each range bin of the classical radar and quantum-enabled radar. Since the simulation parameters remain the same, both the clutter power and the thermal noise floor in figure 5.7 overlap.

In figure 5.7, the overall noise floor consisting of phase noise floor and thermal noise floor for the quantum-enabled radar is considerably below the overall noise floor of the classical radar. For range bins close to the radar, the overall noise floor of the quantum-enabled radar is at least 20 dB below the classical radar. The overall noise floor of the quantum-enabled radar is also very close to the thermal noise floor, indicating that the

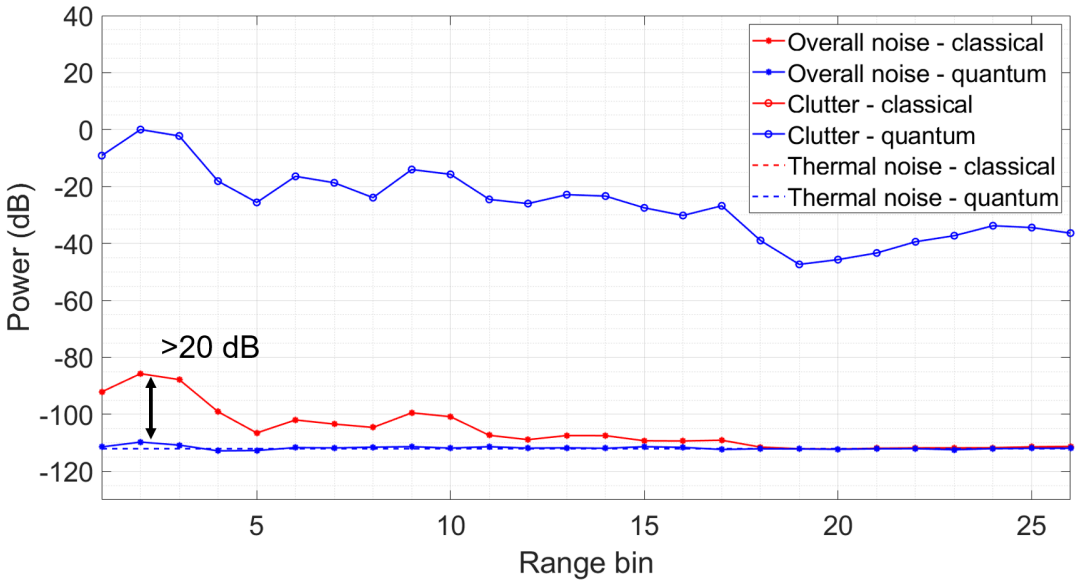

Figure 5.7: The comparison graph showing the peak clutter power, overall noise floor, and thermal noise floor for each range bin for both the classical and quantum-enabled radar. For range bins close to the radar. The overall noise floor of the quantum-enabled radar is at least 20 dB below the classical radar. The thermal noise floor and the clutter power fully overlap and hence are not differentiable.

quantum-enabled radar with a quantum oscillator having a very low phase noise is only limited by the thermal noise floor for the clutter environment realised in the comparative study.

Similar to the detection plots for classical radar discussed in section 5.3, the overall noise floor in the range-Doppler plot in figure 5.6b was used to generate detection plots for quantum-enabled radar in simulation, and is shown in figure 5.8. The detection plot in figure 5.8a corresponds to the target used in the simulated quantum-enabled radar range-Doppler plot in figure 5.6b, also the same as the target used in the detection plot for classical radar in figure 5.5a. The detection plot in figure 5.8b corresponds to a target having a lower RCS, the same as the hypothetical target used in the detection plot for classical radar in figure 5.5b.

The simulated detection plots for quantum-enabled radar in figure 5.8 show that both

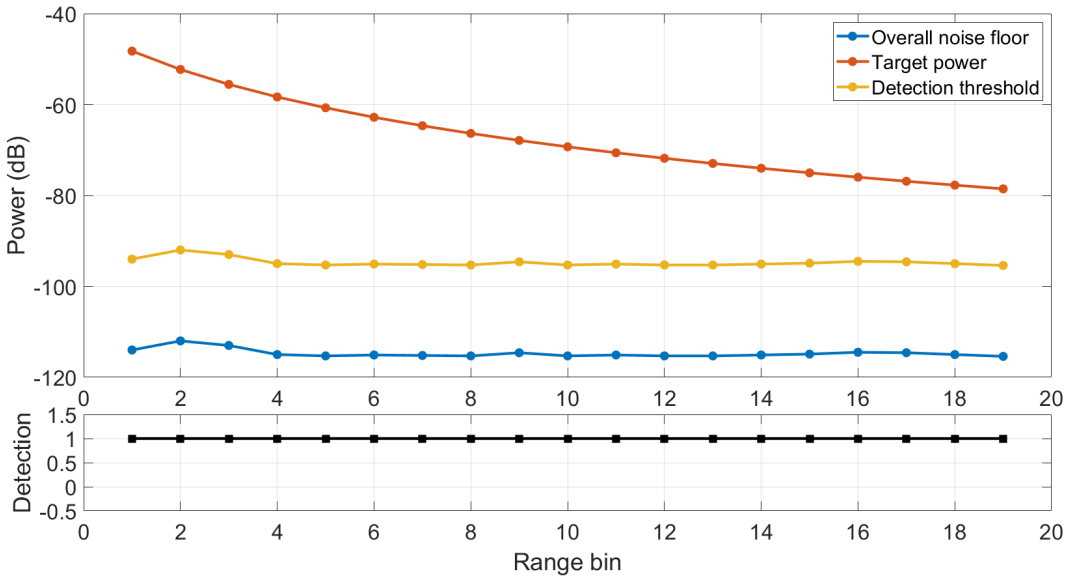

(a) Detection plot for quantum-enabled radar with the target simulated in the quantum-enabled radar range-Doppler plot in figure 5.6b. The target is getting detected in all the range bins.

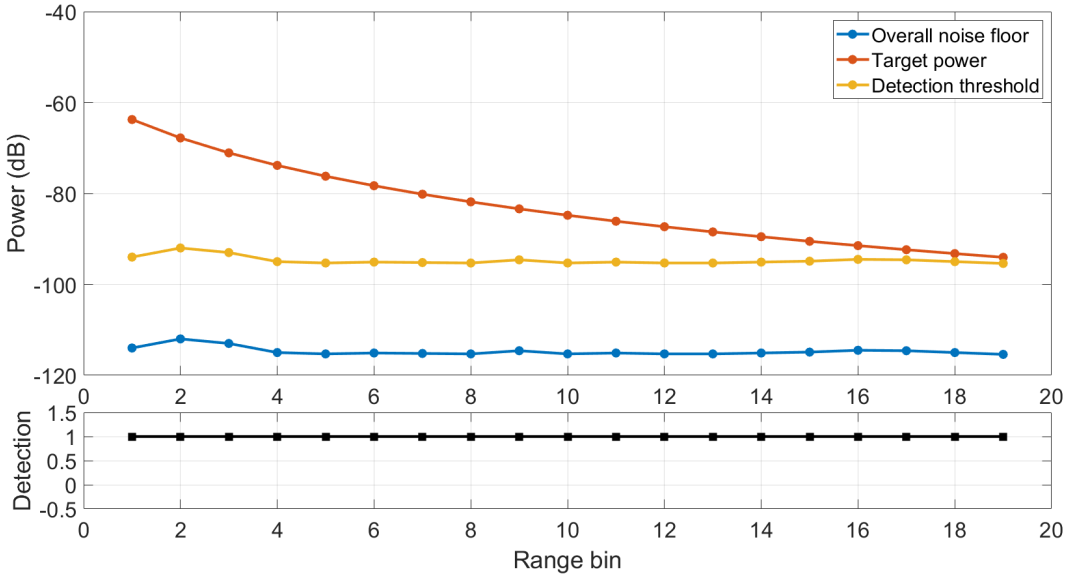

(b) Detection plot for quantum-enabled radar with a target having RCS 15 dBsm lower than the target simulated in the quantum-enabled radar range-Doppler plot in figure 5.6b. The target is getting detected even in range bins with higher clutter power.

Figure 5.8: Simulated quantum-enabled radar detection plots consisting of the overall noise floor, the detection threshold at 20 dB above the noise floor, and the target power for each range bin. The values one and zero in the detection plot correspond to the target getting detected and the target not getting detected in the specific range bin, respectively.

the targets, the specific target used in the quantum-enabled radar range-Doppler plot and the hypothetical target with lower RCS get detected in all the range bins for the specific clutter environment modelled in the simulation. Comparing the quantum-enabled radar detection plot in figure 5.8 with the classical radar detection plot in figure 5.5, we can conclude that even the targets that failed to get detected in range bins with higher clutter power for the classical radar get detected with the quantum-enabled radar. Since the phase noise floor of the quantum-enabled radar is very close to the thermal noise floor, the detection threshold for the quantum-enabled radar stays considerably below the detection threshold for the classical radar. Even in a higher clutter environment and with a weaker target, the ultra-low phase noise of the quantum oscillator helps to keep the clutter-induced phase noise floor to a very low level, resulting in almost zero cases of misdetection due to phase noise floor.

5.5 Conclusion

This chapter presented the very first realisation of a quantum-enabled radar in simulation. The chapter also provided a detailed study of the effects of classical oscillator phase noise in radar systems and the potential advantages of quantum-enabled radar with ultra-low phase noise quantum oscillators over classical radars. The studies were enabled by integrating the phase noise measurements provided in chapter 4 to the comprehensive radar model discussed in chapter 3.

The range-Doppler plot with classical radar oscillator showed the phase noise floor emerging from the thermal noise floor for range bins with higher clutter power. The overall noise floor of the classical radar range-Doppler plot was at least 25 dB above the thermal noise floor for the range bins close to the radar. The classical radar detection plots showed a target failing to get detected in range bins with increased phase noise floor due to higher

oscillator phase noise.

Simulations with low phase noise quantum oscillator generated quantum-enabled radar range-Doppler plot with almost negligible phase noise floor for the clutter environment simulated in the model. The clutter-induced phase noise floor of the quantum-enabled radar was lower than the classical radar by at least 20 dB for the range bins close to the radar. The quantum-enabled radar detection plot showed a detection threshold considerably lower than the classical radar detection plot. The quantum-enabled radar detection plot also showed the targets getting detected, even in range bins with higher clutter power. The quantum-enabled radar with low-phase noise quantum oscillators can thus detect slow-moving low-RCS targets even in extreme clutter.

Chapter Six

CONCLUSION

This thesis has focused on the development of a whole radar model to evaluate the performance capabilities of quantum-enabled radar systems and to study the fundamental limitations of oscillator phase noise in target detection. The first section of the chapter describes a brief summary of the work presented in the thesis. The second section discusses the conclusions arrived at from the thesis work. In the third section, future work is given in detail.

6.1 Summary

The aim of this thesis was to model the performance of a quantum-enabled radar. The chapter 2 presented the background theory related to radar systems. The background theory included an outline of the basic radar configuration, fundamental radar parameters, and noise in radar systems. The noise in radar systems consisted of a detailed section on the definition and properties of phase noise.

The development of a whole radar model in MATLAB/Simulink environment and the validation of the radar model by comparison of simulated data with the data from actual

staring radar trials were presented in chapter 3. The radar model consisted of all the fundamental hardware building blocks in the transmit chain, the receive chain, and the data processing chain. The transmit chain consisted of transmit PLL, envelope generator and vector modulator, amplifier, and antenna. The receive chain consisted of receive antenna, thermal noise block, LNA, receive PLL, mixer, BPF, and ADC. The data processing chain consisted of Hilbert transform and matched filtering, windowing, FFT, and range-Doppler plot. The radar model also simulated targets and clutter in the environment as point scatterers. The theory behind each building block and the realisation of every building block in the simulation platform was described in detail. The whole radar model was validated by comparing the system-level signal powers, the SNR, range and Doppler basic parameters, and the range-Doppler plots obtained from both the simulation and actual staring radar trials.

Chapter 4 presented the experiments performed for characterising different oscillators. The chapter 4 consisted of a description of different types of oscillators (both classical and quantum oscillators), a description of Allan deviation and phase noise as two figures of merit for the characterisation of oscillators, methods to measure the figures of merit and the measurement results. The chapter consisted of four different methods to measure the Allan deviation and three different methods to measure the phase noise and accommodates both RF and optical oscillators. The results from the measurement campaign were represented in graphical form to compare and evaluate the performance of both the classical and quantum oscillators.

The whole radar model built and discussed in chapter 3 and the measurement campaign performed and discussed in chapter 4 were utilised to study the effects of oscillator phase noise in target detection and to develop simulations towards quantum-enabled radar in chapter 5. Chapter 5 consisted of validating the whole radar model with oscillator phase noise by comparing the results generated in the simulation with results from actual staring

radar trials. The radar model validated with oscillator phase noise is then used to generate simulations with low phase noise quantum oscillators to develop the first realisation of a quantum-enabled radar in simulation and to compare the results with classical radar.

6.2 Conclusion

The thesis demonstrated the very first realisation of a quantum-enabled radar with ultra-low phase noise quantum oscillators in the simulation platform. A whole radar model was developed and discussed in chapter 3, based on a commercially available L-band staring radar with a reasonable number of simplifications, and represented the response of every fundamental hardware building block. An extensive comparison of the model with the L-band staring radar showed a high level of parity between the simulated results and the data from the experimental measurements, validating the radar model with real-world data. The whole radar model can optimise any system-level parameter and integrate additional building blocks to represent any real and hypothetical radar scenarios.

The results from the laboratory measurements for phase noise characterisation in chapter 4 were applied to the whole radar model to study the effects of the phase noise of classical and quantum oscillators in radar systems in chapter 5. The phase noise spectra in figure 4.18 showed a quantum oscillator with phase noise values for every offset frequency at least 20 dB lower than the staring radar at the L-band transmit frequency. The considerably low phase noise values of the quantum oscillator make it a potential candidate for ultra-low phase noise radar oscillators. The thesis studied the fundamental limitations of the conventional radar oscillator phase noise in target detection and the performance capabilities of the quantum-enabled radar with ultra-low phase noise quantum oscillators.

The range-Doppler plot from the actual staring radar field trial and the simulated

replica of the staring radar trial showed the phase noise floor at around 25 dB above the thermal noise floor for range bins close to the radar (with higher clutter power), manifesting the limitations of the conventional radar oscillator phase noise floor in radar range-Doppler plots, and is described in detail in section 5.3. For every dB increase in the phase noise floor above the thermal noise floor, the radar loses a dB of SNR available for target detection.

The first quantum-enabled radar was realised in the simulation by replicating the classical oscillator phase noise and substituting it with the quantum oscillator in the whole radar model. The simulated quantum-enabled radar range-Doppler showed low levels of the phase noise floor, very close to the thermal noise floor in comparison to the classical radar range-Doppler plot and is described in detail in section 5.4. The classical and quantum-enabled radar detection plots in figures 5.5 and 5.8 evidently showed quantum-enabled radar detects low-RCS targets that fail to get detected with classical radars in the same clutter environment.

In conclusion, the phase noise floor in the range-Doppler plots is a result of the phase noise of the radar oscillator and is a fundamental limit in the performance of radar systems. The effect is crucial in the detection of low-RCS slow targets. The low-RCS targets, like drones, are extremely difficult to detect in high-clutter environments. The simulations in the thesis have shown that the quantum-enabled radar with ultra-low phase noise quantum oscillators are capable of detecting low-RCS targets, in comparison to classical radars, where the same target in the same clutter environment fails to get detected. The quantum-enabled radar, in reality, would be a breakthrough in the radar community and in the pursuit of the detection of ever-smaller targets.

6.3 Future work

The immediate future of the thesis work includes improved representation of components in the radar model, the utilisation of the radar model to explore the underlying fundamental limitations of different radar building blocks, further measurements and experiments to characterise the performance of additional classical and quantum oscillators, followed by the experimental realisation of the quantum-enabled radar. The experiments and simulations towards quantum-enabled network radars and DDS of the transmit signal in radar systems also constitute future work.

6.3.1 Improving the radar model

As presented in the thesis, the radar model begins at the PLL in the transmit chain and through to the range-Doppler plot in the data processing chain. Even though the radar model consists of all fundamental blocks, it can improve the representation of different building blocks. For example, the radar model has a single transmit and receive element, while the staring radar consists of an array of radar receivers; the model represents the target and clutter only as a point scatterer at a specific distance and RCS, whereas the real targets and clutter are much more than a point scatterer. The radar model can also be expanded to accommodate the realisation of PLL and frequency up-conversion.

6.3.2 Fundamental limitations of radar blocks

The thesis mainly focused on the limitation of oscillator phase noise in radar systems. Along with the oscillators, other building blocks also contribute to the noise in radar systems and limit performance. One of the significant noise sources in radar systems is the

quantisation noise due to analogue to digital conversion [159]. Spurious responses due to clocking, power amplification, mechanical phased-array antennas, phase noise contribution from power amplifiers, and frequency up-conversion through PLO could also contribute to noise in radar systems. The radar model can be used as a tool to study and quantify the noise contributions from different radar building blocks.

6.3.3 Characterisation of additional oscillators

The thesis presented the characterisation of a number of oscillators. Each radar consists of a different reference oscillator. Also, there are quantum oscillators like strontium optical clocks. All these oscillators can be characterised to obtain and assess the phase noise values. One of the exciting measurements in the near future is the phase noise of the strontium optical lattice clock, down-converted to RF using the MGU. The ultra-high precision and accuracy of the strontium atomic clock will be translated to the RF, resulting in an exceptionally low phase noise level quantum oscillator.

6.3.4 Realisation of quantum-enabled radar

The thesis has provided a strong base that concludes the advantage of quantum-enabled radar over classical radar (in terms of phase noise) in simulation. The most important and highly anticipated near-future goal would be the experimental realisation of the first quantum-enabled radar and tests that show very low phase noise levels in the range-Doppler plots compared to classical radars. A quantum-enabled radar, in reality, would be a great starting point to look at several applications, including detection of slow and weak targets in strong clutter [60], better classification of drones and birds based on micro-Doppler [160], and quantum-enabled networked radar [72].

6.3.5 Quantum-enabled network radar

Networked radars provide improved detection and tracking capability compared to monostatic radar systems [161]. Network radar consists of two or more radar systems working in harmony referenced by a common frequency and time reference, mostly global positional system disciplined oscillators (GPSDO) [162]. The performance of network radar primarily depends on the synchronisation linked to the frequency stability of the GPSDO. The quantum oscillators with ultra-high frequency stability, orders of magnitude higher than GPSDO [163, 164], make them the best candidate for networked radar systems.

6.3.6 DDS in radar systems

In any radar system, the frequency up-conversion is a crucial factor contributing to the phase noise. Radar systems with PLO consist of a reference oscillator followed by a PLL for frequency up-conversion. An alternative way is to directly synthesise the transmit frequency to bypass frequency up-conversion [165, 166]. The DDS can also generate signals with relatively low phase noise levels. The quantum oscillators with ultra-low phase noise levels can also act as stable frequency references for the DDS systems.

BIBLIOGRAPHY

[1] *Gamekeeper Aveillant 16 U*. Sept. 2020. URL: https://www.aveillant.com/products/gamekeeper/.

[2] James Clerk Maxwell. "VIII. A dynamical theory of the electromagnetic field". In: *Philosophical Transactions of the Royal Society of London* (), pp. 459–512.

[3] Heinrich Hertz. *Electric waves: being researches on the propagation of electric action with finite velocity through space*. Dover Publications, 1893.

[4] Sungook Hong. *Wireless: From Marconi's black-box to the audion*. MIT press, 2001.

[5] A. Marincic and D. Budimir. "Tesla's contribution to radiowave propagation". In: *5th International Conference on Telecommunications in Modern Satellite, Cable and Broadcasting Service. TELSIKS 2001. Proceedings of Papers (Cat. No.01EX517)*. Vol. 1. 2001, 327–331 vol.1. DOI: 10.1109/TELSKS.2001.954902.

[6] Hugh Griffiths, Peter Knott, and Wolfgang Koch. "Christian Hülsmeyer: Invention and demonstration of radar, 1904". In: *IEEE Aerospace and Electronic Systems Magazine* 34.9 (2019), pp. 56–60.

[7] Anil K Rajvanshi. "Nikola Tesla—The creator of the electric age". In: *Resonance* 12.3 (2007), pp. 4–12.

[8] Robert Watson-Watt. "Radar in war and in peace". In: *Nature* 156.3959 (1945), pp. 319–324.

[9] Rod Burman. "Summary of magnetron development". In: *2010 International Conference on the Origins and Evolution of the Cavity Magnetron*. IEEE. 2010, pp. 3–4.

[10] H. Ghadaki and R. Dizaji. "Target track classification for airport surveillance radar (ASR)". In: *2006 IEEE Conference on Radar*. 2006, 4 pp.-. DOI: 10.1109/RADAR.2006.1631787.

[11] Yong Yang et al. "Effects of K distributed sea clutter and multipath on radar detection of low altitude sea surface targets". In: *IET Radar, Sonar & Navigation* 8.7 (2014), pp. 757–766.

[12] Odile Adrian. "Future Surface Radar technology: From Air Defence to Air and Missile Defence". In: *2007 IEEE Radar Conference*. 2007, pp. 49–54. DOI: 10.1109/RADAR.2007.374189.

[13] Sandeep P. Sira et al. "Adaptive Waveform Design for Improved Detection of Low-RCS Targets in Heavy Sea Clutter". In: *IEEE Journal of Selected Topics in Signal Processing* 1.1 (2007), pp. 56–66. DOI: 10.1109/JSTSP.2007.897048.

[14] Shiyu Zhang et al. "Target Detection for Multistatic Radar in the Presence of Deception Jamming". In: *IEEE Sensors Journal* 21.6 (2021), pp. 8130–8141. DOI: 10.1109/JSEN.2021.3050008.

[15] Svante Björklund. "Target Detection and Classification of Small Drones by Boosting on Radar Micro-Doppler". In: *2018 15th European Radar Conference (EuRAD)*. 2018, pp. 182–185. DOI: 10.23919/EuRAD.2018.8546569.

[16] Mohammed Jahangir and Chris Baker. "Persistence surveillance of difficult to detect micro-drones with L-band 3-D holographic radar™". In: *2016 CIE International Conference on Radar (RADAR)*. 2016, pp. 1–5. DOI: 10.1109/RADAR.2016.8059282.

[17] R.J. Doviak, D.S. Zrnic, and D.S. Sirmans. "Doppler weather radar". In: *Proceedings of the IEEE* 67.11 (1979), pp. 1522–1553. DOI: 10.1109/PROC.1979.11511.

[18] Robert J Serafin and James W Wilson. "Operational weather radar in the United States: Progress and opportunity". In: *Bulletin of the American Meteorological Society* 81.3 (2000), pp. 501–518.

[19] Xinwei Chen et al. "Rain Detection From X-Band Marine Radar Images: A Support Vector Machine-Based Approach". In: *IEEE Transactions on Geoscience and Remote Sensing* 58.3 (2020), pp. 2115–2123. DOI: 10.1109/TGRS.2019.2953143.

[20] RE Rinehart and ET Garvey. "Three-dimensional storm motion detection by conventional weather radar". In: *Nature* 273.5660 (1978), pp. 287–289.

[21] Boming Liu et al. "Characteristics and performance of wind profiles as observed by the radar wind profiler network of China". In: *Atmospheric Measurement Techniques* 13.8 (2020), pp. 4589–4600.

[22] Muhammad Akram Adnan et al. "Vehicle speed measurement technique using various speed detection instrumentation". In: *2013 IEEE Business Engineering and Industrial Applications Colloquium (BEIAC)*. 2013, pp. 668–672. DOI: 10.1109/BEIAC.2013.6560214.

[23] Changzhi Li et al. "A Review on Recent Advances in Doppler Radar Sensors for Noncontact Healthcare Monitoring". In: *IEEE Transactions on Microwave Theory and Techniques* 61.5 (2013), pp. 2046–2060. DOI: 10.1109/TMTT.2013.2256924.

[24] Changzhan Gu and Changzhi Li. "From Tumor Targeting to Speech Monitoring: Accurate Respiratory Monitoring Using Medical Continuous-Wave Radar Sensors". In: *IEEE Microwave Magazine* 15.4 (2014), pp. 66–76. DOI: 10.1109/MMM.2014.2308763.

[25] Marco Mercuri et al. "Digital Linear Discrete FMCW Radar for Healthcare Applications". In: *2019 IEEE MTT-S International Microwave Symposium (IMS)*. 2019, pp. 144–147. DOI: 10.1109/MWSYM.2019.8701012.

[26] Lynn M. Carter, Donald B. Campbell, and Bruce A. Campbell. "Geologic Studies of Planetary Surfaces Using Radar Polarimetric Imaging". In: *Proceedings of the IEEE* 99.5 (2011), pp. 770–782. DOI: 10.1109/JPROC.2010.2099090.

[27] Alberto Moreira et al. "A tutorial on synthetic aperture radar". In: *IEEE Geoscience and Remote Sensing Magazine* 1.1 (2013), pp. 6–43. DOI: 10.1109/MGRS.2013.2248301.

[28] W.A. Al-Ashwal et al. "Measurements of bistatic radar sea clutter". In: *2011 IEEE RadarCon (RADAR)*. 2011, pp. 217–221. DOI: 10.1109/RADAR.2011.5960531.

[29] HD Griffiths et al. "Measurement and modelling of bistatic radar sea clutter". In: *IET radar, sonar & navigation* 4.2 (2010), pp. 280–292.

[30] Simon Watts. "Modeling and simulation of coherent sea clutter". In: *IEEE Transactions on Aerospace and Electronic Systems* 48.4 (2012), pp. 3303–3317.

[31] Luke Rosenberg, Simon Watts, and Maria Sabrina Greco. "Modeling the statistics of microwave radar sea clutter". In: *IEEE Aerospace and Electronic Systems Magazine* 34.10 (2019), pp. 44–75.

[32] Michael E O'Brien and Daniel G Fouche. "Simulation of 3D laser radar systems". In: *Lincoln Laboratory Journal* 15.1 (2005), pp. 37–60.

[33] Dominik Brunner et al. "Radar imaging simulation for urban structures". In: *IEEE Geoscience and Remote Sensing Letters* 8.1 (2010), pp. 68–72.

[34] Samuel Grosdidier, Alexandre Baussard, and Ali Khenchaf. "HFSW radar model: Simulation and measurement". In: *IEEE Transactions on Geoscience and Remote Sensing* 48.9 (2010), pp. 3539–3549.

[35] Dongran Yu et al. “An incoherent scatter radar simulation system based on MATLAB”. In: *IEEE Geoscience and Remote Sensing Letters* 17.9 (2019), pp. 1513–1517.

[36] Mahmod A Al-Zubaidy, Khalil H Sayidmarie, and Saad S Al-Shamaa. “Radar system simulator using PC and Matlab Simulink”. In: *2006 International Radar Symposium*. IEEE. 2006, pp. 1–4.

[37] Marc Brooker and Michael Inggs. “A signal level simulator for multistatic and netted radar systems”. In: *IEEE Transactions on Aerospace and Electronic Systems* 47.1 (2011), pp. 178–186.

[38] James Irving and Rosemary Knight. “Numerical modeling of ground-penetrating radar in 2-D using MATLAB”. In: *computers & Geosciences* 32.9 (2006), pp. 1247–1258.

[39] M Dudek et al. “The impact of phase noise parameters on target signal detection in FMCW-radar system simulations for automotive applications”. In: *Proceedings of 2011 IEEE CIE International Conference on Radar*. Vol. 1. IEEE. 2011, pp. 494–497.

[40] Walter Schottky. “Über spontane Stromschwankungen in verschiedenen Elektrizitätsleitern”. In: *Annalen der physik* 362.23 (1918), pp. 541–567.

[41] Walter Schottky. “Zur berechnung und beurteilung des schroteffektes”. In: *Annalen der Physik* 373.10 (1922), pp. 157–176.

[42] John B Johnson. “The Schottky effect in low frequency circuits”. In: *Physical review* 26.1 (1925), p. 71.

[43] Walter Schottky. “Small-shot effect and flicker effect”. In: *Physical Review* 28.1 (1926), p. 74.

[44] John B Johnson. “Thermal agitation of electricity in conductors”. In: *Nature* 119.2984 (1927), pp. 50–51.

[45] Harry Nyquist. "Thermal agitation of electric charge in conductors". In: *Physical review* 32.1 (1928), p. 110.

[46] John Bertrand Johnson. "Thermal agitation of electricity in conductors". In: *Physical review* 32.1 (1928), p. 97.

[47] Fred L Walls and Andrea DeMarchi. "RF spectrum of a signal after frequency multiplication; measurement and comparison with a simple calculation". In: *IEEE Transactions on Instrumentation and Measurement* 24.3 (1975), pp. 210–217.

[48] Augusto Aubry et al. "Radar Phase Noise Modeling and Effects-Part I : MTI Filters". In: *IEEE Transactions on Aerospace and Electronic Systems* 52.2 (2016), pp. 698–711. DOI: 10.1109/TAES.2015.140549.

[49] David B Leeson. "Oscillator phase noise: a 50-year review". In: *IEEE transactions on ultrasonics, ferroelectrics, and frequency control* 63.8 (2016), pp. 1208–1225.

[50] DB Lesson. "A simple model of feedback oscillator noise spectrum". In: *proc. IEEE* 54.2 (1966), pp. 329–330.

[51] RS Raven. "Requirements on master oscillators for coherent radar". In: *Proceedings of the IEEE* 54.2 (1966), pp. 237–243.

[52] Ali Hajimiri and Thomas H Lee. "A general theory of phase noise in electrical oscillators". In: *IEEE journal of solid-state circuits* 33.2 (1998), pp. 179–194.

[53] Alper Demir, Amit Mehrotra, and Jaijeet Roychowdhury. "Phase noise in oscillators: A unifying theory and numerical methods for characterisation". In: *Proceedings of the 35th annual Design Automation Conference*. 1998, pp. 26–31.

[54] Un-Ku Moon, Karti Mayaram, and John T Stonick. "Spectral analysis of time-domain phase jitter measurements". In: *IEEE Transactions on Circuits and Systems II: Analog and Digital Signal Processing* 49.5 (2002), pp. 321–327.

[55] Reza Navid, Thomas H Lee, and Robert W Dutton. "An analytical formulation of phase noise of signals with Gaussian-distributed jitter". In: *IEEE Transactions on Circuits and Systems II: Express Briefs* 52.3 (2005), pp. 149–153.

[56] Kashif Siddiq. "The impact of oscillator phase noise on the design of millimetre-wave continuous wave radar systems". PhD thesis. University of Bath, 2017.

[57] Stanley J Goldman. *Phase noise analysis in radar systems using personal computers*. Wiley-Interscience, 1989.

[58] Debashis Dhar et al. "Modeling and analysis of the effects of PLL phase noise on FMCW radar performance". In: *2017 IEEE International Symposium on Circuits and Systems (ISCAS)*. IEEE. 2017, pp. 1–4.

[59] Kashif Siddiq et al. "Phase noise in FMCW radar systems". In: *IEEE Transactions on Aerospace and Electronic Systems* 55.1 (2018), pp. 70–81.

[60] Mohammed Jahangir et al. "Development of Quantum Enabled Staring Radar with Low Phase Noise". In: *2021 18th European Radar Conference (EuRAD)*. 2022, pp. 225–228. DOI: 10.23919/EuRAD50154.2022.9784517.

[61] Tao Wu, Xiaohong Tang, and Fei Xiao. "Reserch on the coherent phase noise of millimeter-wave doppler radar". In: *Progress In Electromagnetics Research Letters* 5 (2008), pp. 23–34.

[62] Junhyeong Park et al. "Leakage Mitigation in Heterodyne FMCW Radar for Small Drone Detection With Stationary Point Concentration Technique". In: *IEEE Transactions on Microwave Theory and Techniques* 67.3 (2019), pp. 1221–1232. DOI: 10.1109/TMTT.2018.2889045.

[63] Svante Björklund. "Target detection and classification of small drones by boosting on radar micro-Doppler". In: *2018 15th European Radar Conference (EuRAD)*. IEEE. 2018, pp. 182–185.

[64] André Hanewinkel. "Architecture and operational results of feature based automatic radar target classification". In: *2019 20th International Radar Symposium (IRS)*. 2019, pp. 1–10. DOI: 10.23919/IRS.2019.8768189.

[65] BJ Bloom et al. "An optical lattice clock with accuracy and stability at the 10- 18 level". In: *Nature* 506.7486 (2014), pp. 71–75.

[66] Markus Gellesch et al. "Transportable optical atomic clocks for use in out-of-the-lab environments". In: *Advanced Optical Technologies* 9.5 (2020), pp. 313–325.

[67] Samuel M Brewer et al. "Al+ 27 quantum-logic clock with a systematic uncertainty below 10- 18". In: *Physical review letters* 123.3 (2019), p. 033201.

[68] Nathan Hinkley et al. "An atomic clock with 10–18 instability". In: *Science* 341.6151 (2013), pp. 1215–1218.

[69] Xiaopeng Xie et al. "Photonic microwave signals with zeptosecond-level absolute timing noise". In: *nature photonics* 11.1 (2017), pp. 44–47.

[70] Johannes Rimmelspacher et al. "Low Power Low Phase Noise 60 GHz Multichannel Transceiver in 28 nm CMOS for Radar Applications". In: *2020 IEEE Radio Frequency Integrated Circuits Symposium (RFIC)*. 2020, pp. 19–22. DOI: 10.1109/RFIC49505.2020.9218297.

[71] Stephan Kruse et al. "Phase Noise Investigation for a Radar System with Optical Clock Distribution". In: *2020 17th European Radar Conference (EuRAD)*. 2021, pp. 26–29. DOI: 10.1109/EuRAD48048.2021.00018.

[72] Jonathan M Jones et al. "Quantum Enabled Radar Sensing". In: *2022 IEEE International Topical Meeting on Microwave Photonics (MWP)*. IEEE. 2022, pp. 1–4.

[73] Merrill Ivan Skolnik. "Introduction to radar systems". In: *New York* (1980).

[74] David M Pozar. *Microwave engineering*. John wiley & sons, 2011.

[75] Takashi Fujii and Tetsuo Fukuchi. *Laser remote sensing*. CRC press, 2005.

[76] "IEEE Standard Letter Designations for Radar-Frequency Bands". In: *IEEE Std 521-1984* (1984), pp. 1–8. DOI: 10.1109/IEEESTD.1984.81588.

[77] Russell Rzemien. "Coherent radar: Guest editor's introduction". In: *John Hopkins APL Technical Digest* 18.3 (1997).

[78] William West. "Absorption of electromagnetic radiation". In: *AccessScience,© McGraw-Hill Companies* (2008).

[79] JF Scott. "Scattering of Electromagnetic Radiation". In: *McGraw-Hill Encyclopedia of Science and Technology,* 12 (1982), pp. 97–99.

[80] John Lekner. *Theory of reflection of electromagnetic and particle waves*. Vol. 3. Springer Science & Business Media, 1987.

[81] Michael Allaby. *A dictionary of geology and earth sciences*. Oxford University Press, 2013.

[82] Richard Rennie and Jonathan Law. *A dictionary of chemistry*. Oxford University Press, 2016.

[83] Isamu Matsunami, Ryohei Nakamura, and Akihiro Kajiwara. "RCS measurements for vehicles and pedestrian at 26 and 79GHz". In: *2012 6th International Conference on Signal Processing and Communication Systems*. 2012, pp. 1–4. DOI: 10.1109/ICSPCS.2012.6508004.

[84] Doren W Hess. "Introduction to RCS measurements". In: *2008 Loughborough Antennas and Propagation Conference*. IEEE. 2008, pp. 37–44.

[85] Merrill I Skolnik. *Radar handbook*. McGraw-Hill Education, 2008.

[86] Mark A Richards et al. *Principles of modern radar*. Vol. 1. Citeseer, 2010.

[87] Dario Camuffo. "Chapter 20 - Measuring Wind and Indoor Air Motions". In: *Microclimate for Cultural Heritage (Third Edition)*. Ed. by Dario Camuffo. Third Edition. Elsevier, 2019, pp. 483–511. ISBN: 978-0-444-64106-9. DOI: https://doi.org/10.1016/B978-0-444-64106-9.00020-1.

[88] Philippe Lacomme et al. *Air and spaceborne radar systems: An introduction*. Vol. 108. William Andrew, 2001.

[89] Vijay Garg. *Wireless communications & networking*. Elsevier, 2010.

[90] Walid A Zgallai. *Biomedical Signal Processing and Artificial Intelligence in Healthcare*. Academic Press, 2020.

[91] Enrico Rubiola. *Phase noise and frequency stability in oscillators*. Cambridge University Press, 2008.

[92] John R Vig et al. "IEEE standard definitions of physical quantities for fundamental frequency and time metrology-random instabilities". In: *IEEE Standard* 1139 (1999), p. 1999.

[93] Xiaolong Chen et al. "Measuring the power law phase noise of an rf oscillator with a novel indirect quantitative scheme". In: *Electronics* 8.7 (2019), p. 767.

[94] Floyd M Gardner. *Phaselock techniques*. John Wiley & Sons, 2005.

[95] WE Willshaw et al. "The high-power pulsed magnetron: development and design for radar applications". In: *Journal of the Institution of Electrical Engineers-Part IIIA: Radiolocation* 93.5 (1946), pp. 985–1005.

[96] Gorka Rubio-Cidre et al. "DDS-Based Signal-Generation Architecture Comparison for an Imaging Radar at 300 GHz". In: *IEEE Transactions on Instrumentation and Measurement* 64.11 (2015), pp. 3085–3098. DOI: 10.1109/TIM.2015.2440557.

[97] M Pieraccini et al. "High-speed CW step-frequency coherent radar for dynamic monitoring of civil engineering structures". In: *Electronics Letters* 40.14 (2004), p. 1.

[98] Herman Jalli Ng et al. "A DLL-Supported, Low Phase Noise Fractional-N PLL With a Wideband VCO and a Highly Linear Frequency Ramp Generator for FMCW Radars". In: *IEEE Transactions on Circuits and Systems I: Regular Papers* 60.12 (2013), pp. 3289–3302. DOI: 10.1109/TCSI.2013.2265966.

[99] M Gardner Floyd. "Charge-pump phase-lock loops". In: *IEEE Transaction on communications* 28.11 (1980).

[100] Dries Peumans, Adam Cooman, and Gerd Vandersteen. "Analysis of Phase-Locked Loops using the Best Linear Approximation". In: *2016 13th International Conference on Synthesis, Modeling, Analysis and Simulation Methods and Applications to Circuit Design (SMACD)*. IEEE. 2016, pp. 1–4.

[101] Bill Moran. "Mathematics of radar". In: *Twentieth Century Harmonic Analysis—A Celebration*. Springer, 2001, pp. 295–328.

[102] Jerry Eaves and Edward Reedy. *Principles of modern radar*. Springer Science & Business Media, 2012.

[103] Robert A Meyers et al. *Encyclopedia of physical science and technology*. Academic Press, 1987.

[104] Wolfgang Menzel and Arnold Moebius. "Antenna concepts for millimeter-wave automotive radar sensors". In: *Proceedings of the IEEE* 100.7 (2012), pp. 2372–2379.

[105] Alexander M Haimovich, Rick S Blum, and Leonard J Cimini. "MIMO radar with widely separated antennas". In: *IEEE signal processing magazine* 25.1 (2007), pp. 116–129.

[106] Jian Li and Petre Stoica. "MIMO radar with colocated antennas". In: *IEEE Signal Processing Magazine* 24.5 (2007), pp. 106–114.

[107] Jukka Ruoskanen, Pekka Eskelinen, and Heikki Heikkila. "Millimeter wave radar with clutter measurements". In: *IEEE aerospace and electronic systems magazine* 18.10 (2003), pp. 19–23.

[108] Norman W Guinard and John C Daley. "An experimental study of a sea clutter model". In: *Proceedings of the IEEE* 58.4 (1970), pp. 543–550.

[109] Alexander M. Haimovich, Rick S. Blum, and Leonard J. Cimini. "MIMO Radar with Widely Separated Antennas". In: *IEEE Signal Processing Magazine* 25.1 (2008), pp. 116–129. DOI: 10.1109/MSP.2008.4408448.

[110] Levent Sevgi. "Target reflectivity and RCS interactions in integrated maritime surveillance systems based on surface-wave high-frequency radars". In: *IEEE Antennas and Propagation Magazine* 43.1 (2001), pp. 36–51.

[111] G.W. Stimson et al. *Stimson's Introduction to Airborne Radar*. Radar, Sonar and Navigation. SciTech Publishing, 2014. ISBN: 9781613530221. URL: https://books.google.co.uk/books?id=BMpingEACAAJ.

[112] Robert J Mailloux. *Phased array antenna handbook*. Artech house, 2017.

[113] Volker Hessel, Holger Löwe, and Friedhelm Schönfeld. "Micromixers—a review on passive and active mixing principles". In: *Chemical engineering science* 60.8-9 (2005), pp. 2479–2501.

[114] Keng Leong Fong and Robert G Meyer. "Monolithic RF active mixer design". In: *IEEE Transactions on Circuits and Systems II: Analog and Digital Signal Processing* 46.3 (1999), pp. 231–239.

[115] Zhenzhou Tang and Shilong Pan. "Image-reject mixer with large suppression of mixing spurs based on a photonic microwave phase shifter". In: *Journal of Lightwave Technology* 34.20 (2016), pp. 4729–4735.

[116] Bert C Henderson and James A Cook. "Image-reject and single-sideband mixers". In: *WJ Tech. Note* 12.3 (1985).

[117] Hank Zumbahlen et al. *Linear circuit design handbook*. Newnes, 2011.

[118] Changzhi Li et al. *Principles and Applications of RF/microwave in Healthcare and Biosensing*. Academic Press, 2016.

[119] Wai Kai Chen. *The electrical engineering handbook*. Elsevier, 2004.

[120] Marcel JM Pelgrom and Marcel JM Pelgrom. *Analog-to-digital conversion*. Springer, 2013.

[121] Lizhe Tan and Jean Jiang. *Digital signal processing: fundamentals and applications*. Academic Press, 2018.

[122] Stefan Lindner et al. "ADC depending limitations for Six-Port based distance measurement systems". In: *2015 IEEE Topical Conference on Wireless Sensors and Sensor Networks (WiSNet)*. 2015, pp. 29–31. DOI: 10.1109/WISNET.2015.7127396.

[123] Boualem Boashash. *Time-frequency signal analysis and processing: a comprehensive reference*. Academic press, 2015.

[124] Yaguo Lei. *Intelligent fault diagnosis and remaining useful life prediction of rotating machinery*. Butterworth-Heinemann, 2016.

[125] Jonathan M Blackledge. *Digital signal processing: mathematical and computational methods, software development and applications*. Elsevier, 2006.

[126] Robert W Cayse. *Application of the Hilbert transform to Doppler radar signals from a hypervelocity gun*. Tech. rep. ARNOLD ENGINEERING DEVELOPMENT CENTER ARNOLD AFB TN, 1988.

[127] Douglas A Lyon. "The discrete fourier transform, part 4: spectral leakage". In: *Journal of object technology* 8.7 (2009).

[128] Fransiska DW Enggar et al. "Performance comparison of various windowing On FMCW radar signal processing". In: *2016 International Symposium on Electronics and Smart Devices (ISESD)*. 2016, pp. 326–330. DOI: 10.1109/ISESD.2016.7886743.

[129] KM Muraleedhara Prabhu. *Window functions and their applications in signal processing*. Taylor & Francis, 2014.

[130] Jarez S Patel, Francesco Fioranelli, and David Anderson. "Review of radar classification and RCS characterisation techniques for small UAVs or drones". In: *IET Radar, Sonar & Navigation* 12.9 (2018), pp. 911–919.

[131] Nima Mohajerin et al. "Feature extraction and radar track classification for detecting UAVs in civillian airspace". In: *2014 IEEE Radar Conference*. 2014, pp. 0674–0679. DOI: 10.1109/RADAR.2014.6875676.

[132] Rudolf F Graf. *Modern dictionary of electronics*. Elsevier, 1999.

[133] Ramon M Cerda. *Understanding quartz crystals and oscillators*. Artech House, 2014.

[134] D Chattopadhyay. *Electronics (fundamentals and applications)*. New Age International, 2006.

[135] Marvin Frerking. *Crystal oscillator design and temperature compensation*. Springer Science & Business Media, 2012.

[136] Colin Campbell. *Surface acoustic wave devices and their signal processing applications*. Elsevier, 2012.

[137] Liang Zhou et al. "Dielectric resonators with high Q-factor for tunable low phase noise oscillators". In: *IEEE Transactions on Components, Packaging and Manufacturing Technology* 3.6 (2013), pp. 1008–1015.

[138] Chien-Jung Li et al. "A rigorous analysis of a phase-locked oscillator under injection". In: *IEEE Transactions on Microwave Theory and Techniques* 58.5 (2010), pp. 1391–1400.

[139] Jouko Vankka, Jaakko Lindeberg, and Kari Halonen. "Direct digital synthesiser with tunable phase and amplitude error feedback structures". In: *IEE Proceedings-Circuits, Devices and Systems* 151.6 (2004), pp. 529–535.

[140] *ChronosTechnology*. Sept. 2020. URL: https://chronos.uk/.

[141] Harold Mark Goldenberg, Daniel Kleppner, and Norman Foster Ramsey. "Atomic hydrogen maser". In: *Physical Review Letters* 5.8 (1960), p. 361.

[142] Jonathan M. Jones et al. "Quantum Enabled Radar Sensing". In: *2022 IEEE International Topical Meeting on Microwave Photonics (MWP)*. 2022, pp. 1–4. DOI: 10.1109/MWP54208.2022.9997763.

[143] David Crecraft and Stephen Gergely. *Analog Electronics: circuits, systems and signal processing*. Elsevier, 2002.

[144] *Axtal OCXO*. Sept. 2020. URL: https://www.axtal.com/English/Products/CrystalOscillators/OvenControlledCrystalOscillatorsOCXO/.

[145] Xinyu Liu and Yu Sun. *Micro and Nano Systems for Biophysical Studies of Cells and Small Organisms*. Academic Press, 2021.

[146] Pierre Jarry and Jacques N Beneat. *Passive and Active RF-Microwave Circuits: Course and Exercises with Solutions*. Elsevier, 2015.

[147] Alan Bensky. *Short-range wireless communication*. Newnes, 2019.

[148] Robert A Meyers. *Encyclopedia of physical science and technology*. Academic, 2002.

[149] *Time and frequency from A to Z, Q to ra*. Sept. 2016. URL: https://www.nist.gov/pml/time-and-frequency-division/popular-links/time-frequency-z/time-and-frequency-z-q-ra.

[150] *T4Science*. Sept. 2020. URL: https://www.t4science.ch/products/imaser3000/.

[151] *Menlosystems*. Sept. 2020. URL: https://www.menlosystems.com/products/ultrastable-microwaves/pmwg-1500/.

[152] Jonathan Jones. "Quantum metrology with a single ytterbium ion optical clock". PhD thesis. University of Birmingham, 2018.

[153] *Vectron*. Sept. 2020. URL: https://www.vectron.com/index.htm.

[154] Peter P Bohn. *The relationship between phase stability and frequency stability and a method of converting between them*. Tech. rep. 1971.

[155] David W Allan. "Statistics of atomic frequency standards". In: *Proceedings of the IEEE* 54.2 (1966), pp. 221–230.

[156] David W Allan and James A Barnes. "A) IWlDIFIED" ALLAN VARIANCE" WITH INCREASED OSCILLATOR CHARACTERIZATION ABILITY". In: (1981).

[157] James Allen Barnes. *Tables of bias functions, B1 and B2, for variances based on finite samples of processes with power law spectral densities*. Vol. 375. US Department of Commerce, National Bureau of Standards, 1969.

[158] Lorenzo Galleani and Ilaria Sesia. "The corrected allan variance: stability analysis of frequency measurements with missing data". In: *IEEE Transactions on Ultrasonics, Ferroelectrics, and Frequency Control* 66.10 (2019), pp. 1667–1683.

[159] P Payandehnia et al. "Fully passive third-order noise shaping SAR ADC". In: *Electronics Letters* 53.8 (2017), pp. 528–530.

[160] Zihao Liu, Bo Peng, and Xiang Li. "Analysis of phase noise influence on micro-Doppler feature extraction of vibrating target". In: *The Journal of Engineering* 2019.20 (2019), pp. 6834–6839.

[161] Andrew L Hume and Christofer J Baker. "Netted radar sensing". In: *2001 CIE International Conference on Radar Proceedings (Cat No. 01TH8559)*. IEEE. 2001, pp. 110–114.

[162] Simon Lewis and Michael Inggs. "Synchronization of Coherent Netted Radar Using White Rabbit Compared With One-Way Multichannel GPSDOs". In: *IEEE Transactions on Aerospace and Electronic Systems* 57.3 (2021), pp. 1413–1422. DOI: 10.1109/TAES.2020.3043530.

[163] JS Sandenbergh and MR Inggs. "Synchronizing network radar using all-in-view GPS-disciplined oscillators". In: *2017 IEEE Radar Conference (RadarConf)*. 2017, pp. 1640–1645. DOI: 10.1109/RADAR.2017.7944470.

[164] Matthew A Norcia et al. "Frequency measurements of superradiance from the strontium clock transition". In: *Physical Review X* 8.2 (2018), p. 021036.

[165] Björn Möhring et al. "Broadband, Fast, and Linear Chirp Generation Based on DDS for FMCW Radar Applications". In: *2019 IEEE Radar Conference (RadarConf)*. 2019, pp. 1–4. DOI: 10.1109/RADAR.2019.8835542.

[166] Serdal Ayhan et al. "Impact of Frequency Ramp Nonlinearity, Phase Noise, and SNR on FMCW Radar Accuracy". In: *IEEE Transactions on Microwave Theory and Techniques* 64.10 (2016), pp. 3290–3301. DOI: 10.1109/TMTT.2016.2599165.

[167] S. Watts and L. Rosenberg. "A comparison of coherent and non-coherent radar detection performance in radar sea clutter". In: *International Conference on Radar Systems (Radar 2017)*. 2017, pp. 1–6. DOI: 10.1049/cp.2017.0497.

[168] Terry N Guo. "Unique measurement and modeling of total phase noise in RF receiver". In: *IEEE Transactions on Circuits and Systems II: Express Briefs* 60.5 (2013), pp. 262–266.